Atomic Energy Control Board
P.O. Box 1046
Ottawa, Canada
K1P 5S9

Commission de contrôle de l'énergie atomique
C.P. 1046
Ottawa, Canada
K1P 5S9

INFO-0110

ULTRASONIC SIZING OF FATIGUE CRACKS

by

D.J. Burns

A research report prepared for the
Atomic Energy Control Board
Ottawa, Canada

RESEARCH REPORT

December 19, 1983

ULTRASONIC SIZING OF FATIGUE CRACKS

A research report prepared by D.J. Burns, Department of Mechanical Engineering, University of Waterloo, under contract to the Atomic Energy Control Board.

ABSTRACT

Surface and buried fatigue cracks in steel plates have been sized using immersion probes as transmitters-receivers, angled to produce shear waves in the steel. Sizes have been estimated by identifying the ultrasonic waves diffracted from the crack tip and by measuring the time taken for a signal to travel to and from the crack tip. The effects of compression normal to a fatigue crack and of crack front curvature are discussed. Another diffraction technique, developed by UKAEA, Harwell, is reviewed.

RÉSUMÉ

Les fissures dues à la fatigue sur la surface et à l'intérieur des plaques d'acier ont été mesurées en utilisant des sondes d'immersion comme émetteurs-recepteurs et en les inclinant pour produire des ondes de cisaillement dans le métal. Les dimensions ont été estimées en déterminant la nature des ondes ultrasoniques diffractées au bout de la fissure et en mesurant le temps qu'un signal prend pour parcourir l'étendue de la fissure aller-retour. Le rapport traite également de la compression normale sur une fissure due à la fatigue et de la courbure du front de la fissure, ainsi que d'une autre technique de diffraction, développée par UKAEA, Harwell.

DISCLAIMER

The Atomic Energy Control Board is not responsible for the accuracy of the statements made or opinions expressed in this publication and neither the Board nor the author assumes liability with respect to any damage or loss incurred as a result of the use made of the information contained in this publication.

TABLE OF CONTENTS

		Page
1.	Introduction	1
2.	Ultrasonic Equipment	6
	2.1 Pulse Echo Instrument and Time Delay Unit	6
	2.2 Ultrasonic Probes	7
	2.2.1 Immersion Probes	7
	2.2.2 Contact Probes	8
3.	Mechanical Scanning Systems	9
	3.1 Modification of Existing Immersion Rig	9
	3.2 Immersion Rig For Use With Twin Probe Technique	10
4.	Theory and Technique	11
	4.1 Single Probe Inclined at θ x z = 0	11
	4.2 Twin Probes	12
	4.2.1 Calculations of Time of Flight	13
	4.2.2 Estimation of V_0 and (C/V_0)	16
	4.2.3 YZ Locations of Points G on the Defect Front	16
5.	Specimen Preparation	18
6.	Experimental Results and Discussion	20
	6.1 Sizing Fatigue Cracks in Plate 11 and 12 with θ x Z = 0	20
	6.1.1 Plate 11 Without Compressive Load Applied	21
	6.1.2 Plate 11 With Compressive Load Appied	22
	6.1.3 Plate 12 With and Without Compressive Load Applied	23
	6.2 Sizing a 'regular' EDM Defect with Twin-probe Technique	24
	6.3 Plate 21 With and Without Compressive Applied to the Fatigue Crack	25
	6.4 Plate 22 and 23 With Burred Fatigue Cracks	27
	6.4.1 Sizing of Defect in Plate 22	28
	6.4.2 Sizing of Defect in Plate 23	29
	6.5 Sizing of Irregular Defects	30
	6.5.1 Sizing of Defect EDM 1	30
	6.5.2 Sizing of EDM 2	31
	6.5.3 Sizing of EDM 3	32
	6.6 Measurement of Surface Length of Fatigue Cracks	33
7.	Discussion	35
	7.1 Effects of Compression or Ultrasonic Response	35
	7.2 Diffraction Sizing Technqiue Using Probe as a Transmitter-Receiver	38
	7.3 Harwell 'Separable Probe' Diffraction Technique	39

	Page
Conclusions	43
Acknowledgements	44
References	45
Appendix	48
Tables	50
Figures	65

LIST OF FIGURES

Fig. No.	
1	Separable Probe Technique
2	Basic Immersion Probe Layout
3	Crack Photos; Plate 2, 3, 4, 5, 6, 7, 8, 11 and 12
4	Beam Path Through Steel Plate
5	Functional Diagram of Time Delay Unit
6	Internal Mechanism Existing Immersion Rig
7	Complete Frame Existing Immersion Rig (Photo)
8	Twin Probe Immersion Rig (Photo)
9	Side View Twin Probe Immersion Rig
10	Front View Twin Probe Immersion Rig
11	Horizontal Calibration Hole
12	Vertical Calibration Hole
13	Calibration Plate for Twin Probe Rig
14	Beam Path Through Oil
15	Complete Beam Path
16	Angle Probe Mechanism for Twin Probes
17	Beam Path to Corner and Tip of Calibration Hole
18	Detailed View of Calibration Hole
19	Edm Cracks 1, 2, and 3 (Photo)
20	Weld Preparation and Weld
21	Final Weld Cap
22	Time of Flight versus Lateral Position
23	Relative Amplitude versus Compression
24	Time of Flight versus Repeated Compression
25	Relative Amplitude versus Lateral Position
26	Time of Flight versus Lateral Position/Compression
27	Graph of EDM Crack Results - First Test
28	Graph of EDM Crack Results - Second Test
29	Fatigue Crack Shape Uldat 1
30	Fatigue Crack Shape Uldat 2
31	Fatigue Crack Shape Uldat 3
32	Fatigue Crack Shape Uldat 4
33	Fatigue Crack Shape Uldat 5
34	Photos Plate 22 Section 1-10
35	Photos Plate 23 Section 4-8 and Typical Weld Section
36	Plate 22 Crack Dimensions
37	Plate 23 Crack Dimensions
38	Fatigue Crack Shape Uldat 7A
39	Fatigue Crack Shape Uldat 8
40	Fatigue Crack Shape Uldat 9
41	Fatigue Crack Shape Uldat 12
42	Fatigue Crack Shape Uldat 13
43	EDM 1 Results
44	EDM 2 Results
45	EDM 3 Small Wedge Results 3 mm Steps
46	EDM 3 Large Wedge Results 3 mm Steps
47	EDM 3 Small Wedge Results 1 mm Steps
48	EDM 3 Large Wedge Results 1 mm Steps
49	Echo Amplitude Method Without Compression
50	Echo Amplitude Method with Compression
51	Error in Depth for Near Surface Cracks
52	Weld Defects

1. Introduction

An important input to the fracture mechanics analysis of a component is the nature, orientation and size of inherent defects or defects produced by service loading. Although ultrasonic inspection has been used in some industries for many years, there is still considerable debate as to the reliability and accuracy of various ultrasonic techniques for detecting and sizing planar defects such as fatigue cracks.

The ultrasonic parameter most often used for detection and sizing is the pulse echo amplitude. It is assumed that the amplitude of the ultrasonic beams, reflected specularly from the main face of the defect, can be correlated with defect size. Often the error band associated with such 'echo amplitude' sizing techniques is very wide [1] and it may not be valid in some cases to assume a correlation between echo amplitude and defect size [2].

Another factor to be considered is that a fatigue crack, or like defect, in a residual compressive stress field may show considerable ultrasonic transmission and a reduction in reflectivity. For example M. Mahmoud [3] grew surface fatigue cracks in A1030 steel plates and found, in immersion tests with shear waves, that the echo amplitude from these cracks dropped as much as 5 dB when the cracked surface was subjected to compressive bending stresses of 24.5 MNm^{-2}. Also Wooldridge [4] of the C.E.G.B. Non Destructive Testing Applications Centre, Manchester has reported reductions in reflectivity of up to 12 dB for

normal incidence compression waves and up to 25 dB for angled shear waves. In his tests, mild steel specimens containing fatigue cracks, 5, 10 or 15 mm deep, were subjected to compression stresses up to 150 MNm^{-2}.

This and other limitations of echo amplitude techniques led M. Mahmoud and the author to look for alternative sizing techniques. A technique that seemed to have promise was to locate the defect tip(s) by identifying the ultrasonic waves diffracted from the defect tip. By measuring the time taken for waves to travel to and from the defect tip one can obtain estimates of defect depth that are independent of echo amplitude. However the amplitude of the defect tip signal is smaller than that reflected from the main face of the defect so identification of the tip signal is more difficult and one questions whether tip signals can still be identified if one is looking for fatigue cracks in a residual compressive stress field.

A diffraction technique developed at the NDT Centre at Harwell will be discussed in some detail later so only a brief description will be given here. As shown in Figure 1, angled longitudinal wave probes are placed each side of the crack with one probe transmitting and the other receiving. The time delay in receiving the crack tip echo t_D, can be used to calculate d, the position of the crack tip below the surface, if the separation 2S, of the probes is known. If the crack tip lies midway between the beam entry and exit points on the plate, the geometry

gives:

$$t_D = \frac{2}{C_L} (^2 + d^2)1/2$$

where C_L is the velocity of longitudinal waves in the plate [5].

A basic limitation of this 'separable' probe technique is that the two probes must be linked so that their separation remains essentially constant. Also for some complex geometries it may not be physically possible to use two probes. In such cases it may be possible to use a single probe acting as a transmitter-receiver. Evaluation of a single probe diffraction technique has been the main thrust of recent work at Waterloo [3,6] and the basis for the research reported herein.

This 'single' probe, technique was used by Mahmoud [3] to size surface fatigue cracks in steel plates. Scans were made from the uncracked side of the plate, Fig. 2(a), using immersion probes in water to generate oblique shear waves in the plate. As mentioned previously Mahmoud observed that the echo from the main face of the crack dropped in amplitude as much as 5 dB when the cracked surface was subjected to compressive bending stress. However these preliminary experiments showed that the smaller crack tip echo could usually still be identified. Also measurements of the time delay in receiving this crack tip echo gave good estimates of crack depth, with or without compression on the cracks.

Although Mahmoud's observations were encouraging there was concern that crack closure effects would have been more significant if the cracks had been subjected to pure compression rather than compression

induced by plate bending. Also all of the surface fatigue cracks in Mahmoud's plates, photographs 2-8 on Figure 3, had a smooth front and were almost uniform in depth over most of their length. It was argued that there might have been significant loss of crack tip signal at some points along the crack fronts if

(1) the curvature of these so-called regular cracks had been more pronounced, see schematic Fig. 2(b), or

(2) there had been significant changes in curvature along the crack front. Fig. 2(c) shows a so-called irregular crack with changes from convex to concave curvature along its front.

This anticipated loss of crack tip signal can be explained using the schematic shown in Figure 4. In Mahmoud's experiments the beam entered the plate at Q and met the crack tip at some point G. When the angle β in the xz plane, of the tangent to the crack front at G exceeds some critical value, β^*, it is likely that the crack tip signal returned to the probe will be too weak to be identified.

In Mahmoud's experiments this signal loss was not a problem because the angle β was very small over most of the crack front, see Fig. 3, plates 2-8. However this might not be the case for many 'regular' cracks and is often not the case for 'irregular' cracks. In theory it should be possible to reduce this problem by using twin-probes, each acting as a transmitter-receiver. As in Mahmoud's experiments one of these probes should be oriented so that its path in the steel plate is the line QG on Fig. 4. (i.e. $\theta_{xz} = 0$). The other probe should be

oriented at some angle θ_{xz} so that its path in the steel plate is the line CG on Fig. 4. This probe should receive crack tip echoes from steeper (large β) parts of the crack front that are not "seen" by the probe with the standard orientation, $\theta xz = 0$.

In view of the known limitations of echo amplitude techniques and the limited information published on time domain (diffraction) techniques, a research proposal was submitted to AECB on February 6th, 1981. The proposal recommended an extension of the experimental program started by Mahmoud and a review of sizing techniques being explored by others. The objectives of the experimental program described herein have been to:

1) further explore the ability of the single-probe diffraction technique to size fatigue cracks
2) whenever possible record pulse echo amplitudes as well as time domain data so as to add to our understanding of the limitations of sizing methods based on echo amplitudes.
3) further explore the effect of compression on the crack, when sizing fatigue cracks. In particular to use pure compression rather than bending to induce crack closure
4) ascertain the effects of an irregular crack front. In particular to see if loss of crack tip signal is a major problem when using the single probe diffraction technique. Also to see if the twin-probe diffraction technique mentioned earlier is useful for looking at steep parts of a crack front.

5) ascertain the effects of transducer frequency, diameter, incident angle and standoff distance

6) conduct experiments to extend the basis of the above comparison to cracks in plate welds. Since weld cracks may be buried an attempt has been made to simulate a buried crack.

2. Ultrasonic Equipment

2.1 Pulse-echo instrument and time delay unit

The pulse-echo instrument used is a Sperry UM 771 Reflectoscope with a type D timer and a type ION dB pulse-receiver. Although this unit has a built-in sweep delay circuit for measuring signal-delay time, its accuracy is unsuitable for the time-domain technique used in this study. Therefore the Reflectoscope is used with an external time delay unit that is much more accurate and stable. The delay unit designed for this purpose is shown schematically in Fig. 5. The unit receives the main pulse synchronisation signal through a rear connector on the Reflectoscope. This sets a reset/set flip-flop, which sets a counter. The counter starts to count the pulses coming from a crystal oscillator. The counter outputs are connected to thumb wheel selector switches. When the number of pulses received by the counter is equal to the number selected on the thumb wheel selectors, the flip-flop and counter reset, and the trigger for the start of the sweep in the Reflectoscope is generated. This means that the display on the Reflectoscope screen starts after the preselected delay and that by switching the thumb wheel selectors it is possible to display different regions of the ultrasonic path.

To measure the transit time for crack tip signals, the thumb wheel switches are used to select a value that leads to a delayed sweep equivalent to the transit time, i.e. the start of display on the screen coincides with the signal of interest. The transit time is then equal to the product of the number preselected with the thumb wheel switches (which equals the number of pulses counted by the counter), and the time period of the oscillator. The oscillator used in the present unit is a crystal-controlled generator, with a frequency of 5 MHz ∓ .05%. Its stability is approximately 10 parts per million per °C. The selector switches used with the above unit allow time delay measurements in the range 0.2 to 199.8 μ sec. The time resolution of the unit is 0.2 μ sec.

2.2 Ultrasonic Probes

2.2.1. Immersion Probes

The experiments by Mahmoud [3] that led to the present research program were made in water with a Krautkramer MB-4T immersion probe which had a 12.7 mm, 4MHz crystal. Although this was a good couplant-probe combination, it was decided to try a mineral oil as couplant to avoid rusting of the fatigue cracks; some of the test plates were needed for a variety of experiments and were not broken open for several months.

The MB-4T probe worked well in the mineral oil and was used for some of the experiments discussed herein. Unfortunately this probe was damaged during the commissioning of the angle probe rig (section 3.2) so a 5MHz probe in our laboratory stock was tried. This 1/4 inch diameter KB-Aerotech probe did not give good tip signals in the mineral oil so a silicone oil, Dowtherm A was tried. This had proved to be a

useful couplant in earlier work [3] and, fortunately, gave good signals with the 5MHz probe. This combination was only used on a temporary basis because Dowtherm A is an unpleasant liquid to handle!

When new probes were ordered it was found that 4MHz probes were no longer a catalogue item but that 3.5 MHz, 1/2 mm probes were and likely to be available in 2-3 months. Therefore two 3.5MHz, 1/2 inch KB-Aerotech probes have been used for most of the 'twin probe' experiments discussed herein. These work well with the mineral oil couplant. It was found that probes with a lower frequency, 2.25 MHz gave a poor response.

To summarize it was found that probes of 3.5 to 4 MHz worked well with the mineral oil couplant. Probes of 2.25 or 5 MHz did not give good tip signals. It was not possible, due to time and cost limitations, to adequately explore the effect of probe diameter; one can only say that 1/4 and 1/2 immersion probes gave acceptable signal response.

2.2.2. Contact probes

During the discussions of the research proposal for this project it was agreed that some experiments would be made with contact probes. It was decided to use contact probes for the first experiments on defects with irregular fronts since the calibration experiments on the new immersion rig (section 3.2) indicated that some design modifications were required.

5 and 2.25 MHz probes were purchased from KB-Aerotech. Preliminary experiments on a defect with a regular front indicated that the 5 MHz probe had a greater resolution but it was much easier to separate the tip signal when using the 2.25 MHz probe. Therefore all of the contact data presented herein was obtained using this 2.25 MHz 1/2 inch probe with 45° wedges.

Two wedges were purchased from Aerotech. One of these was custom built (so-called large wedge PN2102191) to give a greater standoff. The extra thickness of wedge material reduces the number of reflections picked up from the wedge/metal interface and gives a better separation between 'nuisance' signals and those received from the defect. On the other hand the standard wedge purchased (so-called small wedge ST45) gives a stronger tip signal so both wedges were used.

3. Mechanical Scanning Systems

3.1 Modification of existing immersion rig

This rig, Fig. 6, was developed previously for immersion testing at temperatures up to 290°C [7]. The probe sleeve locates the probe at $\theta_{xz} = 0$ and at a known distance (x axis) above the test plate. The carriage mechanism allows one to change the angle of incidence θ_{xy} and lateral position (y axis) of the probe.

It was decided to modify this rig so that it could be clamped to cracked plates, while they were subjected to pure compression in a standard testing machine. Also, since the fatigue cracks lie in the zx plane, Fig. 4, provision had to be made for moving the probe in the z direction to permit measurements at various positions along the crack front. This was achieved by mounting the rig (Fig. 6), in the frame shown in Fig. 7. The springs, on this frame, clamp the rig against the test plate. This prevents couplant leakage but still allows one to slide the rig across the plate in the z direction. Dial gauges are mounted on the frame to measure the 'z' position of the probe.

3.2 Immersion rig for use with twin probe technique

Figures 8-10 show the new probe rig built for this research program. The carriage can accommodate three probes although only two were normally used. All of the probes can be rotated in the xy and zx planes; in the other rig (section 3.1) the probe could only be rotated in the xy plane. The probes can be moved separately or together across the crack front, ie. along the z axis. They can also be moved in the y direction using the micrometers shown.

Although this rig was checked very carefully by our machine shop using various metrology techniques, it was deemed wise to first check out the system and method of analysis (section 4.2) by using the rig to measure the depth of holes drilled in steel plates. Side-drilled holes could only be sized when θxz was set at zero, Fig. 11a, since the signal disappeared when θxz was not zero, Fig. 11b.

Two types of bottom-drilled hole, Figs. 12a and 12b, were scanned with probes set at non-zero values of θxz. The first set of holes, Fig. 12a, had bottoms which were almost flat and it was not possible to identify a 'tip' signal. The second set of holes had bottoms which were hemispherical, Fig. 12b. Since a small part of this hemispherical end was always perpendicular to the beam path, it was always possible to find a 'tip' signal at the θxz angles of interest, see Table 1.

The dimensions (mm) of the holes used are shown in Fig. 13. The times of flight from the face of the probe crystal to the hole 'tip' and back were measured and calculated for various probe positions. Since there was good agreement between measured and calculated times of

flight, Table 1, the same method was used to calculate times of flight for crack tip signals received by an angle probe. This method is explained in section 4.2.

4. Theory and Techniques

4.1. Single Probe inclined at $\theta xz = 0$

The basic testing geometry is shown in Figure 2. The immersion probe is positioned so that $\theta xz = 0$, therefore the angle of incidence is the angle θ on Fig. 2.

An estimate of defect depth, a, at any location, z, along the crack front (see Fig. 2a and b) was obtained by moving the transducer in the y direction until the echo from the crack tip reached a maximum. Assume that Fig. 2a illustrates the probe position which gives the largest echo from the defect. If θ and h are fixed and the tip signal is always maximum when the same ray impinges on the defect tip regardless of depth, a, then one can obtain estimates of defect depth by solving the simultaneous equations:

$$\phi = \mathrm{Sin}^{-1}\,(C_s \mathrm{Sin}\theta / C_D)$$

$$y = h\,\tan\theta + d\,\tan\phi$$

$$T = 2(h/C_D\,\mathrm{Cos}\theta + d/C_s\,\mathrm{Cos}\phi)$$

$$a = D - d$$

where C_s is the shear wave velocity in the steel; C_D is the sound velocity in the couplant; T is the time of the two-way path between the crystal face and defect tip.

These equations indicate that the time T should decrease linearly as the defect depth, a, increases. This was confirmed by stationing the probe at various positions, z, along a calibration plate containing a milled saw slot tapering in the z direction. The data obtained in such calibration experiments [6] can be used to convert time measurements taken on fatigue cracks into estimates of defect depth.

4.2 Twin Probes

The theory outlined above can be used to interpret time data obtained from the probe inclined at $\theta xz = 0$. However its twin has a double inclination, θxz and $\theta x'y$, as shown in Fig. 14a. The ultrasonic beam DC travels through a layer of couplant, thickness AC, and enters the steel plate lying in the yz plane. Since the beam enters the plate at point C the angle of incidence is defined as the angle between the beam DC and the line, AC, which is perpendicular to the front face of the plate.

This angle

$$\theta_{xyz} = \text{Cos}^{-1}\left(\frac{AC}{DC}\right)$$

can be related to the set (measured) transducer angles ($\theta_{x'y}$ and θ_{xz}) by the following equations

$$AC = BC \text{ Cos } \theta_{xz} \qquad (1)$$

$$DC = \frac{BC}{\text{Cos } \theta_{x'y}} \qquad (2)$$

i.e., $$\theta_{xyz} = \text{Cos}^{-1} (\text{Cos } \theta_{xz} \text{Cos } \theta_{x'y}) \qquad (3)$$

The angle of the beam in the steel plate (ϕ_{xyz} on Fig. 14b) is

obtained from the refraction equation

$$\frac{\text{Sin } \phi_{xyz}}{\text{Sin } \theta_{xyz}} = \frac{\text{ultrasonic velocity in steel } (V_{ss})}{\text{ultrasonic velocity in couplant } (V_o)} \qquad (4)$$

In the present study the beam travelled as a compression wave in the oil couplant and as a shear wave in the steel plate. The velocity of the compression wave in the oil was measured (see next section) and the shear velocity in steel was calculated using data published by Krautkramer. Combining equations (3) and (4) then gives

$$\phi_{xyz} = \text{Sin}^{-1}\left[\frac{V_{ss}}{V_o} \text{Sin } \left[\text{Cos}^{-1}(\text{Cos } \theta_{x'y} \text{Cos } \theta_{xz})\right]\right] \qquad (5)$$

Figure 15 shows the beam travelling in the couplant oil, entering the steel plate at point C and interacting with the hole 'tip', slot tip or crack tip at point G. The beam is travelling in a plane which contains the surfaces ADC and EGC, i.e. the angles $\widehat{BDA}$ and $\widehat{FCE}$ are the same and denoted by α.

4.2.1 Calculation of Times of Flight

To calculate the times of flight one must relate the beam path length, DCG, to the probe angles $\theta_{x'y}$ and θ_{xz} and other geometric measurements. Fig. 16 shows how the transducer was positioned with respect to the steel plate. The face of the transducer was set at distance K from the plate, using a calibration block, with $\theta_{x'y}$ and θ_{xz} set at zero. This distance K and measurements of the separation (Rxy) of the z pivot and the probe face, and of the separation (R) of the z and y pivots can be used with experimental settings of $\theta_{x'y}$ and θ_{xz} to calculate the beam path length.

First consider the calculation of the beam path length from the transducer face to the point C when it enters the steel. This path length, Dm on Figs. 17a and 17b, can be obtained from the equation

$$\frac{R + R_{xy} + K}{R_h + R_{xy} + D_m} = \text{Cos } \theta_{xyz} \qquad (6)$$

where $R_h = \frac{R}{\text{Cos } \theta_{x'y}}$ as shown on Fig. 16 (7)

Combining these equations gives

$$D_m = \frac{(R + R_{xy} + K)}{\text{Cos } \theta_{xyz}} - \frac{R}{\text{Cos } \theta_{x'y}} - R_{xy} \qquad (8)$$

and combining equations (8) and (3) gives

$$D_m = \frac{R + R_{xy} + K}{\text{Cos } \theta_{xy} \text{ Cos } \theta_{x'y}} - \frac{R}{\text{Cos } \theta_{x'y}} - R_{xy} \qquad (9)$$

To calculate the time of flight for a corner signal one must calculate Dm and the length D_c shown on Fig. 17a. For a steel plate of thickness t_s

$$D_c = \frac{t_s}{\text{Cos } \phi_{xyz}} \qquad (10)$$

where ϕ_{xyz} is defined by equation (4).

To calculate the time of flight for a 'tip' signal reflected from the bottom of one of the calibration holes one must calculate D_m and the length D_t shown on Fig. 17b. Since the bottoms of these holes were machined to have a hemispherical surface of 3 mm radius, see Fig. 18 , the path length D_t is related to the plate thickness t_s and hole depth, d, by the following equations

$$D_T = \frac{H_d}{\text{Cos } \phi_{xyz}} \qquad (11)$$

where

$$H_d = t_s - (N + M)$$

$$= t_s - (N + d - 0.003)$$

$$H_d = t_s - \frac{0.003}{\text{Cos } \phi_{xyz}} - d + 0.003 \qquad (12)$$

For an EDM slot or fatigue crack, equation (11) can be used directly to calculate the depth of the defect tip below the plate surface. Equations (9) - (12) can be used with measured times of flight, from the crystal face to the defect tip and back, to size the defect. If the defect depth is known, as was the case for the calibration holes, the equations can be used to calculate times of flight for comparison with measured values, Table 1.1 - 1.8.

For example consider the time of flight for the 'tip' of the bottom drilled hole, Fig. 17b. The immersion probes used in these experiments have a protective plastic coating in front of the crystal. If this coating has a thickness, c, the time of flight to and from the defect tip,

$$T_D = \frac{2c}{V_c} + \frac{2D_m}{V_o} + \frac{2D_T}{V_{ss}} \qquad (13)$$

where V_c is the ultrasonic velocity in the plastic coating, V_o is the velocity of compression waves in the oil and V_{ss} is the velocity of shear waves in the steel.

Equations (9), (11) and (12) define D_M and D_T so T_D can be calculated if one has values for c, V_c, V_o and V_{ss}. If, as in the present case, c is indeterminate one must find values for (c/V_c), V_o and V_{ss}. As mentioned previously V_{ss} was obtained from data published by Krautkramer although it could have been obtained by experiment. The next section describes the experiment used to calculate (c/V_c) and V_0.

4.2.2 Estimation of V_o and (c/V_c)

If $\theta_{x'y}$ and θ_{xz} are set at zero and the probe is directed at a plate without defects, one obtains a series of reflections from the front and back surfaces of the plate. For an oil path length K_1 the first signal received from the front surface of the plate will have a time

$$T_{B1} = \frac{2c}{V_c} + \frac{2K_1}{V_o} \tag{14}$$

For an oil path length K_2 the corresponding time will be

$$T_{B2} = \frac{2c}{V_c} + \frac{2K_2}{V_o} \tag{15}$$

Therefore the acoustic velocity in oil can be calculated from

$$T_{B2} - T_{B1} = \frac{2}{V_o} (K_2 - K_1) \tag{16}$$

This value of V_o can then be substituted back into equation (14) or (15) to obtain (c/V_c). These values of V_o and (c/V_c) can also be checked by looking at the first back surface signal and at subsequent reflections from front and back surfaces. Such studies gave an average value of 1470 m/sec for V_o in mineral oil and an average value of 0.6 microseconds for (c/V_c). The timing system described earlier counts in units of 0.2 microseconds so ignoring the factor c/V_c in the present studies would have led to an underestimation of hole or crack depth of the order of 1 mm. In fact this mistake was made initially.

4.2.3. YZ Locations of Point G on the Defect Front

Equation (11) and the known standoff K of the transducer determine the X location of the point G. Equations must also be developed for the Y and

Z locations. If point D on Fig. 15 is now assumed to be any convenient reference point on the transducer, then the problem is to find the distances (Z' + Z'') and (Y' + Y'').

For convenience the Y' distance is measured from the Z pivot on the probe holder (Fig. 16). In other words the length of AC is $R_{xy}+K$ and the length of BC is

$$BC = \frac{R_{xy} + K}{\text{Cos } \theta_{xz}} \tag{17}$$

and

$$DB = BC \tan \theta_{x'y} \tag{18}$$

i.e.

$$Y' = DB = \frac{(R_{xy}+ K)}{\text{Cos } \theta_{xy}} \tan \theta_{x'y} \tag{19}$$

For convenience the Z' distance is measured from the Y pivot on the transducer holder (Fig. 16). In this case the length of AC is $R+R_{xy}+K$ and $Z' = BA = AC \tan \theta_{xz}$.

i.e. $$Z' = (R + R_{xy} + K) \tan \theta_{xz} \tag{20}$$

To define Y'' and Z'', line CE and angle α on Fig. 15 must be found. Since CG is D_T, which has already been defined, see equation (11), then $CE = CG \text{ Sin } \phi_{xyz} = D_T \text{ Sin } \phi_{xyz}$. (21)

As mentioned previously the spaces CGE and DAC are in the same plane. Therefore the angle

$$\alpha = \tan^{-1} \frac{BA}{DB} \tag{22}$$

where $BA = BC \text{ Sin } \theta_{xy}$

and $DB = BC \text{ Tan } \theta_{x'y}$ (23)

Substituting equations (23) into (22) gives

$$\alpha = \tan^{-1}\left[\frac{\text{Sin } \theta_{xz}}{\text{Tan } \theta_{x'y}}\right] \tag{24}$$

and

$$Y'' = CE \text{ Cos } \alpha = D_T \text{ Sin } \phi_{xyz} \text{ Cos } \left[\tan^{-1} \left[\frac{\text{Sin } \theta_{xy}}{\text{Tan } \theta_{x'y}}\right]\right] \tag{25}$$

and

$$Z'' = CE \text{ Sin } \alpha = D_T \text{ Sin } \phi_{xyz} \text{ Sin } \left[\text{Tan}^{-1}\left[\frac{\text{Sin } \theta_{xy}}{\text{Tan } \theta_{x'y}}\right]\right] \tag{26}$$

Combining equations (19) and (25) gives Y' + Y" and combining equations (20) and (26) gives Z' + Z". Since the scale pointers on the transducer had to be offset from the Z and Y pivots these offsets were measured (Y''' and Z''') and added to give the defect tip (G) coordinates (Y' + Y" + Y''', Z' + Z" + Z''').

5.0 Specimen Preparation

Specimens were machined from 23.3 mm thick, hot rolled, A1030 steel plate. Surface notches were machined halfway along these plates using a slitting saw, 38 mm diameter and 0.152 mm thick. Two or three overlapping saw cuts were made, Fig. 26, and the plates were then subject to repeated, three or four-point bending fatigue as shown schematically in Fig. 2a. Since this generates a very high cyclic stress intensity factor at the intersection of the overlapping sawcuts one gets early initiation of a fatigue crack from a known position. By continuously monitoring crack opening displacement during the fatigue cycling one can, with experience, assess how far the fatigue crack has grown. A similar approach using local bending and two or more overlapping sawcuts has been used to grow fatigue

cracks in the radial-circumferential plane of girth welds of large diameter pipes used for full-scale fracture tests.

When the fatigue crack in a plate had grown to the desired size it was sized ultrasonically. In some cases the starter notches were then machined off and the sizing experiments were repeated. After the sizing experiments had been completed, the specimen was cooled in liquid nitrogen and fractured in the plane of the fatigue crack. Figure 3 shows some fatigue cracks revealed in this way. In two cases, plates 11 and 12, the starter notches have been machined off.

It was our hope that the above technique could be used to grow regular or irregular cracks, depending on the starter crack geometry. We have not succeeded in growing a fatigue crack with a noticeably irregular front. Some of the starter notch geometries tried are shown in the second progress report (Sept. 81). In all cases the cracks quickly assumed a regular geometry or led to total failure of the plate. This was time-consuming and very frustrating. Although we would still like to size irregular fatigue cracks we have been forced to use irregular defects produced by electrical discharge machining (EDM) with thin foils. Fig. 19 shows three irregular EDM defects that have been sized.

The first defect, EDM 1, was machined using a 0.005 inch thick foil. This proved to be too thin a foil so it was difficult to flush the defect as its depth increased. This poor flushing significantly increased the frequency of contact between the foil and plate and led to a series of ridges on the cut face. These ridges made it very difficult to size this defect.

The second defect, EDM2, was machined using a 0.010 inch thick foil but it was still difficult to flush the crack and ridges were again produced parallel to the defect front. The roughness of this ridged surface is much greater than that produced by fatigue crack growth so the problems encountered when sizing this defect are unlikely to be representative of those encountered when sizing fatigue cracks [4].

After various experiments a jet flushing system was devised for the EDM unit and another defect, EDM 3, was cut with a 0.010 inch foil. This eliminated most of the "ridging" discussed above.

All of the planar defects described above were surface defects in parent material. The procedure used to prepare a 'buried' planar defect emanating from a weld is shown schematically in Figures 20 and 21a. First a surface fatigue crack was prepared using the procedure described above. Then the starter notch was enlarged by milling to form a Vee, Fig. 20a. This Vee was then filled with weld, Fig. 20b, and a check made on the ultrasonic response of this 'near-surface' buried defect. Finally, a series of weld passes were made to build up the plate thickness, Fig. 21a. With this type of buried defect it was possible to identify signals from the 'fatigue' tip and from the tip formed at the base of the Vee by the fatigue crack and weld root.

6. Experimental Results and Discussion

6.1 Sizing Fatigue Cracks in Plates 11 and 12 with $\theta xz = 0$

Fig. 3 shows two plates, 11 and 12, that were inspected before and after machining off the starter notches. Then pure compression was

applied normal to the plane of the fatigue crack. The maximum compressive load applied was 200,000 lb (0.89 MN). This produces a nominal compressive stress slightly below minimum yield for this material.

The scanning system described in section 3.1 was used to inspect these plates. The Krautkramer MB-4T, 4MHz probe was used with mineral oil as the couplant with a standoff h of 46.25 mm and $\theta = 16.17°$. First consider some of the ultrasonic data obtained from plate 11.

6.1.1 Plate 11 without Compressive Load Applied

Fig. 22 presents time of flight measurements taken before any compression was applied. The data was obtained with the probe at various z (lateral) positions, both before and after machining off the starter notches. As mentioned previously the probe was moved in the y direction until the echo from the crack tip reached a maximum. The time delay in receiving this echo is measured and used as the sizing parameter. As the probe is moved in the y direction, one also sees a maximum for the echo received from the corner formed by the defect and the back surface of the plate. The time delay in receiving the corner echo is also shown in Fig. 22. It can be argued that the time difference between the two sets of corner signal data is equivalent to the material machined off (3.5 mm) so one has an alternate calibration for the tip 'time of flight' data on Fig. 22. Using this calibration procedure gives a prediction of 6.2 mm for the maximum crack depth (after the notch had been removed) compared to 7.1 mm measured optically after fracturing the plate, Fig. 3.

6.1.2 Plate 11 with Compressive Load Applied

The probe was positioned in the middle of the defect (Z = 0) and compression was applied in steps up to a total load of 200,000 lb (0.89 MN) and then removed in steps. Figure 23 presents echo amplitude data obtained during this loading and unloading. It shows that a compression of 80,000 lb (0.356 MN) (a nominal compressive stress of 14,235 lb/in^2 (98.15 MPa)) reduced the corner amplitude by about 8 dB and that further compression did not have much effect on corner amplitude. Figure 23 also shows that compression had a similar effect on tip echo amplitude, which of course makes identification of the tip echo more difficult.

It will be noticed that the unloading amplitudes are consistently lower than the loading amplitudes. This implies that there was some permanent 'closure' of the crack. When this loading-unloading cycle and measurements were repeated a second and third time there was no further change, i.e. echo amplitude measurements taken during subsequent loading and unloading were essentially the same.

Although compression reduced the corner and tip echo amplitudes it had no significant effect on times of flight from the corner and tip. Fig. 24 presents some of the time of flight data recorded at Z = 0 during these three loading-unloading cycles on plate 11. For convenience of presentation, only one set of corner data is shown and to avoid confusion the three sets of tip time data are shown on separate ordinate scales.

During the third loading-unloading cycle the compression was held at 245 MPa for a while to permit a scan along the crack front in the z direction. The corner amplitudes measured were between 9 and 15 dB compared to 23 to 26 dB observed before any compression was applied to the specimen. It was not possible to identify the tip echo when the probe was moved laterally away from z = 0. ie the centre of this crack. This was unexpected so it was decided to repeat the study outlined above using plates containing similar fatigue cracks. All of these subsequent studies have confirmed the trend of the data shown in Figs. 22, 23 and 24. However, in all of these subsequent studies it was possible to hold the compression at near yield nominal stresses, i.e. 245 MPa, and identify the crack tip echo over a significant part of the crack front.

6.1.3 Plate 12 with and without compressive load applied

For example Fig. 25 presents corner and tip echo amplitudes obtained from plate 12 (see Fig. 3 for crack shape). First the amplitudes were measured with the starter notches present. Then the starter notches were machined off and the measurements repeated. Finally, during the last of three loading-unloading cycles, the compression was held at 245 MPa and the probe was scanned laterally. Clearly the part of the crack front over which tip signals could be identified, was not significantly reduced by the application of the compressive load.

Figure 26 presents the time of flight data obtained from plate 12. It shows that the compressive load had little or no effect on the time delay in receiving the crack tip echo. As mentioned earlier the

time delay unit devised for these experiments has a resolution of 0.2 μ sec. This and the human judgement required when using its selector switches to gate the crack tip echo, leads us to expect a scatter of about ∓ 0.4 μ sec in such time measurements. This explains most of the scatter in the measurements of time of flight of tip echoes evident on Fig. 26; in these experiments a scatter of ∓ 0.4 μ sec is equivalent to a scatter of ∓ 0.5 mm in defect depth compared to a maximum defect depth of 5.3 mm after removing the starter notch.

As mentioned previously the scanning rig (section 3.1) used to inspect plates 11 and 12 inclines the probe at $\theta_{xz} = 0$. This constraint on θ_{xz} and the curvature (angle B) away from the centre of the fatigue crack in plate 12 (Fig. 3) probably explains why crack tip signals could only be obtained (Fig. 26) over the middle 15-20 mm of its 44 mm length.

Soon after completing these experiments on plate 12 the more sophisticated scanning rig (section 3.2) was built. After it had been calibrated using bottom-drilled holes, see section 3.2, it was used to further investigate the effects of crack front curvature and compression normal to the defect plane.

6.2 Sizing a 'regular' EDM defect with the twin-probe technique

As a first check on the twin-probe technique, an EDM equivalent of plate 12 was inspected with no compression on the defect. The actual profile of this EDM surface defect is compared on Fig. 27 with predictions from measured times of flight. For convenience both of the twin probes were used to make scans at various settings of $\theta_{x'y}$ and θ_{xz}. See Fig.

4 for definition of right and leftside 'probe' and Table 2 for details of probe settings.

Since these were the first measurements taken with angle probes, it was decided to replicate the measurements, before breaking open the plate to obtain the actual profile. This replicate set of data, Table 3, is compared on Figure 28 with the actual profile.

In both tests it was possible to identify the defect tip echo over almost all of the defect front. In both tests the rightside probe gave a more accurate sizing; the reason for this is still not clear. Nevertheless the overall agreement between actual and predicted profile was encouraging so the next step was to use the twin probe concept to size a surface fatigue crack using the same approach.

6.3 Plate 21 with and without compression applied to the fatigue crack

Five detailed studies were made of this surface fatigue crack. In two studies (identified as ULDAT 1 and ULDAT 2) measurements were taken with no compression applied to the crack. ULDAT 1 data was taken by J. Kervin and ULDAT 2 data was taken by G. Hewitt; ULDAT 1 was a much more comprehensive scan taken after ULDAT 2 had been analyzed.

Experiments ULDAT 3, 4 and 5 were made with a compressive normal force applied to the crack during the ultrasonic measurements. After reviewing previous experiments with a compressive force with θ_{xz} always set at zero (see data for plates 11 and 12) it was decided to conduct ULDAT 3, 4 and 5 with normal forces of 40,000, 100,000 and 200,000 lb. respectively.

The data obtained in these five studies is presented in Figs. 29-33. In each study various scans were made by the left side probe and by the right side probe. The results of scanning with a particular setting of $\theta_{x'y}$ and θ_{xz} are shown with a distinctive symbol. The settings and symbols are correlated in Table 4.

Figs. 29 and 30 show the data obtained by the two operators, with zero compression applied to the crack. A 'mean' line is shown for each operator's experimental data; these mean lines will be compared later with the mean lines from ULDAT 3, 4 and 5. Both operators obtained mean predicted crack depths smaller than the actual depths. If one uses maximum rather than mean predicted depths the predictions are within about 1 mm of the actual depth. In both cases the maximum was at a lateral position of about 1.45 to 1.65 and in agreement with the position of the maximum for the actual defect.

Figs. 31 - 33 show the data obtained at compressions of 40,000, 100,000 and 200,000 lb. respectively. At a compression of 200,000 lb. it was much more difficult to identify the crack tip signal particularly on the right side so relatively few measurements could be taken. Fig. 33 also compares the mean line through ULDAT 5 data with mean lines from Figs. 29-32.

In all cases applying the compression made it more difficult to identify the crack tip signal but at 40,000 and 100,000 lb. the crack depth predictions are very similar to those obtained at zero compression. The maxima are similar and a comparison of mean lines, Fig. 33, reveals very little difference.

If one thinks of these compressions as "residual stresses" tending to close a crack, these experiments suggest that residual stresses of the order of 40,000/plate area and 100,000/plate area i.e. 5700 to 14,300 lb/in^2 do not stop one using this sizing method. Another interpretation of the results is that 'pre-service' measurements, taken with a residual stress of 5700 to 14,300 lb/in^2 present, should be similar to 'in-service' measurements taken after residual stresses have decayed to a negligible level because of long-term operation at higher temperatures. This would not be the case if echo amplitude measurements had been used to size the defect; the 'in-service' amplitude would be larger and give the impression that the defect had grown. This is false since such changes in echo amplitude are due to crack opening rather than crack growth.

6.4 Plates 22 and 23 with buried fatigue cracks

The procedure used to prepare these defects has already been described, see section 5 and Figure 20 and 21a. When the defects had been sized ultrasonically, the plates were sectioned and polished. Sections were made at 90° to the plane of the defect. Photographs of these sections are shown in Figures 34 and 35. One of the sections was etched to reveal (Figure 35b) the interfaces between the weld, heat affected zone and fatigue crack.

Some of the sections on Figures 34 and 35 show lack of penetration or slag at the weld root. It should be noted that some of the photographs on Fig. 34 (22-1, 22-2 and 22-10) have a higher magnification

and that Figures 34 and 35 have different magnifications. If one requires the magnifications they can be calculated using the data on Figures 36 and 37. These show defect depth and location and were measured from the polished sections using the front (non-welded) surface of the plate as the reference surface. These measurements have been used to prepare crack tip and weld root (tip) profiles for comparison with profiles calculated from 'time of flight' measurements. First consider the ultrasonic data obtained from plate 22.

6.4.1 Sizing of defect in plate 22

As mentioned previously the first step in preparing this defect was to grow a surface fatigue crack in the plate. It was then inspected (using the twin probe rig) to confirm that the crack was a reasonable size. This ultrasonic data is shown in Fig. 38.

The next step was to enlarge the starter notch to form a Vee and then fill the Vee with a root pass, see schematic Fig. 20b. It was inspected again, Fig. 39, to see if this welding operation had produced any changes in the response of the fatigue tip. A comparison with Fig. 38 shows that there was no significant change.

Finally a series of weld passes were made to build up the weld, see Fig. 35b for typical cross-section. Time of flight measurements were than taken to identify the locations of the fatigue tip and of the tip formed at the base of the Vee by the fatigue crack and weld root. These ultrasonic profiles are compared on Figure 40 with the actual profiles determined by sectioning (see Fig. 36). If one uses maximum rather than

mean predictions of depth there is very good agreement between predicted and actual "tip" positions for this buried defect.

A comparison of Figures 38, 39 and 40 suggests that the weld passes used to build up from the root pass have 'opened' the fatigue tip; in particular the maximum depth on Fig. 40 is 1.8 x 10^{-2}m compared to 1.6 x 10^{-2}m on Fig. 38 and 39. One interpretation of this is that the original surface fatigue crack, Fig. 38, was undersized by about 2 mm. It is interesting to note that surface fatigue crack in plate 21 was also undersized by about 2.0 mm. This observation and the obvious advantages of repeating any experiment led us to prepare another buried defect. This defect in plate 23, Fig. 37, was smaller than that in plate 22, Fig. 36.

6.4.2 Sizing of defect in plate 23

As before the first step in preparing this defect was to grow a surface fatigue crack. This was inspected to confirm that it was a reasonable size, Fig. 41. Then the welding procedure outlined earlier was followed and the finished defect inspected, Fig. 42. Again if one uses maximum rather than mean predictions of depth, Fig. 42, there is very good agreement between predicted and actual "tip" depths for this defect.

Although it is not as obvious as it was with plate 22, there is an indication that welding over the surface defect has 'opened' the fatigue tip. This can be seen if one compares the spread of the data on 41 and 42.

This was the last of the experiments on surface and buried defects having 'regular' shapes. In all cases where the 'twin-probe' technique was

used it was possible to 'see' . steeper parts of the crack front. The reader will have noticed that a range of θxz values rather than two set values were used in these experiments. This was done to glean the maximum information from each specimen. The information obtained indicates that it may be very wise to do this anyway, either by using more than two probes or by making several scans with changes in the θx'y and θxz settings of the twins after each scan.

6.5 Sizing of irregular defects

As mentioned in section 5 an attempt was made to grow surface fatigue cracks with an irregular shape. This was very time consuming and unsuccessful. Therefore sizing experiments to date have used irregular defects produced by electrical discharge machining. Fig. 19 shows the three EDM defects that have been sized; section 5 discusses how they were machined and the surface features that proved to be a nuisance.

As mentioned in section 2.2.2, these defects were sized using contact probes because the new immersion rig was being modified at the time. All of the data presented in this section was obtained using a 2.25 MHz, 1/2 inch probe with 45 wedges (see Section 2.2.2 for details).

6.5.1 Sizing of defect EDM 1

Fig. 43 presents the data obtained in three experiments (A,B,C) on this defect. The actual profile of the defect is shown alongside plots of time of flight vs location along the defect. To avoid the need to refer to calibration curves, some of the key measurements of time are shown with their equivalent defect depths in parenthesis above them.

Fig. 43A shows the data obtained with the large 45° wedge. Fig. 43B shows the data obtained with the small wedge and Fig. 43C data obtained when this wedge was rotated through a small angle θxz. Figs. 43A-C show that it was not possible to follow the profile of this defect with this probe. Over the very shallow part of the defect (2 mm) the tip signal could not be identified and over the deepest part, the times change in the opposite way to that anticipated for this curvature. The tip signals were very difficult to identify because of reflections from nearby ridges. Nevertheless the ultrasonic measurements of depth were 7 to 8.6 mm and the actual maximum was found to be 7 mm when the plate was broken open.

6.5.2 Sizing of defect EDM 2

This defect was intended to have the same profile as EDM1 but to be of greater depth. As mentioned previously it was cut with a 0.010 inch whereas EDM1 was cut with a 0.005 inch foil. Fig. 44 presents the data obtained in two experiments on this defect. Fig. 44A presents the data obtained with the large wedge and Fig. 44B the data obtained with the small wedge. Both of these figures show that, at some locations along the crack front, two distinct crack tip signals were identified. One set of these crack tip signals (those with the larger times of flight (⊗)) give predictions of crack depth which are reasonably near to the maximum measured when this plate was broken open. The set of crack tip signals with the shorter times of flight (●) give predictions of crack depth which are 4 to 6 mm larger than the maximum (8.5 mm) measured when

the plate was broken open. The only explanation we can offer for this is that the ridges near the crack tip led to significant mode conversion. Hindsight suggests that it would have been useful to scan from both sides of the crack to see if these 'higher velocity' signals were only produced by one side of the defect.

6.5.3 Sizing of defect EDM3

A result of improving the flushing of the EDM machine was that it was possible to machine deeper defects. This defect EDM3 had a maximum depth of 12 mm and a minimum depth of 7 mm. To assist in the identification of spurious signals it was decided to scan from both sides of this defect (see schematic below).

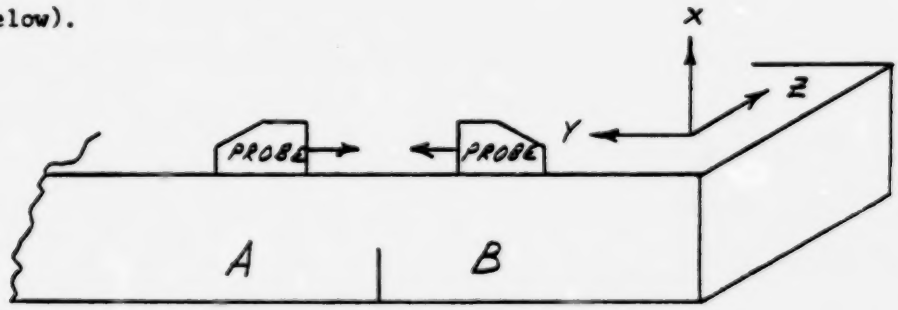

Scanning from side A and then from side B gave the data shown in Figs. 45 and 46 for the small wedge and large wedge , respectively. In all cases there are clear indications of maxima and minima in crack depth and the predicted crack depths (shown in parenthesis above the times) are in reasonable agreement with the machined depths.

The experimental data presented in Figs. 45 and 46 was obtained by moving the transducer laterally (Z direction on schematic above) in steps of 3 mm. As a further check, scans were made from one side using smaller

(1 mm) laternal steps and a higher sensitivity. Figs. 47 and 48 show the data obtained with the large and small wedges respectively. In both cases the maxima and minima in the defect profile was detected but, spurious signals (X) were much more of a nuisance when using the small wedge.

These results for irregular EDM defects emphasized the need for a detailed study of the influence of crack front curvature (angle β) and it was decided that this could be more easily obtained by using EDM or fatigue defects of regular shape with significant curvature. Hence the next step chronologically was to use the twin-probe immersion rig to size the EDM defect, section 6.2, and the fatigue crack in plate 21, section 6.3. At the same time a single probe ($\theta xz = 0$) was used to size a part-circular surface slot cut with a milling saw. The angle β was measured at points along the front of this defect and correlated with the operator's experience when trying to identify the crack tip signal. This and the experiments described in sections 6.2 and 6.3 suggest that the defect tip signal can no longer be identified with a probe set at $\theta xz = 0$, if the angle β exceeds about 23°.

Obviously it would now be desirable to prepare an EDM defect similar to EDM3 and size it using the twin-probe rig with the twins set at various values of θxz. It would be even more desirable to try this approach with an irregular fatigue crack if a technique for growing it can be developed.

6.6 Measurement of Surface Length of Fatigue Cracks

In previous sections of this report, the emphasis has been on finding the maximum depth and general shape of EDM defects or fatigue cracks. As

mentioned previously it is difficult to identify the crack tip signal at the end of a defect if the curvature is steep. Also when the defect depth is less than 2-3 mm it is difficult to separate the crack signal from the corner signal.

In view of the above limitations, the lengths of some defects were also measured using the corner echo amplitude as the sizing parameter. Only the data for plate 21 will be reviewed here since there has already been a detailed discussion of time of flight data for that plate, see 6.3.

Figure 33 compares the mean profiles obtained from time of flight data with the actual crack profile measured after breaking open the plate. In the very comprehensive study with no compression on the crack (ULDAT1), the time of flight data, Fig. 29, shows very clearly the "loss of tip signal" regions at the ends of the crack. This effect was even more pronounced in the other tests on this plate because of operator inexperience (ULDAT2) or crack closure (ULDAT3-5). At best, this very comprehensive set of 'time of flight' data predicts a crack length of 95-97 mm compared to an actual length of 126 mm.

During the tests at zero compression (ULDAT 1) and at a compression of 40,000 lb (ULDAT3), measurements were also taken of corner echo amplitude. There are presented in Figures 49 and 50 for ULDAT1 and ULDAT3 respectively. If one defines the ends of the crack as the positions where the echo amplitude is 20% of the maximum, then these measurements lead to crack length predictions of 111 mm and 117 mm compared to the actual length of 126 mm.

7. Discussion

7.1 Effects of compression on ultrasonic response

Studies on plates 11, 12, and 21 and others not discussed herein, show that compression normal to a surface fatigue crack significantly decreases the amplitude of the corner and crack tip echoes, eg. Fig. 23. The implications of and reasons for this reduction in corner echo amplitude have been considered in detail by Wooldridge et al [4,8,9] of the C.E.G.B., Non Destructive Testing Applications Centre, Manchester.

Of particular interest here are their experiments on fatigue cracks in mild steel parent plate and weld metal [9]. These through-thickness cracks were grown under constant stress intensity conditions and examined with compressive stresses, up to 150 MN m^{-2}, normal to the crack plane. Measurements of corner echoes were made using shear waves generated by 4-5 MHz contact probes, with angles of 45, 60 or 70° and crystal diameters of 10-12.7 mm. Some of their conclusions were (quote):

(1) The growth conditions of fatigue cracks have a significant effect on their ultrasonic response, both at zero load and when under compressive stress. The (range of) stress intensity factor, ΔK, during crack growth correlates well with the roughness of the fatigue crack surfaces and this is believed to cause the changes in ultrasonic (corner) response.

(2) Both increasing crack roughness and increasing compressive stresses reduce the specular reflection from fatigue cracks. Decreases of up to 10 dB may be caused by crack roughness while large compressive stresses may cause decreases of up to 20 dB. However, the two

effects are not cumulative as the roughest cracks show little variation with stress. To some extent it may be possible to compensate for these effects by increasing the test sensitivity, but this will be limited in practice by the number of insignificant inclusions which give ultrasonic echoes similar in amplitude to those from cracks.

(3) If echo amplitude comparison techniques like DGS are used, then variations in compressive stress or crack roughness will lead to appreciable sizing errors. The reduced response may also result in defects being missed entirely if an echo amplitude threshold is used to define recordable defects.

(6) The presence of liquid in a crack causes a marginal increase in reflection for shear wave beams incident at 20° to the crack normal. Modest decreases in reflection occur for beams incident at 45°, while considerable decreases are likely at 30° incidence.

(7) Although compressive residual stresses may lead to cracks being undersized, fracture mechanics predictions of growth rates may nevertheless be conservative because these stresses reduce the resultant stress intensity at the crack tip.

During these tests, they also looked for the crack tip echoes and came to the conclusion that:

(4) Crack tip echoes are small; typically they are 50 dB down on a back wall echo at the same range when using a compression wave probe at grazing incidence, and they are practically impossible to identify if the cracks are in compression or if the material contains other defects such as inclusions.

Their conclusion is not supported by the data presented herein for surface (part-through thickness) fatigue cracks sized with compression normal to the crack. Although there was a significant decrease in crack tip echo amplitude in our compression tests, it was usually possible to identify the crack tip echo over the central (deepest) part of the surface crack.

It is pertinent to ask if this disagreement is caused by differences in fatigue crack growth conditions between their through-thickness cracks and our part-through thickness cracks. This is unlikely since Wooldridge and Steel also noted that "in contrast to the crack corner echoes, the tip echoes show little dependence on the crack growth conditions. The scatter in signals from cracks of the same roughness but varying depth is as large as that from cracks of the same depth but different roughness. During fatigue growth a residual plastic zone is set up in the region of the crack tip [10] and the size of this zone depends on ΔK. It has been suggested by Silk [11] that crack tip echoes are determined by plastic deformation around the crack tip but our results indicate that the size of this plastic zone does not have a very significant effect on the crack tip echo."

If this observation by Wooldridge and Steel is correct one wonders if differences in crack closure between through-thickness and part-through thickness cracks explains these differences in identification of the crack tip echo.

7.2 Diffraction Sizing Techniques using probe as a transmitter-receiver

As anticipated a single probe acting as a transmitter-receiver is of limited use when trying to identify the crack tip echo from 'steep' parts of a crack front. Experiments indicate that the defect tip signal can no longer be identified with a probe set at $\theta xz = 0$ if the curvature angle, β, exceeds about 23°.

This problem was reduced by scanning with twin-probes; one inclined at $\theta xz = 0$ and the other at some inclination ($\theta x'y$, θxz) so that it receives tip signals from the steeper parts of the crack front. Making several scans with changes in the $\theta x'y$ and θxz settings after each scan has proved to be a very useful way of providing a profile of surface and buried fatigue cracks. When maximum rather than mean predictions of defect depth are compared to actual depths, the predicted depth at the deepest point is usually within about 2.0 mm of the actual depth.

It is particularly difficult to identity the crack tip signal from the ends of defects, particularly if the curvature is steep. When sizing the fatigue crack in plate 21, plots were also made of the variations in corner echo amplitude as the probe was traversed along the crack. These plots and the well known "20% of maximum amplitude" rule for defining the ends of the crack proved to be a better method for assessing surface length, with or without compression normal to this crack.

The above observations serve to emphasize that it is probable that the maximum benefit will be obtained from diffraction techniques if they are used in conjunction with some of the more sophisticated echo amplitude

techniques. Unfortunately time did not permit a more detailed look at this concept.

As mentioned in the introduction there are situations (geometries) where the above technique is the only one suitable for looking at the time of flight of the crack tip echos. If geometry permits there may be considerable advantage in using the separable probe technique developed by Harwell. For example if it had been used to scan the irregular EDM defects, section 6.5 it is unlikely that the surface ridges near the defect tip would have confused the tip signal and given the impression there were two tip signals. Since the Harwell 'separable probe' technique is at a very advanced stage of development it merits a more detailed discussion here.

7.3 Harwell 'separable probe' diffraction technique

A recent UKAEA, Harwell, report [12] describes a system for recording the ultrasonic signals digitally on a floppy disc and then displaying the information in various formats on a video monitor.

The basic arrangement of the probes is shown in Figure 1. They say that it is usual to calibrate the time scale by reference to a lateral wave which runs just below the surface of the specimen directly between the two probes, or to the backwall echo from the bottom of the specimen. Since there may also be other signals due to Rayleigh waves and to mode conversions at the material surfaces, they say that it is important to calculate approximate arrival times and verify that the part of the waveform being digitised is correct.

They say that Krautkramer G4KB, 5 MHz probes have been found suitable for a wide range of applications. However their reports imply that

frequencies of 2.5 to 5 MHz have been used successfully and note that on one occasion they used 15 MHz probes with a separation of less than 4 mm to size slits of 1 mm depth to an accuracy of $\pm$ 0.05 mm.

For cracks near the surface, one can improve the resolution by using higher frequency probes and by reducing the probe separation, 2S. To illustrate the effect of probe separation, 2S, and timing error, Δt, Carter and Slesenger [12] prepared the graph shown as Fig. 51. A timing error of 50 ns or 25 ns was assumed because this corresponds to a full or half sample interval of the digitiser in their system.

However in general the probe separation should be about twice the depth of the specimen in order to see most of the depth. Therefore if small, near surface defects are suspected a special scan with small probe separation is obviously in order, Fig. 51. Also for thick plates the finite beam-spread of the probes limits the range of depths which can be effectively inspected for a given probe separation and angle. Thus for plates greater in depth than 10 cms a number of scans may have to be used with different probe separations to cover different levels in the thickness.

In their report [12] Carter and Slesenger present several examples of the video display of the data collected in automated scans of various cracked samples. In another recent report Silk et al [13] present data obtained some years ago by hand scanning one of the PISC plates. The data was not presented until recently since the plate could not be sectioned until the round-robin program had been completed. They conclude that no significant defect was missed by the diffraction technique and that the defects were sized or located in through-thickness terms to an accuracy

of at least 7% of total plate thickness.

A second international POST-SMIRT seminar on "non-destructive examination in relation to structural integrity" was held at OECD headquarters in Paris, August 24-25, 1981. Of the papers presented four included some discussion of time of flight techniques. In one case [14] no preprint was distributed and in the other case [15] only an abstract and summary table of data (attached as Appendix 1) was available. In all cases the time of flight studies were done by Silk et al of Harwell.

The attached table of data (Appendix 1) summarizes the results of a collaborative program of the Welding Institute (UK); the NDT centre at AERE, Harwell and CEGB, NDT Applications Centre. Most of the data was obtained from defects in butt welds in flat plates of a ferritic steel. The crack-like defects were introduced during the welding process to simulate solidification cracking, lack of fusion and HAZ cracking. In general the defects were 1-10 mm size but some were as large as 35 mm.

In their abstract, Mudge and Jessop comment "that the 20 dB drop and maximum amplitude methods can considerably underestimate defect size and there is no correlation between AVG (DGS) size measurement and overall size. On the other hand, a novel diffraction technique employing time of flight measurement (separable probes) markedly improved the accuracy and precision of size measurement". Their raw data which was presented in slides, showed this very clearly. The table of data, Appendix 1, masks the problems to some extent because they prepared it on the assumption that each set of data was normally distributed. This assumption was obviously nonsense for the DGS data and I suspect that it was wrong for some of the other data sets. Mudge agreed with my observation and mentioned that a statistician was reanalysing the data.

In their paper [16] on reliability assessment of austenitic steel inspections, Bell et al of UKAEA, Risley discuss experiments on 14 defective welds in 50 mm thick, type 316 stainless steel plate. Figure 52 shows the disposition of weld runs and the believed positions of the defects in the cross-section. Their comments on Silk's measurements are "By and large the sizes attributed using the 'Time of Flight' technique to defects detected by other means are in encouraging agreement with the results of the destructive examination and comparable in accuracy with similar data from ferritic welds but two particular areas for further study are indicated by the results. These are, firstly, examination for small surface breaking defects where the tip diffraction pattern may be difficult to identify against the reflected back wall echo and secondly, large curved defects of the type represented by that in specimen 864 (Fig. 52). This was actually associated with a small satellite defect and was not easy to identify in the test record. Thus for a 45° nominal beam angle it was not possible to simultaneously record the diffracted signal from both extremities of the defect from either surface of the weld. Each extremity could only be clearly detected from one surface.

In another paper [17] Bell comments that "An interesting and potentially important suggestion arising from this work has been the possibility that the use of wide angle transducers with the time of flight technique may make it less susceptible to the grain structure of a weld than the pulse echo techniques and consequently that it should be considered for defect detection as well as sizing. AERE Harwell are examining this possibility further."

None of the other papers presented at the OECD meeting contained quantitative information on time of flight techniques. Some participants said that in their experience it was often very difficult to identify the crack tip signal. In my opinion there is already ample evidence that it is a very useful sizing technique and the research team at Harwell are very convinced that it can be applied in the field.

8. Conclusions

1) Echo amplitude measurements on steel plates containing surface (part-through thickness) fatigue cracks, and data published by others for through-thickness fatigue cracks, show that a compressive stress normal to the crack plane reduces the specular reflections. If echo amplitude measurements are used to size fatigue cracks, this reduction in specular reflections is likely to lead to undersizing.

2) Measurements on steel plates containing surface fatigue cracks also show that a compressive stress normal to the crack plane reduces the amplitude of the crack tip echo. However in most cases it was still possible to identify the tip echo over the deepest part of these surface cracks and size the defect using the time delay in receiving the tip echo.

3) Surface and buried fatigue cracks in steel plates have been sized using immersion probes as transmitter-receivers, angled to produce shear waves in the cracked steel plates. In almost all cases it was possible to identify the crack tip echo and predict the crack depth from time delay measurements.

4) Identification of the crack tip echo is very dependent on the curvature of the crack front over the section 'seen' by the ultrasonic beam. Making repeat scans, with changes in the probe angular settings (θxz and $\theta x'y$) after each scan, makes it much easier to identify the tip signal from steeper parts of the crack front.

5) Making repeat scans and using maximum rather than mean predictions of defect depths gives predicted depth, at the deepest point that are within about 2 mm of actual depth. The fatigue cracks sized were between 5 and 16 mm deep at the deepest point.

6) It was not possible to identify the crack tip signal from the ends of a crack because of steep curvature and small (< 3mm) defect depth. Therefore the 20% of maximum (corner) amplitude rule proved to be a better method for assessing the surface length of one of the fatigue cracks (with or without normal compression).

7) The aforementioned diffraction technique uses shear waves and probes acting as transmitter-receivers. A diffraction technique developed by AERE, Harwell uses two probes, one acting as transmitter and the other as receiver. A literature survey and visits to Harwell and other laboratories shows that this separable probe technqiue has been developed to the stage where it can be used in the field.

8) If the crack tip echoes can be identified, these diffraction technqiues are intrinsically more accurate than echo amplitude techniques for sizing.

Acknowledgments

My assistants during this project were T. Vainionpaa, J. Kervin and G. Hewitt. All three are undergraduates who worked on this project during their work-terms; their assistance is gratefully acknowledged. During one work term J. Kervin was partly funded by an Undergraduate Summer Research Award from the Natural Sciences and Engineering Research Council. The interest and advice of Dr. M.A. Mahmoud is also acknowledged; he is now an assistant professor at the State University of New York, Buffalo.

Visits to CEGB research laboratories, Berkeley and Manchester and to UKAE Harwell were made; their staff are thanked for these very useful discussions and demonstrations.

References

1) Dalrymple, D.G., "AECL Research and Development in Piping System Non-Destructive Testing", p. 301-308. Proc. of International Conference on Pipeline and Energy Plant Piping, Calgary, November 1980. Pergamon Press.

2) Silk, M.G., "The fundamental sources of error in ultrasonic defect sizing". Proc. of European Conference on N.D.T. Mainz, 1978.

3) Mahmoud, M.A.M. "Ultrasonic Sizing of Surface Defects in Plates and Pipes". Ph.D. thesis, University of Waterloo, Dec. 1980.

4) Wooldridge, A.B., "The effects of compressive stress and contaminating liquids on the ultrasonic detection of fatigue cracks." Revue du CETHEDEC-NS80-2, 1980.

5) Silk, M.G., Lidington B.H. and Hammond, G.C. "A separable probe technique for accurate crack sizing using ultrasonic diffraction" UKAEA Harwell Report AERE-R-9252, November 1978.

6) Mahmoud, M.A.M. and Burns, D.J., "Some Canadian Developments in Ultrasonic Inspection", Proc. of 2nd Intnl. Post-SMIRT Seminar on Non-destructive examination in relation to structural integrity, OECD, Paris, 1981, to be published by Applied Science Publishers Ltd

7) Hartung, H.F., Burns, D.J. and Pindera, J.T. "Ultrasonic Monitoring of Growth of Part-through thickness defects at 290 C". ASME Jnl of Engineering for Power, Vol. 101, p. 471-476, 1979.

8) Wooldridge, A.B., "The Effects of Compressive Stress on the Ultrasonic Response of Steel-Steel Interfaces and of Fatigue Cracks" C.E.G.B. Report NW SSDRR4279, April 1979.

9) Wooldridge, A.B. and Steel, G. "The Influence of Crack Growth Conditions and Compressive Stress on the Ultrasonic Detection and Sizing of Fatigue Cracks", C.E.G.B. Report NWSSDRR4580, April 1980.

10) Knott, J.F. "Fundamentals of Fracture Mechanics", Butterworths, 1973.

11) Silk, M.G., "The transfer of ultrasonic energy in the geometry of the diffraction technique for crack sizing." U.K.A.E.A. Harwell Report AERE-R-8665, March 1977.

12) Carter, P. and Slesenger, T. "Harwell Ultrasonic Flow Detection and Sizing Equipment with Digital Recording", UKAEA Harwell Report AERE-R-10386, December 1981.

13) Silk, M.G., Lidington, B.H. and Hammond, G.C., "A Comparison betwee ultrasonic Diffraction Data and Destructive Analysis for the PVRC Plate Number 51/53". UKAEA Harwell report AERE-R-9761, July 1981.

14) Silk, M., Developments in UK in ultrasonic inspection of RPV weldments. Session 2 of 2nd International Post-SMIRT Seminar on Nondestructive examination in relation to structural integrity, OECD Headquarters, Paris, Aug. 1981, Proc. to be published by Applied Science Publishers Ltd.

15) Mudge, P.J. & Jessop, T.J., "Size Measurement and Characteristics of Weld Defects by Ultrasonic Testing-Findings of a Collaborative Program," Ibid ref. 14, session 6.

16) Bell, I.P., Gray, B.S., Hudgell, R.J. and Sargent, T., "Reliability Assessment of Austenite Steel Ultrasonic Inspections" - Progress report on a UKAEA program, Ibid ref. 14, session 5.

17) Bell, I.P. & Gray, B.S., "Developments in the UK on ultrasonics for austenite steel weldments." Ibid ref. 14, session 3.

APPENDIX 1

SIZE MEASUREMENT AND CHARACTERISATION OF WELD DEFECTS BY ULTRASONIC TESTING:- FINDINGS OF A COLLABORATIVE PROGRAMME

By P. J. Mudge and T. J. Jessop

The Welding Institute, Cambridge, England

Quantitative assessments of a fabrication's fitness for purpose using fracture mechanics rely on information on defect position, size and type supplied by shop or site non-destructive testing (NDT). Measurement of defect depth is invariably achieved by the use of ultrasonics. However, few data exist which enable the accuracy of ultrasonic size measurement to be assessed. Errors of defect measurement may have a considerable influence on the validity of subsequent fracture analysis.

This paper describes a collaborative programme, conducted in Great Britain by The Welding Institute, the NDT Centre at AERE Harwell and the Central Electricity Generating Board's NDT Applications Centre. The aim was to assess the performance of both conventional and more advanced ultrasonic testing methods for determining the size and type of a number of real weld flaws. Both planar and non-planar defects were studied in butt welds in ferritic steel of 38, 70 and 95mm thickness and in a small number of welds of more complex geometry.

It was found that there was a considerable scatter of size measurement results when compared with actual defect sizes for all methods. Overall trends and scatter of results were represented statistically by mean and standard deviation of the sizing errors, assuming the data to be normally distributed. These findings are summarised in the attached table. It can be seen that 20dB drop and maximum amplitude methods can considerably underestimate defect size, and there was no correlation between AVG (DGS) size measurement and overall size. On the other hand, a novel diffraction technique employing time of flight measurement markedly improved the accuracy and precision of size measurement, (as can be seen from the table the values of both $\bar{x}$ and σ are less than for other tests), although this requires further development to enable it to be used in the field.

The type of defect present is also an important consideration in assessments of fitness for purpose. However, it was found that while some defects produce characteristic responses which enables their type and shape to be determined, in many cases insufficient information is presented in the conventional A-scan display to produce a reliable diagnosis. Several storage and display systems capable of capturing and superimposing responses from defects such as B-scan and holography were included in the programme and these improved diagnosis of defect character.

These findings will be discussed in terms of their effect on assessment of defects, including the influence on the use of fracture mechanics to determine fitness for purpose.

Ultrasonic testing: defect cross-sectional size measurement accuracy

Test	Mean error $\bar{x}$, mm		Standard deviation, σ		95% confidence limits ($\bar{x} \pm 2\sigma$), mm		Sizing method
	Non-planar	Planar	Non-planar	Planar	Non-planar	Planar	
Laboratory 4MHz	-1.7	-2.3	1.9	2.6	+2.1 -5.5	+2.9 -7.5	20dB Drop 45°
Laboratory 4MHz	-	-2.7	-	3.0	- -	+3.3 -8.7	20dB Drop 60° +70°
Laboratory 4MHz	-2.1	-0.7	2.0	2.4	+1.9 -6.1	+4.1 -5.5	Maximum amplitude (all angles)
Laboratory 2MHz	-0.8	-1.2	2.3	3.4	+3.7 -5.5	+5.6 -8.0	Maximum amplitude (all angles)
B-scan 4MHz	-0.8	-1.8	2.1	3.0	+3.4 -5.0	+4.2 -7.8	20dB Drop (all angles)
Shop-floor 4MHz	-0.8	-1.0	1.4	3.1	+2.0 -3.6	+5.2 -7.2	20dB Drop (all angles)
Time-of-flight	-0.3	+0.5	1.0	1.8	+1.7 -2.3	+4.1 -3.1	Time measurement
Amplitude (DGS)	-2.7	-1.6	1.8	3.4	+1.5 -4.9	+5.2 -8.4	DGS (all angles)

Table #1.1 Calculated Results - Time of Flight
LEFT SIDE PROBE

Θ_{xy}'	Θ_{xz}	Θ_{xyz} Incidence	Θ_{xyz} Refracted	Surface Time	Hole #1 Time	Hole #2 Time	Hole #3 Time	Hole #4 Time	Corner Time
17.13	0	17.13	41.66	339	408	402	395	386	434
	0.5	17.14	41.68	339	408	402	395	386	434
	1.0	17.16	41.74	339	408	403	395	386	434
	1.5	17.19	41.84	340	408	403	395	386	434
	2.0	17.24	41.98	340	408	404	395	387	434
	2.5	17.31	42.17	340	409	405	396	387	434
	3.0	17.38	42.39	340	409	405	396	387	436
	3.5	17.47	42.65	341	409	405	396	388	436
	4.0	17.58	42.96	341	410	406	397	388	436
	4.5	17.69	43.30	341	411	407	397	389	437
	5.0	17.82	43.69	342	411	407	398	389	438
17.13	5.5	17.97	44.11	342	412	408	399	390	439
15.92	6.0	16.99	41.24	340	407	403	394	386	432
	6.5	17.16	41.75	340	408	404	395	386	433
	7.0	17.35	42.31	341	409	404	396	387	434
	7.5	17.56	42.90	341	410	406	397	388	435
15.92	8.0	17.77	43.53	342	411	407	398	389	437
14.79	8.5	17.01	41.31	340	405	403	394	386	432
14.79	9.0	17.26	42.03	341	408	404	395	387	433
14.79	9.5	17.52	42.79	342	409	405	397	388	435
13.74	10.0	16.94	41.10	340	406	403	394	386	432
13.74	10.5	17.23	41.95	341	408	404	395	387	433
13.74	11.0	17.53	42.83	342	410	406	397	388	435
12.63	11.5	17.02	39.49	341	407	403	395	386	432
11.52	12.0	16.58	40.07	340	405	401	393	385	430
11.52	12.5	16.94	41.10	341	407	403	395	386	432
10.48	13.0	16.64	40.26	341	406	402	394	385	431
9.33	13.5	16.36	39.47	340	405	401	393	385	430
9.33	14.0	16.77	40.63	341	407	403	395	387	432
8.34	14.5	16.68	40.38	341	407	403	395	387	432

Table #1.2 Calculated Results – Time of Flight
RIGHT SIDE PROBE

θ'_{xy}	θ_{xz}	θ_{xyz} Incidence	ϕ_{xyz} Refracted	Surface Time	Hole #1 Time	Hole #2 Time	Hole #3 Time	Hole #4 Time	Corner Time
16.88	0	16.88	40.94	339	408	403	395	386	431
↓	0.5	16.89	40.96	339	408	403	395	386	431
	1.0	16.91	41.02	339	408	403	395	387	431
	1.5	16.94	41.12	339	408	403	395	387	432
	2.0	16.99	41.27	339	408	404	396	387	432
	2.5	17.06	41.45	339	409	404	396	387	432
	3.0	17.14	41.68	340	409	405	396	388	433
	3.5	17.23	41.94	340	410	405	397	388	434
	4.0	17.33	42.25	340	411	406	398	389	434
	4.5	17.45	42.59	341	412	407	398	390	435
↓	5.0	17.58	42.98	341	412	407	399	391	436
16.88	5.5	17.73	43.41	342	413	408	400	391	437
15.66	6.0	16.74	40.55	339	408	403	395	386	431
	6.5	16.92	41.06	339	409	404	396	387	432
↓	7.0	17.12	41.62	340	410	405	397	388	433
	7.5	17.32	42.21	341	411	406	398	390	435
15.66	8.0	17.54	42.85	342	413	408	400	391	437
14.49	8.5	16.75	40.58	339	408	403	395	387	431
14.49	9.0	17.01	41.30	340	410	405	397	388	433
14.49	9.5	17.27	42.06	341	412	407	398	390	435
13.47	10.0	16.72	40.48	340	408	404	396	387	432
13.47	10.5	17.02	41.34	341	410	406	397	389	434
13.47	11.0	17.33	42.22	342	412	407	399	391	436
12.61	11.5	17.00	41.29	341	411	406	398	389	434
11.46	12.0	16.53	39.96	340	408	403	395	387	431
11.46	12.5	16.90	40.98	341	410	405	397	389	434
10.48	13.0	16.64	40.26	341	409	404	396	388	432
9.41	13.5	16.41	39.59	340	408	403	395	387	431
9.41	14.0	16.82	40.76	342	410	406	398	389	434
8.17	14.5	16.60	40.14	31	409	405	397	388	433

Table #1.3 Experimental Results - Time of Flight
LEFT SIDE PROBE

θ_{xy}	θ_{xz}	θ_{xyz} Incidence	θ_{xyz} Refracted	Surface Time	Hole #1 Time	Hole #2 Time	Hole #3 Time	Hole #4 Time	Corner Time
17.13	0	17.13	41.66	336	412	406	396	388	432
↓	0.5	17.14	41.68	336	412	407	397	389	433
	1.0	17.16	41.74	335	412	407	396	389	432
	1.5	17.19	41.84	336	412	406	396	389	433
	2.0	17.24	41.98	335	411	407	396	388	432
	2.5	17.31	42.17	336	411	406	397	388	432
	3.0	17.38	42.39	335	413	407	397	389	432
	3.5	17.47	42.65	336	413	408	399	390	433
	4.0	17.58	42.96	337	414	408	399	389	434
	4.5	17.69	43.30	337	415	409	399	390	434
	5.0	17.82	43.69	337	416	410	400	390	434
17.13	5.5	17.97	44.11	340	415	410	401	391	435
15.92	6.0	16.99	41.24	336	412	406	396	389	433
↓	6.5	17.16	41.75	336	413	408	397	389	432
	7.0	17.35	42.31	338	414	408	398	390	433
↓	7.5	17.56	42.90	338	415	408	399	391	433
15.92	8.0	17.77	43.53	339	415	410	401	391	435
14.79	8.5	17.01	41.31	336	412	407	398	389	432
14.79	9.0	17.26	42.03	337	414	407	399	390	435
14.79	9.5	17.52	42.79	338	415	409	400	392	434
13.74	10.0	16.94	41.10	335	413	406	397	388	433
13.74	10.5	17.23	41.95	336	414	406	397	388	433
13.74	11.0	17.53	42.83	336	414	407	397	390	433
12.63	11.5	17.02	39.49	335	413	407	397	390	432
11.52	12.0	16.58	40.07	335	413	406	397	388	433
11.52	12.5	16.94	41.10	334	414	407	399	388	432
10.48	13.0	16.64	40.26	336	412	405	399	388	434
9.33	13.6	16.36	39.47	332	411	405	397	386	431
9.33	14.0	16.77	40.63	336	413	406	398	387	433
8.34	14.5	16.68	40.38	336	412	405	398	389	433

Table #1.4 Experimental Results - Time of Flight
RIGHT SIDE PROBE

ϕ_{xy}	ϕ_{xs}	ϕ_{xys} Incident	ϕ_{xys} Calculated	Surface Time	Hole #1 Time	Hole #2 Time	Hole #3 Time	Hole #4 Time	Corner Time
16.88	0	16.88	40.94	336	410	403	394	387	433
↓	0.5	16.89	40.96	337	410	404	394	387	433
	1.0	16.91	41.02	338	411	404	394	386	433
	1.5	16.94	41.12	338	410	404	394	386	433
	2.0	16.99	41.27	337	411	404	895	387	433
	2.5	17.06	41.45	337	411	405	395	387	434
	3.0	17.14	41.68	337	411	405	395	387	434
	3.5	17.23	41.94	338	412	405	396	388	434
	4.0	17.33	42.25	338	412	406	897	388	435
	4.5	17.45	42.59	338	413	407	398	389	435
	5.0	17.58	42.98	339	413	408	399	390	436
16.88	5.5	17.73	43.41	340	414	409	400	391	437
15.66	6.0	16.74	40.55	336	410	404	396	386	434
↓	6.5	16.92	41.06	336	411	405	397	387	434
	7.0	17.12	41.62	338	412	406	398	387	435
	7.5	17.32	42.21	340	412	408	400	388	436
15.66	8.0	17.54	42.85	340	414	410	401	391	437
14.49	8.5	16.75	40.58	338	412	405	397	387	435
14.49	9.0	17.01	41.30	336	412	408	398	389	436
14.49	9.5	17.27	42.06	338	415	409	399	390	438
13.47	10.0	16.72	40.48	338	413	406	396	387	435
13.47	10.5	17.02	41.34	340	415	407	397	387	437
13.47	11.0	17.33	42.22	340	416	409	399	390	439
12.61	11.5	12.00	41.29	340	413	408	398	389	437
11.46	12.0	16.53	39.96	338	410	405	396	386	434
11.46	12.5	16.90	40.98	340	413	407	398	388	437
10.48	13.0	16.64	40.26	338	411	405	397	387	435
9.41	13.5	16.41	39.59	336	410	404	395	386	434
9.41	14.0	16.82	40.76	339	413	408	399	389	438
8.17	14.5	16.60	40.14	338	412	407	397	390	437

Table #1.5 Calculated Results – Location of Probe
LEFT SIDE PROBE

θx,y	θx,z	Hole #1 y	Hole #1 z	Hole #2 y	Hole #2 z	Hole #3 y	Hole #3 z	Hole #4 y	Hole #4 z
0	0	0	0	0	0	0	0	0	0
17.13	0	37.6	0	36.5	0	34.7	0	33.3	0
	0.5	37.6	1.2	36.5	1.2	34.7	1.1	33.3	1.1
	1.0	37.7	2.4	36.5	2.3	34.7	2.2	33.3	2.1
	1.5	37.7	3.6	36.5	3.5	34.7	3.3	33.3	3.2
	2.0	37.7	4.8	36.6	4.6	34.8	4.4	33.4	4.3
	2.5	37.8	6.0	36.6	5.8	34.8	5.6	33.4	5.4
	3.0	37.9	7.2	36.7	7.0	34.9	6.7	33.5	6.4
	3.5	38.0	8.4	36.9	8.2	35.0	7.8	33.5	7.5
	4.0	38.1	9.6	36.9	9.4	35.1	8.9	33.6	8.6
	4.5	38.2	10.9	37.0	10.6	35.2	10.1	33.7	9.7
	5.0	38.3	12.1	37.1	11.8	35.3	11.2	33.8	10.8
17.13	5.5	38.4	13.4	37.2	13.0	35.4	12.4	33.9	11.9
15.92	6.0	34.9	14.3	33.9	13.9	32.2	13.3	30.9	12.8
	6.5	35.1	15.6	34.0	15.1	32.3	14.5	31.0	14.0
	7.0	35.2	16.8	34.2	16.4	32.5	15.7	31.1	15.1
	7.5	35.4	18.1	34.3	17.6	32.6	16.8	31.3	16.2
15.92	8.0	35.6	19.4	34.5	18.9	32.8	18.0	31.4	17.4
14.79	8.5	32.5	20.4	31.5	19.8	30.0	19.0	28.8	18.3
14.79	9.0	32.7	21.7	31.7	21.1	30.2	20.2	28.9	19.4
14.79	9.5	32.9	23.0	31.9	22.4	30.3	21.4	29.1	20.6
13.74	10.0	30.2	24.5	29.3	23.4	27.9	22.3	26.7	21.5
13.74	10.5	30.4	25.4	29.5	24.7	28.0	23.6	26.9	22.7
13.74	11.0	30.7	26.7	29.7	26.0	28.2	24.9	27.1	23.9
12.63	11.5	27.9	27.7	27.0	27.0	25.7	25.8	24.6	24.9
11.52	12.0	26.2	28.8	24.4	28.0	23.3	26.8	22.3	25.8
11.52	12.5	25.4	30.2	24.6	29.4	23.4	28.1	22.5	27.1
10.98	13.0	23.0	31.3	22.3	30.4	21.2	29.1	20.3	28.1
9.33	13.5	20.4	32.4	19.7	31.5	18.8	30.2	18.0	29.1
9.33	14.0	20.5	33.9	19.9	32.9	19.0	31.5	18.2	30.4
8.34	14.5	18.3	35.1	17.8	34.1	16.9	32.7	16.2	31.5

Table #1.6 Calculated Results - Location of Probe
RIGHT SIDE PROBE

Ox y	Ox z	Hole #1 y	Hole #1 z	Hole #2 y	Hole #2 z	Hole #3 y	Hole #3 z	Hole #4 y	Hole # z
0	0	0	0	0	0	0	0	0	0
16.88	0	36.9	0	35.8	0	34.0	0	32.6	0
↓	0.5	36.9	1.2	35.8	1.2	34.0	1.1	32.6	1.1
↓	1.0	36.9	2.4	35.8	2.3	34.0	2.2	32.7	2.1
↓	1.5	36.9	3.6	35.8	3.5	34.1	3.3	32.7	3.2
↓	2.0	37.0	4.8	35.8	4.6	34.1	4.4	32.7	4.3
↓	2.5	37.0	6.0	35.9	5.8	34.2	5.5	32.8	5.3
↓	3.0	37.1	7.2	36.0	7.0	34.2	6.7	32.8	6.4
↓	3.5	37.2	8.4	36.0	8.1	34.3	7.8	32.9	7.5
↓	4.0	37.3	9.6	36.1	9.3	34.4	8.9	32.9	8.6
↓	4.5	37.4	10.8	36.2	10.5	34.5	10.1	33.0	9.7
↓	5.0	37.5	12.0	36.4	11.7	34.6	11.2	33.1	10.8
16.88	5.5	37.7	13.3	36.5	12.9	34.7	12.4	33.2	11.9
15.66	6.0	34.2	14.3	33.1	13.9	31.5	13.3	30.3	12.8
↓	6.5	34.3	15.5	33.3	15.1	31.7	14.4	30.4	13.9
↓	7.0	34.5	16.8	33.4	16.3	31.8	15.6	30.5	15.0
↓	7.5	34.7	18.0	33.6	17.5	31.9	16.8	30.6	16.2
15.66	8.0	34.8	19.3	33.8	18.8	32.1	18.0	30.8	17.3
14.49	8.5	31.7	20.3	30.7	19.7	29.2	18.9	28.0	18.2
14.49	9.0	31.9	21.6	30.9	21.0	29.4	20.1	28.2	19.4
14.49	9.5	32.1	22.9	31.1	22.3	29.6	21.3	28.4	20.5
13.47	10.0	29.5	23.9	28.6	23.3	27.2	22.3	26.1	21.5
13.47	10.5	29.7	25.3	28.8	24.6	27.4	23.5	26.3	22.7
13.47	11.0	29.9	26.6	29.0	25.9	27.6	24.8	26.4	23.9
12.61	11.5	27.8	27.7	27.0	27.0	25.6	25.8	24.6	24.9
11.46	12.0	25.0	28.8	24.3	28.0	23.1	26.8	22.2	25.8
11.46	12.5	25.2	30.2	24.5	29.3	23.3	28.1	22.3	27.1
10.48	13.0	23.0	31.3	22.3	30.4	21.2	29.1	20.3	28.1
9.41	13.5	20.5	32.4	19.9	31.5	19.0	30.2	18.2	29.1
9.41	14.0	20.7	33.9	20.1	33.0	19.1	31.5	18.4	30.4
8.11	14.5	17.9	35.0	17.4	34.1	16.6	32.6	15.9	31.4

Table #1.7 Experimental Results - Location of Probe
LEFT SIDE PROBE

θ_{xy}	θ_{xz}	Hole #1 y	Hole #1 z	Hole #2 y	Hole #2 z	Hole #3 y	Hole #3 z	Hole #4 y	Hole #4 z
0	0	0	0	0	0	0	0	0	0
17.13	0	38.5	0	37.5	0	35.5	0	33.5	0
↓	0.5	↓	1.0	↓	1.0	↓	1.0	↓	1.0
↓	1.0	↓	2.5	↓	2.0	↓	2.0	↓	2.0
↓	1.5	↓	3.0	↓	3.0	↓	3.0	↓	2.5
↓	2.0	↓	4.5	↓	4.5	↓	4.5	↓	4.0
↓	2.5	↓	6.0	↓	6.0	↓	6.0	↓	5.5
↓	3.0	↓	7.5	↓	7.5	↓	7.0	↓	7.0
↓	3.5	↓	9.0	↓	9.0	↓	8.5	↓	8.0
↓	4.0	↓	10.0	↓	10.0	↓	9.5	↓	9.0
↓	4.5	↓	11	↓	10.5	↓	10.0	↓	9.5
↓	5.0	↓	12.5	↓	12.0	↓	11.5	↓	11.0
17.13	5.5	38.5	14.0	37.5	13.5	35.5	13.0	33.5	12.0
15.92	6.0	36.0	15.0	34.5	15.0	33.0	14.0	31.5	13.5
↓	6.5	↓	16.5	↓	16.0	↓	15.5	↓	14.5
↓	7.0	↓	18.0	↓	17.5	↓	16.5	↓	15.5
↓	7.5	↓	19.0	↓	18.0	↓	17.0	↓	16.0
15.92	8.0	36.0	20.0	34.5	19.5	33.0	18.5	31.5	18.0
14.79	8.5	33.5	22.0	32.5	21.0	31.0	20.0	29.5	19.5
14.79	9.0	33.5	23.0	32.5	22.5	31.0	21.0	29.5	20.5
14.79	9.5	33.5	24.5	32.5	23.5	31.0	22.5	29.5	21.5
13.74	10.0	31.0	26.0	30.0	24.5	29.0	24.0	27.0	23.0
13.74	10.5	31.0	27.0	30.0	26.0	29.0	25.0	27.0	23.5
13.74	11.0	31.0	28.0	30.0	27.0	29.0	26.0	27.0	25.0
12.63	11.5	28.5	29.0	27.5	28.0	27.0	27.0	25.5	26.0
11.52	12.0	28.5	30.0	25.0	29.5	24.5	28.0	22.5	27.0
11.52	12.5	26.0	32.0	25.0	31.0	24.5	30.0	22.5	28.0
10.48	13.0	26.0	33.5	23.0	32.5	22.5	31.0	20.5	29.0
9.33	13.5	23.5	34.0	20.0	32.5	20.0	31.5	18.0	29.0
9.33	14.0	21.0	35.5	20.0	32.5	20.0	33.5	18.0	31.0
8.34	14.5	19.0	37.5	17.5	36.0	18.0	34.5	17.0	33.0

Table #18 Experimental Results - Location of Probe
RIGHT SIDE - PROBE

θ_{xy}	θ_{xz}	Hole #1 y	Hole #1 z	Hole #2 y	Hole #2 z	Hole #3 y	Hole #3 z	Hole #4 y	Hole #4 z
0	0	0	0	0	0	0	0	0	0
16.88	0	37.5	0	35.5	0	33.5	0	32.5	0
↓	0.5	37.5	1.5	↓	2.0	↓	1.0	32.5	1.5
↓	1.0	37.5	2.5	↓	3.0	↓	2.0	32.0	2.5
↓	1.5	37.5	3.5	↓	4.0	↓	3.5	31.5	3.5
↓	2.0	37.0	5.0	↓	5.5	↓	5.0	32.0	5.0
↓	2.5	↓	6.5	↓	7.0	↓	6.0	↓	6.0
↓	3.0	↓	7.5	↓	8.0	33.5	7.0	↓	7.0
↓	3.5	↓	9.0	↓	9.0	34.0	8.5	↓	8.0
↓	4.0	37.0	10.0	↓	10.0	34.0	9.5	↓	9.5
↓	4.5	37.5	11.0	↓	11.5	34.0	10.5	32.0	10.0
↓	5.0	32.5	13.0	↓	13.0	34.5	12.0	32.5	11.5
16.88	5.5	37.5	14.0	35.5	14.0	34.5	13.0	32.5	12.5
15.66	6.0	34.5	15.0	32.5	15.0	32.0	14.5	29.5	13.5
↓	6.5	35.0	16.5	33.0	16.0	32.0	15.5	29.5	14.5
↓	7.0	35.0	17.5	33.0	17.5	32.0	17.0	29.5	16.0
↓	7.5	35.5	18.5	34.0	19.0	32.5	18.0	29.5	16.5
15.66	8.0	35.5	20.0	34.0	20.5	32.5	19.5	30.5	18.5
14.49	8.5	32.5	21.5	31.0	21.5	29.5	20.5	27.5	19.5
14.49	9.0	33.0	22.5	31.5	22.5	29.5	21.5	27.5	20.5
14.49	9.5	33.5	24.0	31.5	24.0	29.5	22.5	28.0	22.0
13.47	10.0	31.0	25.0	29.5	25.5	27.0	23.5	25.0	22.5
13.47	10.5	34.0	26.0	29.0	26.5	27.0	24.5	25.0	23.5
13.47	11.0	34.0	28.0	29.0	28.0	27.0	26.5	25.5	25.0
12.61	11.5	28.0	29.0	26.5	29.0	25.5	27.0	23.5	26.0
11.46	12.0	25.5	30.0	24.0	30.0	23.0	28.5	21.5	27.0
11.46	12.5	26.0	31.5	24.0	31.5	23.0	29.5	21.5	28.0
10.48	13.0	23.5	32.0	21.5	33.5	21.0	31.0	19.5	29.5
9.41	13.5	21.0	34.0	19.0	34.0	19.0	31.5	17.5	30.0
9.41	14.0	21.0	35.5	19.5	35.5	19.5	34.0	18.0	32.0
8.17	14.5	18.5	37.0	17.0	36.5	16.5	34.0	16.0	33.5

First Test Results - EDM Crack

Left Side Probe
$y = 95mm = 0$ $z_L = 118mm = 0$

Right Side Probe
$y = 95mm = 0$ $z_R = 183mm = 0$

θ_{xy}	θ_{xz}	y (mm) ↑	*Dist (mm)	Time
17.13	0	40	0	389
	0.5	40	1	384
	1.0	40	4.5	389
	1.0	40	5.5	389
	1.5	40	5.0	389
	2.0	40.5	9.0	391
	2.5	40.5	11.5	391
	3.0	41.	15.0	392
	3.5	41.	17.0	392
	4.0	41	18.5	393
	4.5	41.5	19.5	394
	5.0	41.5	22.0	396
17.13	5.5	40	25.0	399
15.92	6.0	40	29.5	396
	6.5	40	30.5	397
	7.0	40	34.0	400
	7.5	41	34.0	399
15.92	8.0	39	37.0	404
14.79	8.5	39	39.5	403
14.79	9.0	39	41.5	404
14.79	9.5	39.5	44.0	407
13.74	10.0	38.	46.5	406
13.74	10.5	38	47.0	407
13.74	11.0	38	49.0	410
11.52	12.0	34	56.0.	411
11.52	12.5	32	58.0	414
10.48	13.0	32.5	60.5	416
9.33	14.0	29.5	64.0	418
8.34	14.5	27.0	67.0	420

θ_{xy}	θ_{xz}	y (mm) ↑	*Dist (mm)	Time
16.88	0	40.5	0	385
	0.5	40.5	4.5	385
	1.0	41.0	7.0	386
	1.0	41.0	8.0	386
	1.5	41.0	11.0	387
	2.5	41.0	13.0	389
	3.0	41.5	15.0	390
	3.0	42.0	16.5	391
	3.5	42.0	19.0	394
	4.0	42.5	23.0	395
	4.5	42.5	25.0	398
	5.0	43.0	27.0	400
16.88	5.5	43.5	29.0	403
15.66	6.0	41.0	31.5	400
	6.5	44.0	33.0	401
	7.0	42.0	35.5	404
	7.5	42.0	38.0	408
15.66	8.0	42.5	40.0	410
14.49	8.5	40.0	42.5	408
14.49	9.0	40.0	45.0	411
14.49	9.5	40.5	48.0	415
13.47	10.0	38.0	50.5	416
13.47	10.5	39.0	53.0	418
13.47	11.0	39.0	55.0	422
11.46	12.0	36.0	59.0	423
11.46	12.5	36.0	61.0	427
10.48	13.0	34.5	64.0	429
9.41	14.0	33.0	71.0	438
8.47	14.5	30.5	75.0	443

* Dist = dist from centre of EDM crack to probe. in the z direction.

Table 2.1

Calculated EOM Data

Left Hand Side

θ_{xy}	θ_{xz}	Time	(ts-depth) (mm)	$\frac{z}{(mm)}$	Location (mm)
17.13	00	389	12.0	0.0	0
	05	389	12.0	1.0	0
	1.0	389	11.9	2.0	2.5
	1.5	389	11.9	3.0	2.5
	2.0	391	12.3	4.0	1.0
	2.5	391	12.2	5.0	4.0
	3.0	392	12.4	6.0	5.5
	3.5	392	12.3	7.0	8.0
	4.0	393	12.4	8.0	9.0
	4.5	391	12.4	9.0	9.5
	5.0	396	12.7	10.1	9.4
17.13	5.5	399	13.3	11.2	10.6
15.92	6.0	396	13.8	12.4	12.6
	6.5	397	13.8	13.4	17.1
	7.0	400	14.2	14.6	19.4
	7.5	399	13.7	15.5	18.5
15.92	8.0	404	14.6	16.9	20.1
14.79	8.5	403	15.3	18.2	21.3
14.79	9.0	404	15.2	18.3	23.2
14.79	9.5	407	15.5	20.5	23.5
13.74	10.0	406	16.0	21.9	24.6
13.74	10.5	407	15.9	23.0	24.0
13.74	11.0	410	16.1	24.3	24.7
11.57	12.0	411	17.6	27.5	28.5
11.52	12.5	414	17.8	28.9	29.1
10.48	13.0	416	18.7	30.7	29.8
9.33	14.0	418	18.9	33.5	30.5
8.34	14.5	420	19.5	35.3	31.7

Table 2.2

CALCULATED EOM DATA

RIGHT HAND SIDE

$\theta_{x'y}$	θ_{xz}	TIME	(t_s - OFFSET) (mm)	Z (mm)	LOCATION (mm)
16.88	0.0	385	11.3	0	0
	0.5	385	11.3	1.0	3.5
	1.0	386	11.5	2.0	5.0
	1.5	387	11.7	2.9	5.1
	2.0	389	12.1	4.0	7.0
	2.5	390	12.3	5.0	10.0
	3.0	391	12.4	6.0	10.5
	3.5	394	13.0	7.1	11.9
	4.0	396	13.2	8.1	14.9
	4.5	398	13.7	9.2	15.8
	5.0	400	14.0	10.3	16.7
16.88	5.5	403	14.5	11.5	17.5
15.66	6.0	400	15.1	12.7	18.8
	6.5	401	15.0	13.7	19.3
	7.0	404	15.5	15.0	20.5
	7.5	408	16.2	16.3	21.7
15.66	8.0	410	16.3	17.4	22.6
14.49	8.5	408	17.0	18.8	23.7
14.49	9.0	411	17.3	20.1	24.9
14.49	9.5	415	17.9	21.5	25.5
13.47	10.0	416	18.8	23.1	27.4
13.47	10.5	418	18.9	24.3	28.7
13.47	11.0	422	19.4	25.8	29.2
11.46	12.0	423	20.7	29.1	29.9
11.46	12.5	427	21.1	30.7	30.3
10.98	13.0	429	22.0	32.6	31.4
9.41	14.0	438	23.8	36.6	34.4
8.17	14.5	443	25.4	39.2	35.8

Table 2.3

Second Test Results - EDM Crack

Left Side Probe
$y = 95mm = 0$ $z = 118mm = 0$

$\theta_{x'y}$	θ_{xz}	Y ↑ (mm)	*Dist (mm)	Time
17.13	0	41.0	0	392
	0.5	41.0	2.0	391
	1.0	41.0	5.5	392
	1.5	41.5	7.0	392
	2.0	41.5	11.0	393
	2.5	41.0	13.5	393
	3.0	41.5	15.0	393
	3.5	41.5	18.0	394
	4.0	41.5	19.5	395
	4.5	41.5	20.0	396
	5.0	42.0	24.0	399
17.13	5.5	42.5	26.5	401
15.92	6.0	40.5	29.0	398
	6.5	40.5	32.0	400
	7.0	41.0	34.5	403
	7.5	41.5	36.5	404
15.92	8.0	42.0	38.5	406
14.79	8.5	40.0	40.0	404
14.79	9.0	40.5	43.0	409
14.79	9.5	41.0	46.0	412
13.74	10.0	39.0	48.0	410
13.74	10.5	39.0	48.5	412
13.74	11.0	39.0	51.0	415
12.63	11.5	37.0	53.5	413
11.52	12.0	35.0	57.0	414
11.52	12.5	35.0	58.5	418
10.48	13.0	33.0	61.0	418
9.33	13.5	30.5	62.0	417
9.33	14.0	31.0	65.5	424
8.34	14.5	28.0	68.5	425
7.14	15.0	26.0	71.0	427
6.08	15.5	23.0	74.0	430
5.10	16.0	20.5	74.5	431
4.06	16.0	19.0	75.5	430
3.00	16.0	15.5	75.3	427

Right Side Probe
$y = 95mm = 0$ $z = 183mm = 0$

$\theta_{x'y}$	θ_{xz}	Y ↑ (mm)	*Dist (mm)	Time
16.88	0	41.0	0	387
	0.5	41.0	3.5	389
	1.0	41.5	6.0	390
	1.5	41.5	8.0	390
	2.0	41.5	12.0	391
	2.5	42.0	14.0	392
	3.0	42.0	16.0	394
	3.5	42.0	18.0	395
	4.0	43.0	22.0	399
	4.5	43.5	25.0	401
	5.0	43.5	27.5	404
16.88	5.5	44.0	29.0	405
15.66	6.0	41.5	31.0	401
	6.5	42.0	33.0	404
	7.0	42.0	35.0	407
	7.5	42.5	38.0	410
15.66	8.0	43.0	40.0	413
14.49	8.5	40.5	42.0	410
14.49	9.0	40.5	44.0	413
14.49	9.5	41.5	48.0	418
13.47	10.0	40.0	50.5	420
13.47	10.5	40.0	52.5	422
13.47	11.0	40.0	54.5	427
12.61	11.5	39.0	57.0	426
11.46	12.0	36.5	59.0	426
11.46	12.5	36.5	61.0	428
10.48	13.0	34.5	63.0	429
9.41	13.5	32.0	65.0	429
9.41	14.0	32.5	70.0	437
8.17	14.5	31.0	75.5	446
7.14	15.0	28.0	76.5	446
6.11	15.5	25.0	82.0	453
5.06	16.0	23.0	81.0	449

Table 3.1

EDM - SECOND TEST

LEFT-SIDE - CALCULATED

Δx'y	Δxz	Time	(ts-Depth) (mm)	Z (mm)	Location (mm)
12.13	0	392	12.7	0	0
	0.5	391	12.5	1.0	1.0
	1.0	392	12.7	2.0	3.5
	1.5	392	12.6	3.0	4.0
	2.0	393	12.8	4.0	7.0
	2.5	393	12.7	5.0	8.5
	3.0	393	12.6	6.0	9.0
	3.5	394	12.7	7.0	11.0
	4.0	395	12.8	8.0	11.5
	4.5	396	12.9	9.1	10.9
	5.0	399	13.5	10.2	13.8
12.13	5.5	401	13.7	11.3	15.2
15.92	6.0	398	14.2	12.5	16.5
	6.5	400	14.5	13.6	18.4
	7.0	403	15.0	14.8	19.7
	7.5	404	14.9	15.9	20.6
15.92	8.0	406	15.1	17.0	21.5
14.79	8.5	404	15.6	18.3	21.7
14.79	9.0	409	16.8	19.9	23.1
14.79	9.5	412	16.8	21.1	24.9
13.74	10.0	410	17.0	22.3	25.7
13.74	10.5	412	17.1	23.6	24.9
13.74	11.0	415	17.3	24.9	26.1
12.63	11.5	413	17.5	26.2	27.3
11.52	12.0	414	18.4	27.9	29.1
11.52	12.5	418	18.8	29.9	28.6
10.48	13.0	418	19.2	31.0	30.0
9.33	13.5	417	19.3	32.4	29.6
9.33	14.0	424	20.4	34.5	31.0
8.34	14.5	425	20.7	36.1	32.4
7.14	15.0	427	21.3	38.0	33.0
6.08	15.5	430	22.0	40.1	33.9
5.10	16.0	431	21.9	41.6	32.9
4.06	16.0	430	22.1	41.8	33.7
3.00	16.0	427	21.7	41.5	33.8

Table 3.2

EDM - SECOND TEST

RIGHT-SIDE - CALCULATED

Δx'y	Δxz	Time	(ts-depth) (mm)	z (mm)	Location (mm)
16.88	0	387	11.6	0	0
	0.5	389	12.3	1.0	2.5
	1.0	390	12.5	2.0	4.0
	1.5	390	12.4	3.0	5.0
	2.0	391	12.6	4.0	8.0
	2.5	392	12.8	5.0	9.0
	3.0	394	13.2	6.1	9.9
	3.5	395	13.3	7.1	10.9
	4.0	399	14.1	8.2	13.8
	4.5	401	14.4	9.3	16.7
	5.0	404	15.0	10.5	17.0
16.88	5.5	405	15.0	11.6	17.4
15.66	6.0	401	15.3	12.7	18.3
	6.5	404	15.8	13.9	19.1
	7.0	407	16.3	15.2	19.8
	7.5	410	16.7	16.4	21.6
15.66	8.0	413	17.1	17.7	22.3
14.49	8.5	410	17.4	18.9	23.1
14.49	9.0	413	17.8	20.3	23.7
14.49	9.5	418	18.6	21.8	26.2
13.47	10.0	420	19.8	23.5	27.0
13.47	10.5	422	19.9	24.8	27.7
13.47	11.0	427	20.6	26.4	28.1
12.61	11.5	426	20.8	27.8	29.2
11.46	12.0	426	21.5	29.5	29.5
11.46	12.5	428	21.4	30.8	30.2
10.48	13.0	429	22.0	32.6	30.4
9.41	13.5	429	22.3	34.2	30.8
9.41	14.0	437	23.6	36.5	33.2
8.17	14.5	446	26.1	39.7	35.8
7.14	15.0	446	26.1	41.4	35.1
6.11	15.5	453	27.7	44.3	37.7
5.06	16.0	449	26.4	45.1	35.9

Table 3.3

TABLE 4

GRAPHING SYMBOL LEGEND

GRAPH	θx'y	θxz	PROBE	PRINTED SYMBOL	PLOTTED SYMBOL
ULDAT1	16°	0°	RIGHT	0	○
	16°	2°	LEFT	2	△
	16°	3.5°	LEFT	+	+
	16°	5.5°	LEFT	X	x
	15°	7.5°	LEFT	5	◆
	16°	2.0°	RIGHT	6	♦
	16°	3.5°	RIGHT	7	X
	16°	5.5°	RIGHT	Z	z
	15°	7.5°	RIGHT	Y	y
ULDAT2	16°	0.0°	RIGHT	0	○
	16°	2.0°	RIGHT	2	△
	16°	4.0°	RIGHT	+	+
	16°	5.5°	RIGHT	X	x
	15°	7.5°	RIGHT	5	◇
	16°	0.0°	LEFT	6	♦
	16°	2.0°	LEFT	7	X
	16°	4.0°	LEFT	Z	z
	16°	5.5°	LEFT	Y	y
	15°	7.5°	LEFT	A	□
ULDAT3	16°	0.0°	RIGHT	0	○
	16°	2.0°	RIGHT	2	△
	16°	3.5°	RIGHT	+	+
	16°	0.0°	LEFT	X	x
	16°	3.5°	LEFT	5	◇
	16°	5.0°	LEFT	7	X
	15°	7.5°	LEFT	6	♦
ULDAT4	16°	0.0°	LEFT	0	○
	16°	2.0°	LEFT	2	△
	16°	3.5°	LEFT	+	+
	16°	5.5°	LEFT	X	x
	15°	7.5°	LEFT	5	◆
	16°	0.0	RIGHT	6	♦
	16°	2.0	RIGHT	7	X
	16°	3.5	RIGHT	Z	z
	16°	5.5	RIGHT	Y	y
ULDAT5	16°	0.0	RIGHT	0	○
	16°	2.0	RIGHT	2	△
	16°	0.0	LEFT	+	+

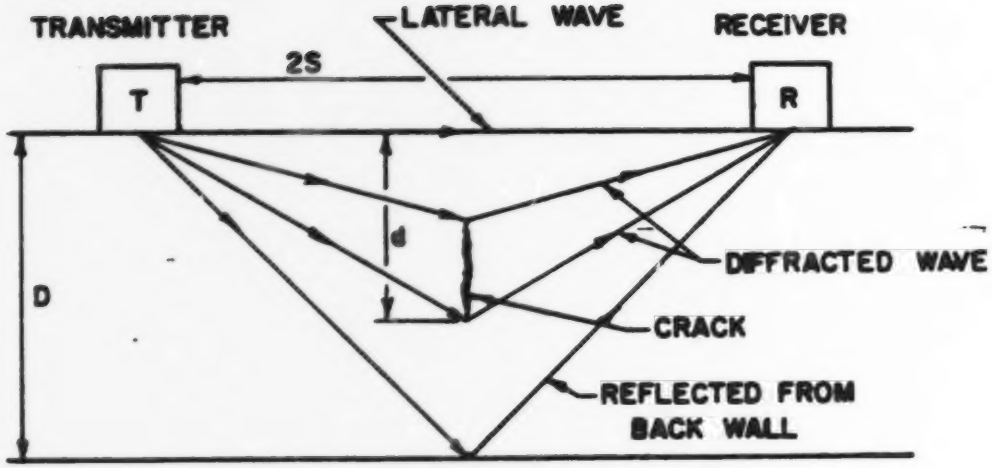

TWO PROBE METHOD FOR STUDYING CRACKS

FIG. NO. 1

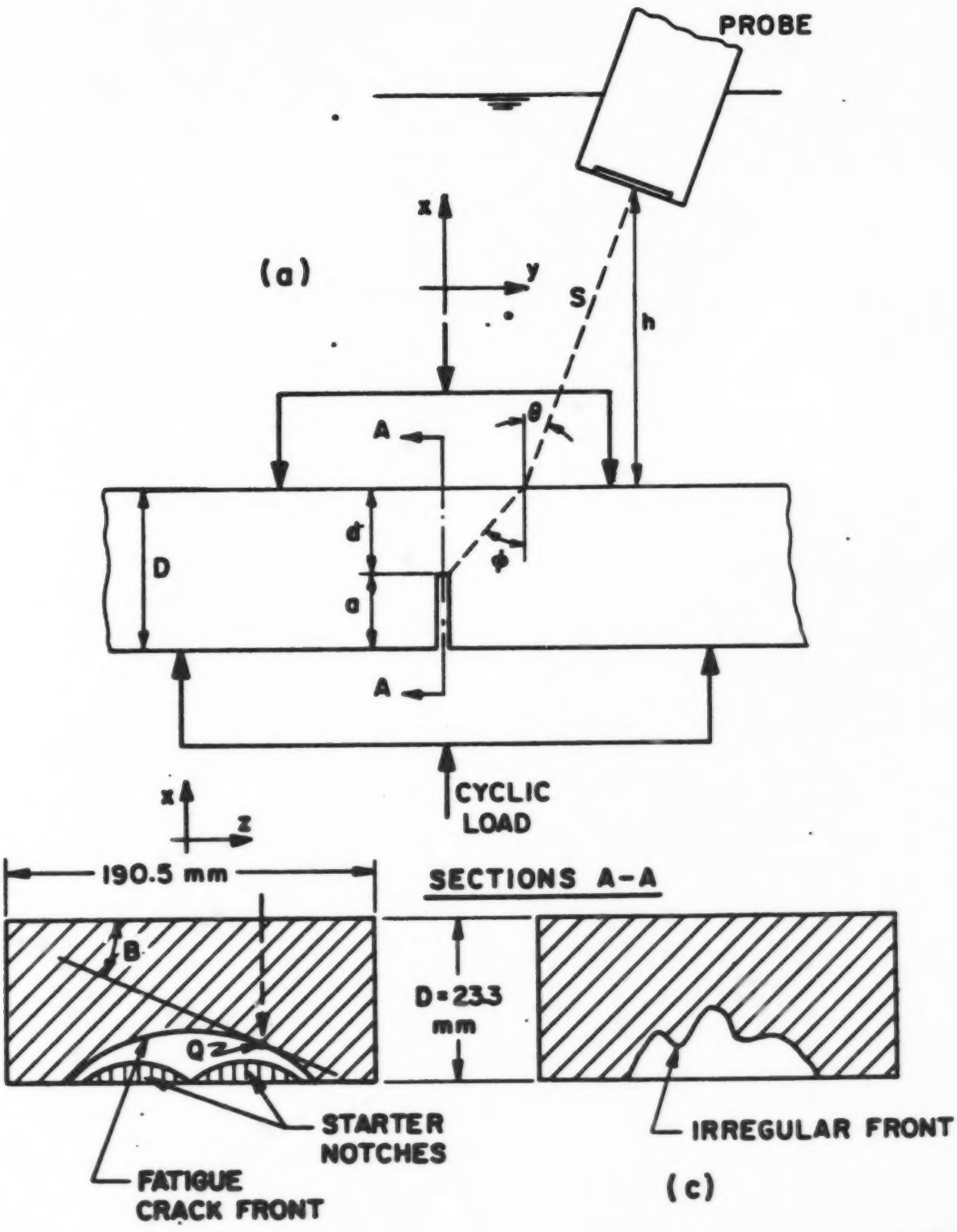
PROBE
(a)
x
y
S
h
θ
A
D
d
a
φ
A
CYCLIC
LOAD
x
z
190.5 mm
SECTIONS A-A
B
D=233
mm
Q2
STARTER
NOTCHES
FATIGUE
CRACK FRONT
IRREGULAR FRONT
(b)
(c)

FIG 2.

FIG. NO. 3

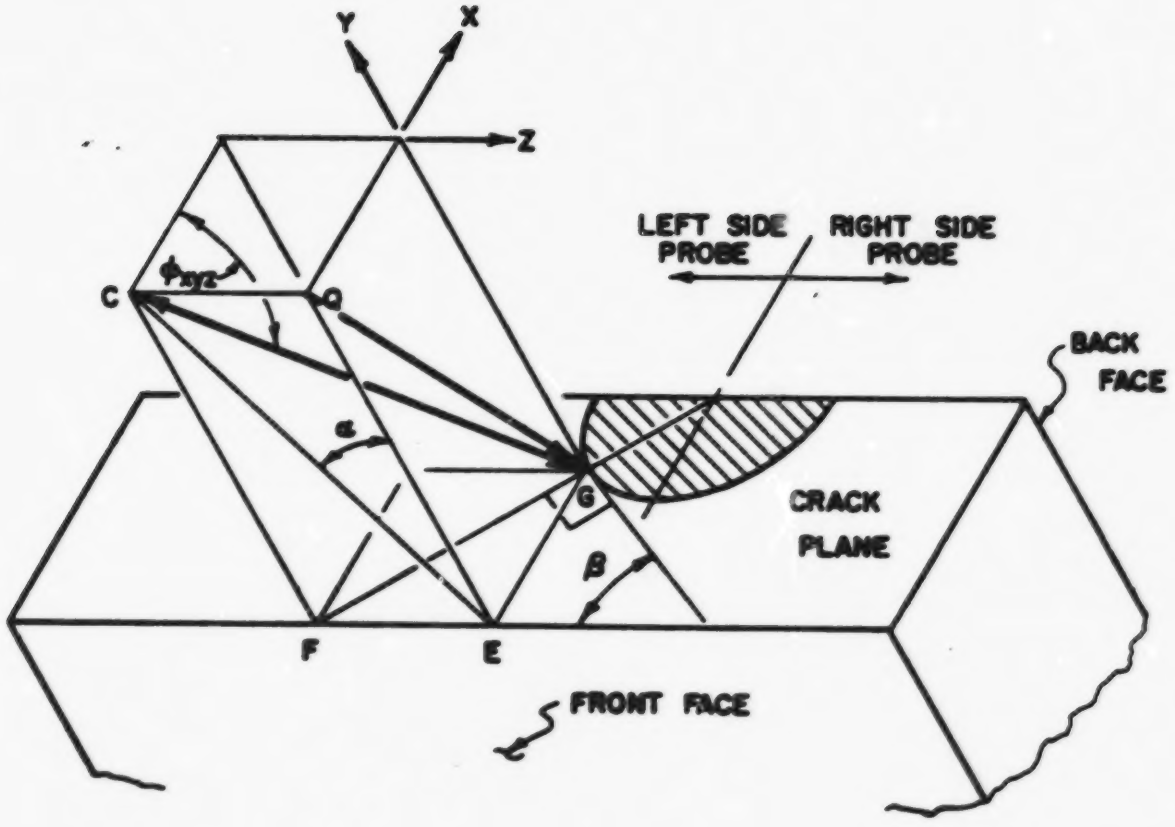
Y
X
Z
LEFT SIDE PROBE
RIGHT SIDE PROBE
ϕ_{xyz}
C
Q
BACK FACE
α
G
CRACK PLANE
β
F
E
FRONT FACE

FIG. NO. 4

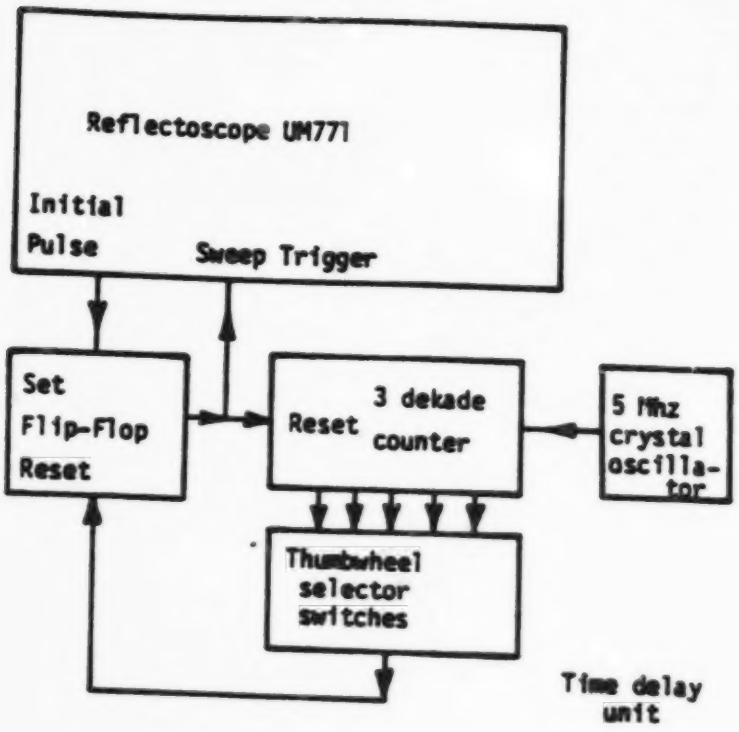

Fig. 5 Functional diagram of Time Delay Unit

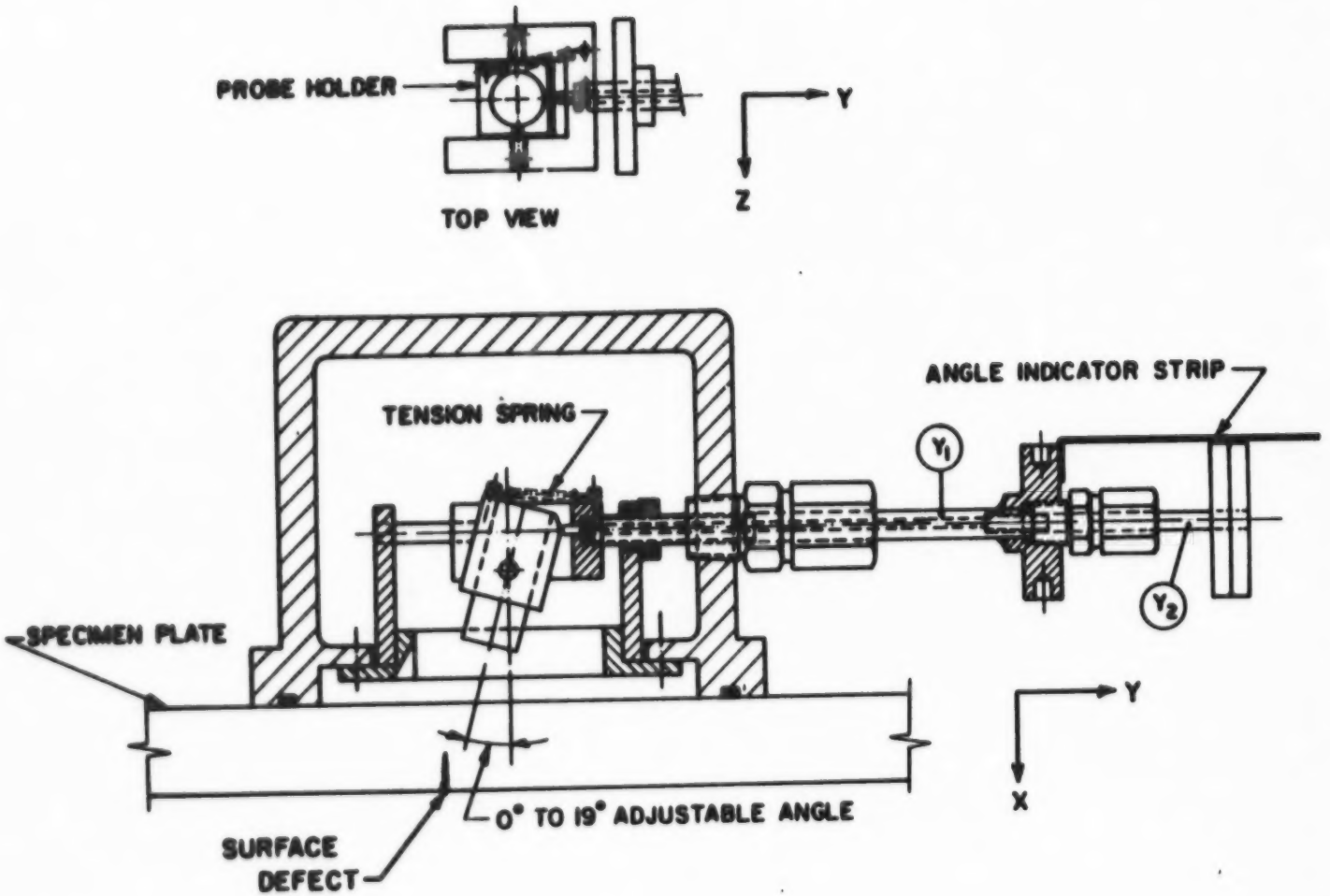
PROBE HOLDER
Y
Z
TOP VIEW
ANGLE INDICATOR STRIP
TENSION SPRING
Y_1
Y_2
SPECIMEN PLATE
Y
X
0° TO 19° ADJUSTABLE ANGLE
SURFACE
DEFECT

Fig. 6

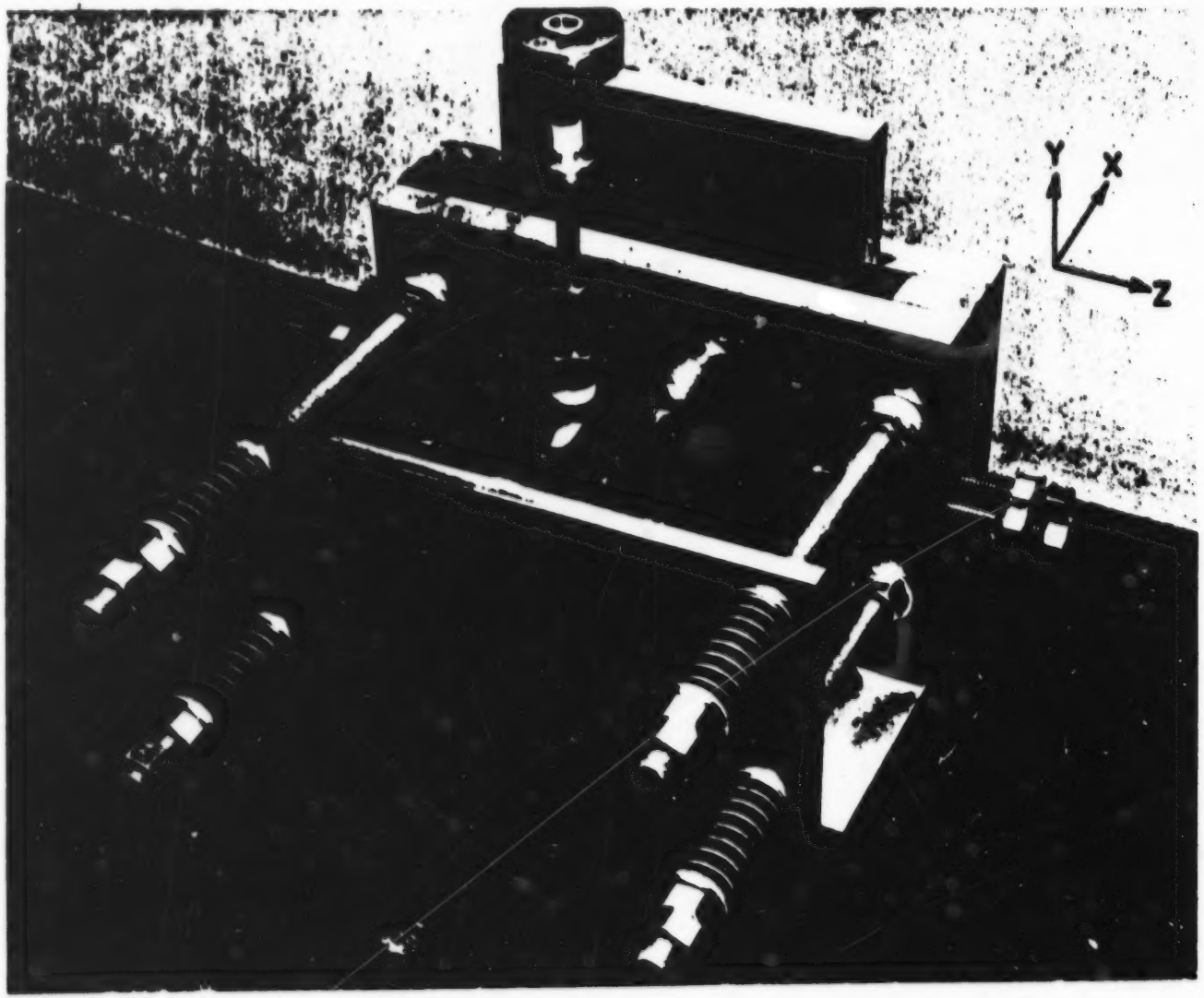

FIG. NO. 7

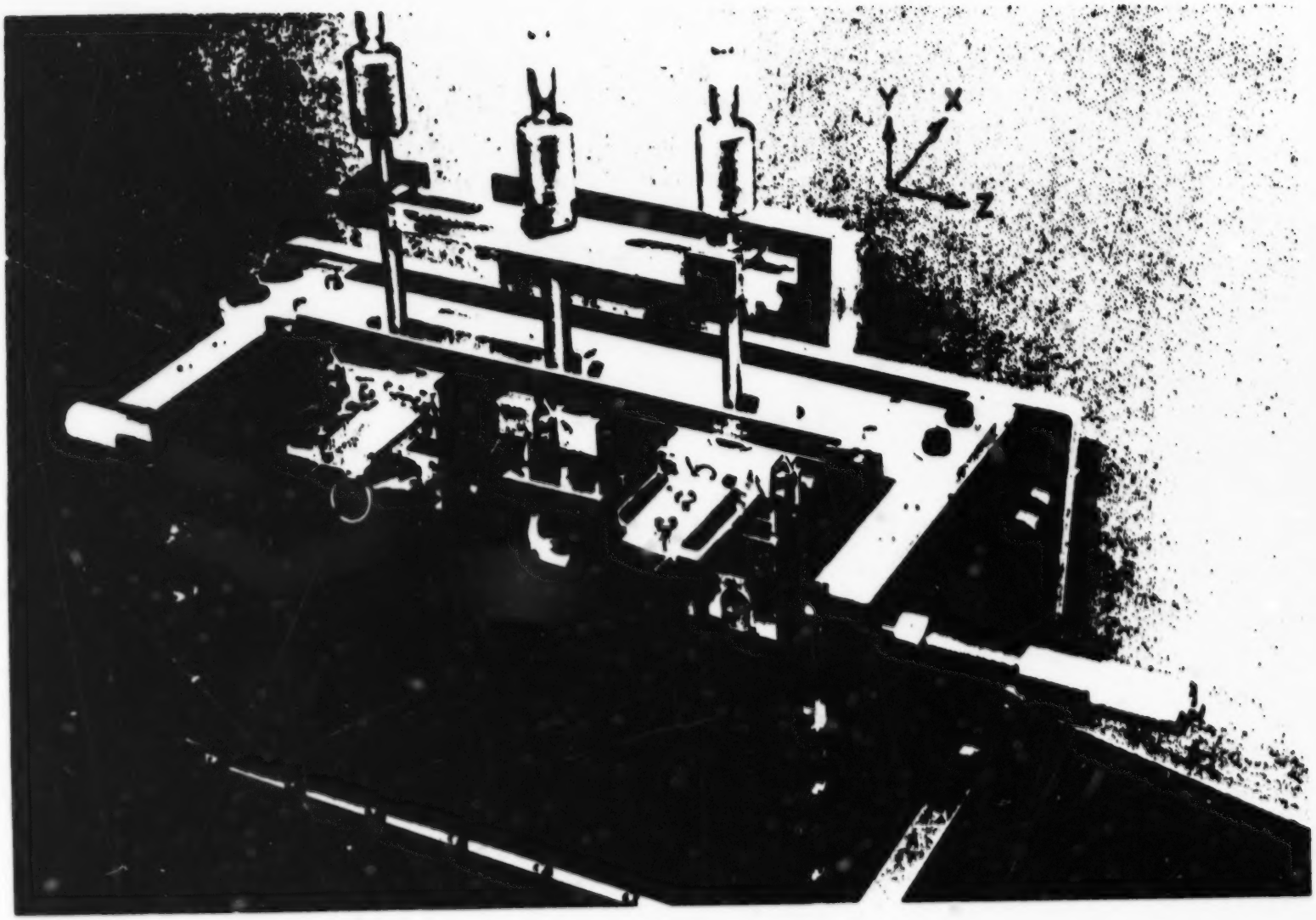

FIG. NO. 8

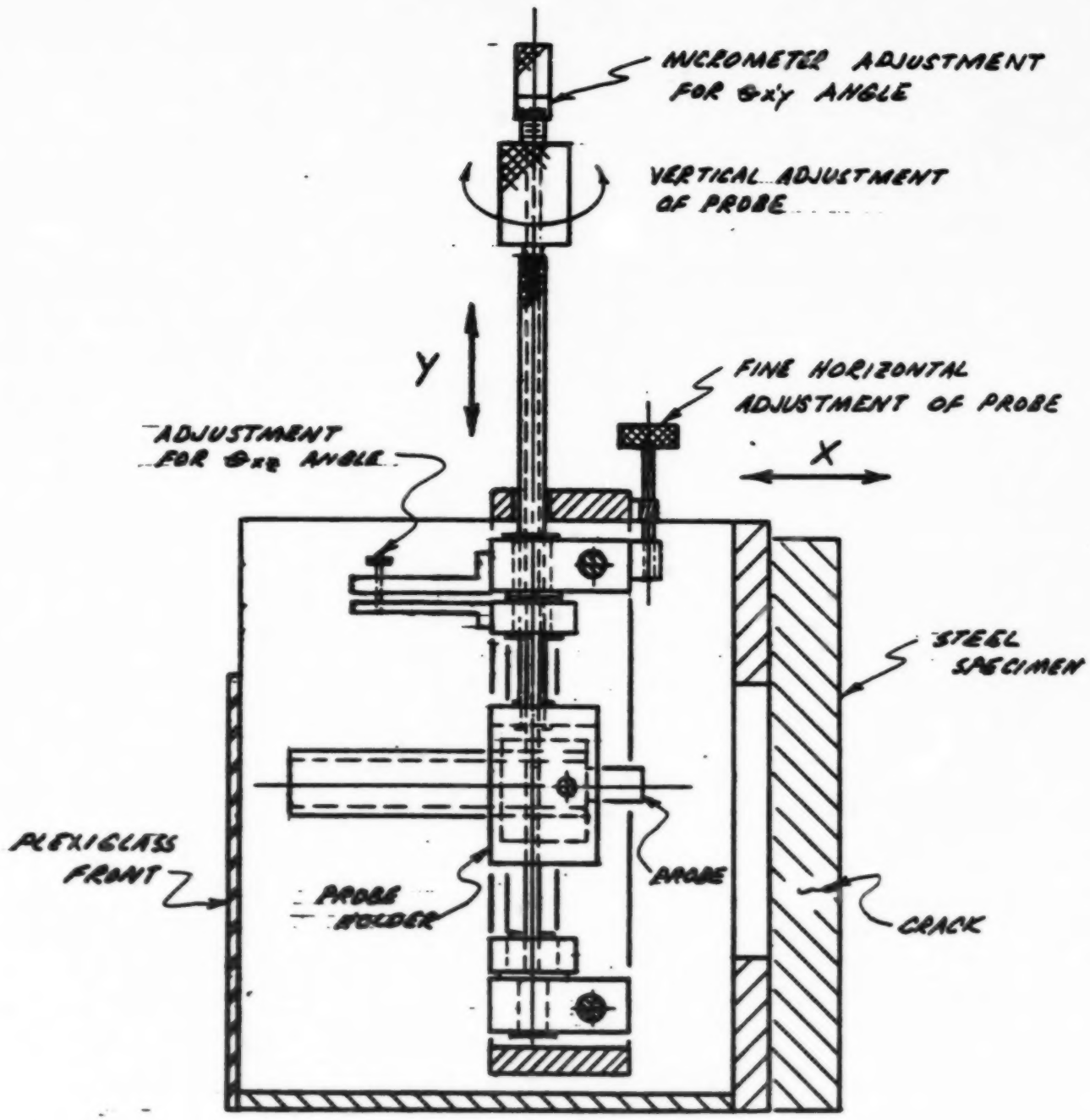

IMMERSION TANK

SECTION A-A

FIG. NO. 9

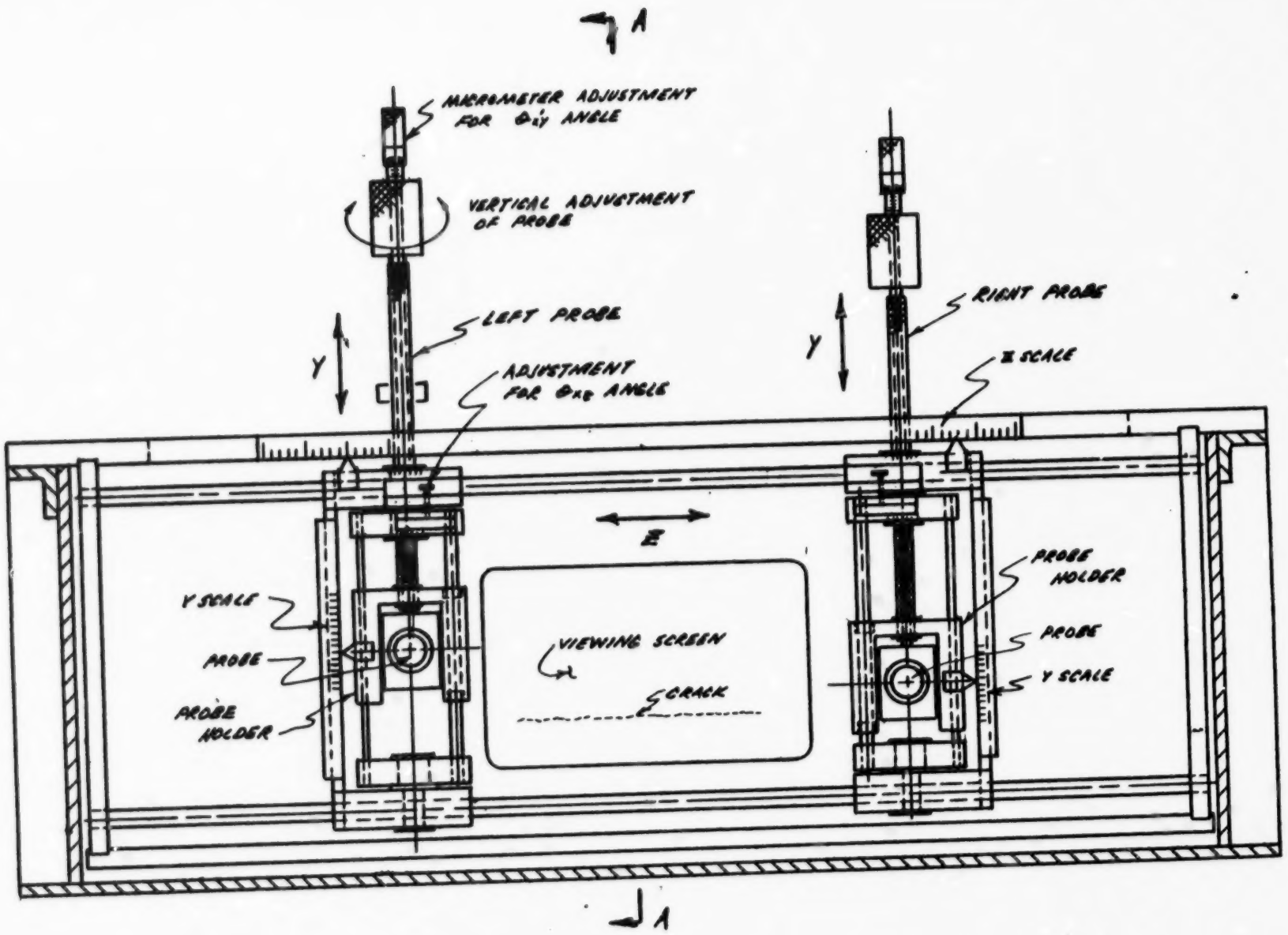

IMMERSION TANK

FRONT VIEW

FIG. NO. 10

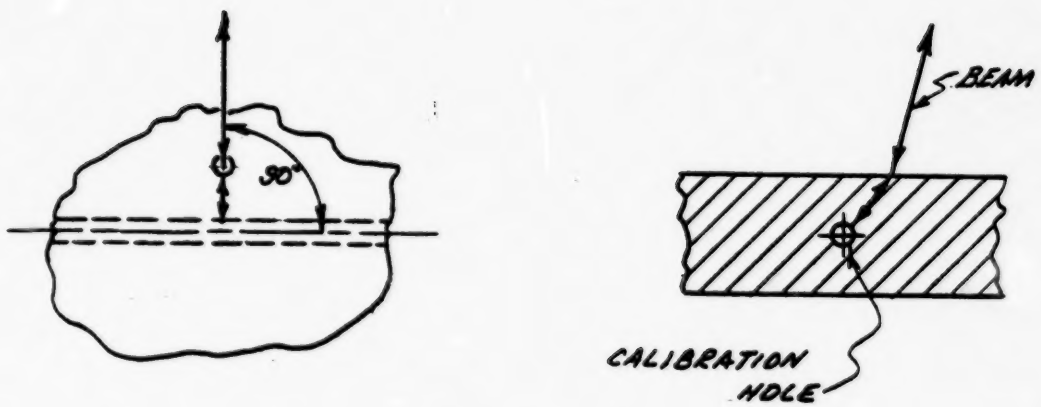

FIG. NO. 11a

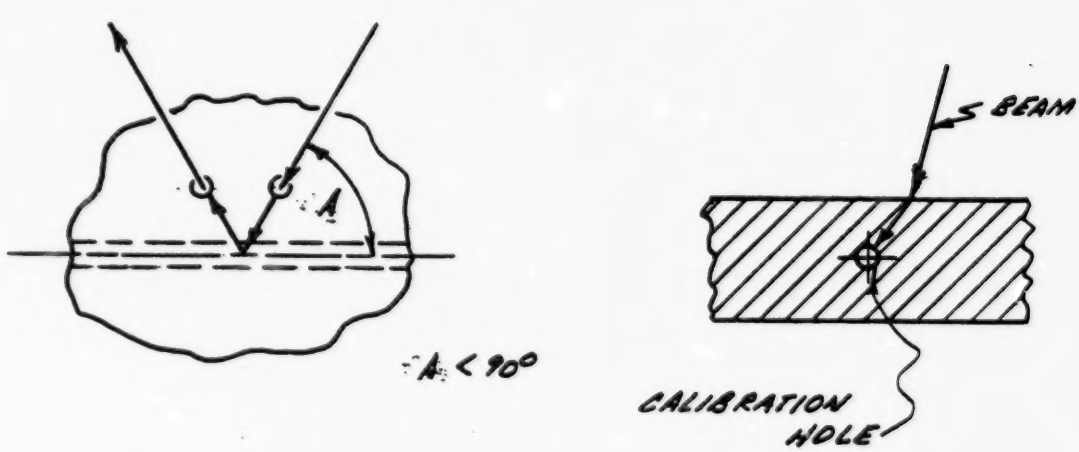

FIG. NO. 11b

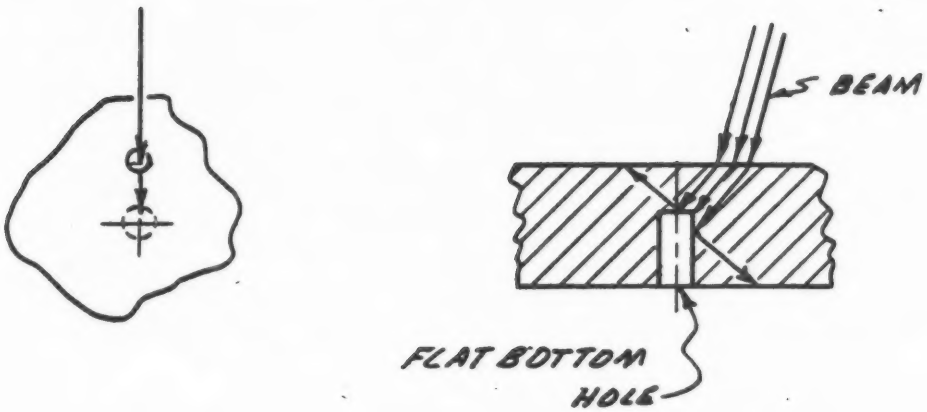

FIG. NO. 12a

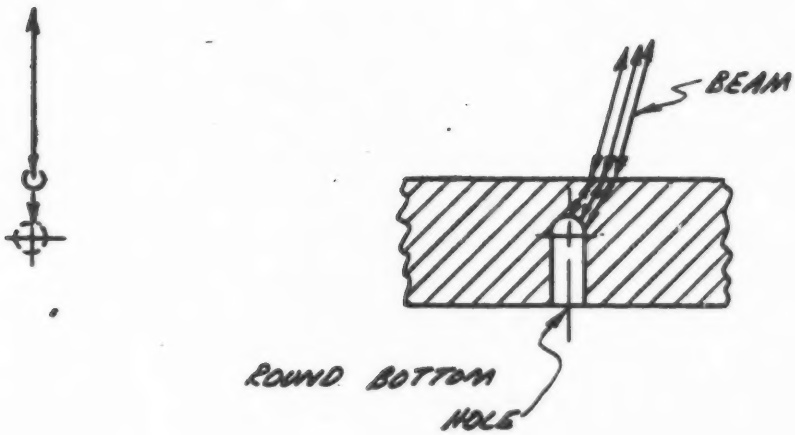

FIG. NO. 12b

ANGLE PROBE CALIBRATION PLATE
FIG. NO.13

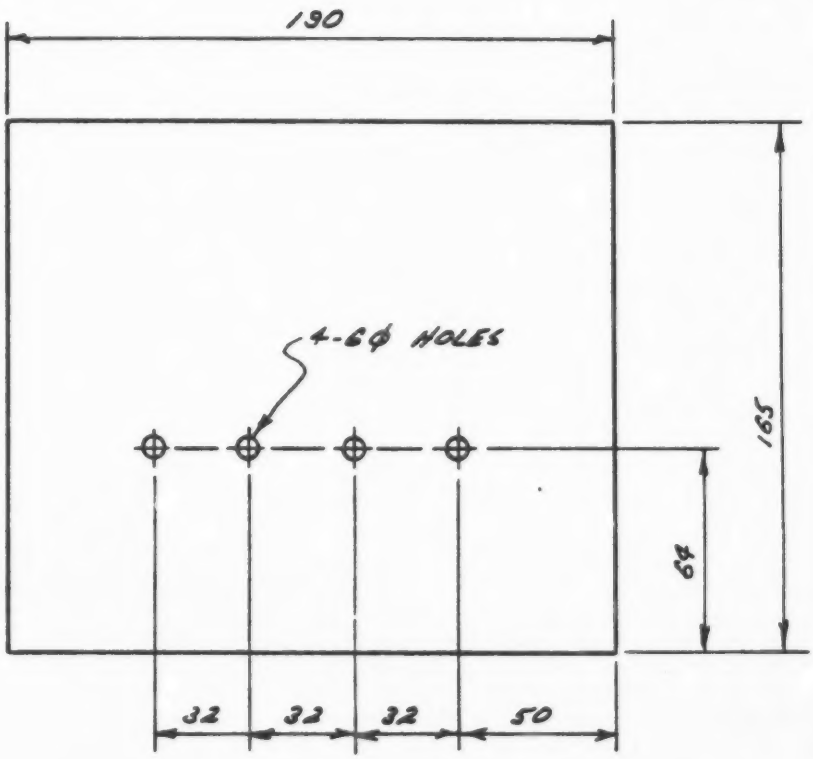

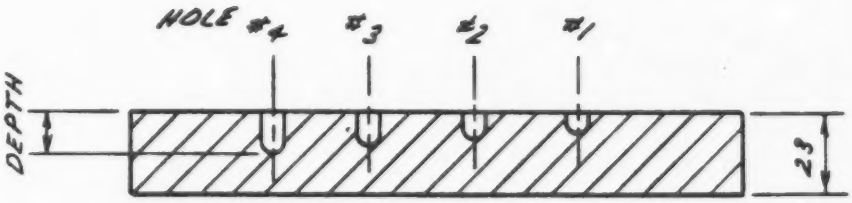

HOLE NO	DEPTH
#1	6.4
#2	7.7
#3	9.7
#4	11.3

NOTE: - BOTTOM OF HOLES ARE ROUND.
- ALL DIMENSIONS ARE MILLIMETRES.

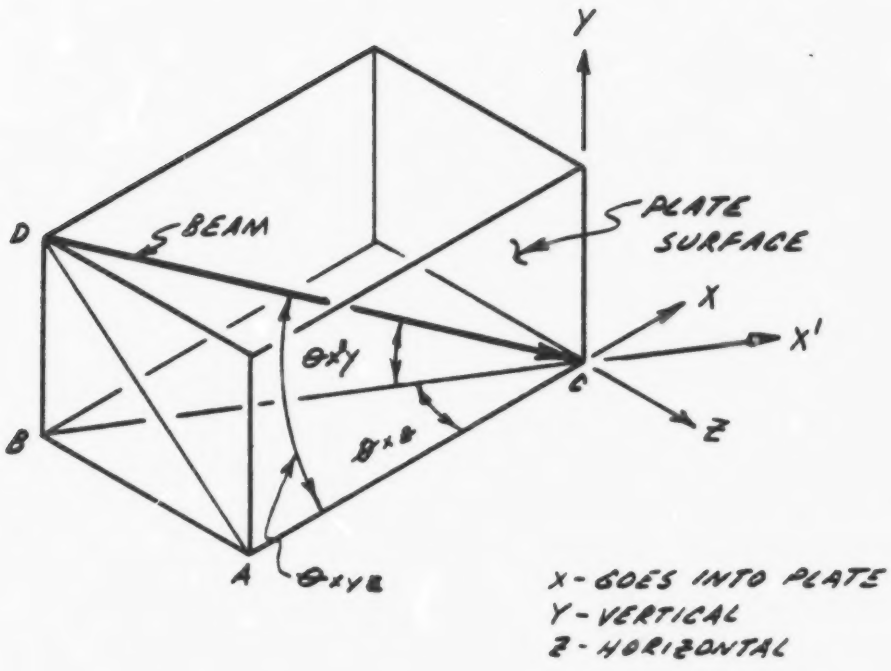

FIG. NO. 14(a)

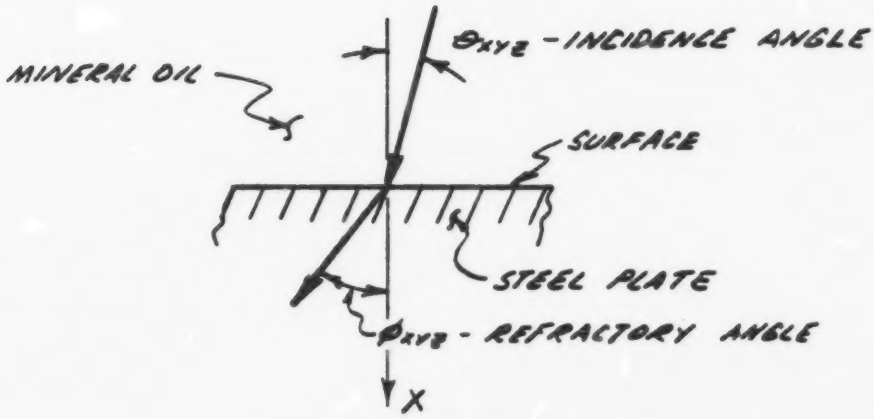

FIG. NO. 14(b)

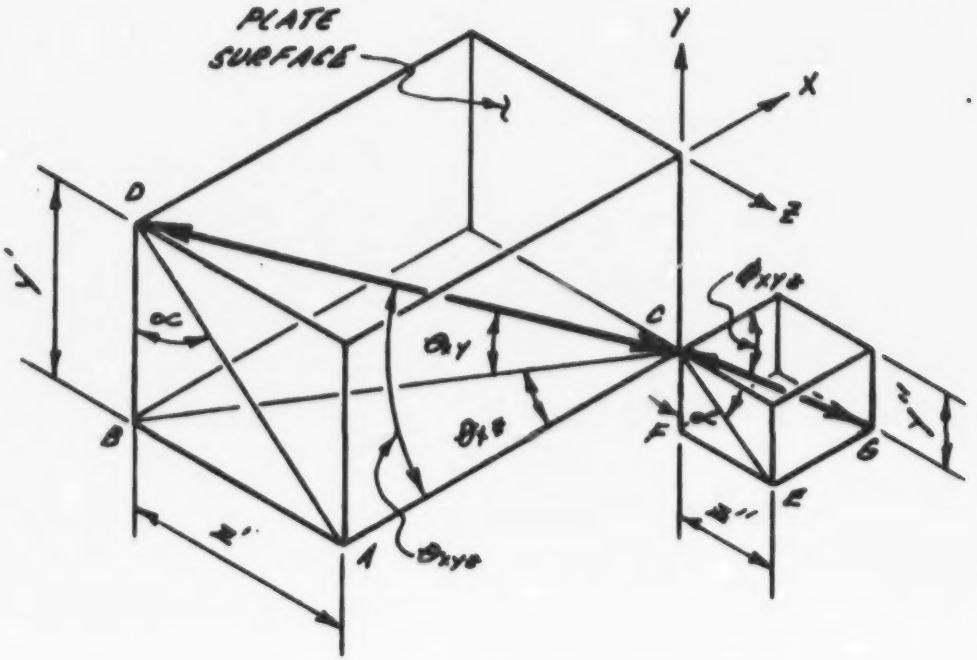
PLATE
SURFACE
Y
X
Z
D
C
B
A
E
F
G
α
θ_{xy}
θ_{yz}
θ_{xyz}
θ_{xyz}
y'
x'
x''
z

FIG 15

ANGLE PROBE MECHANISM

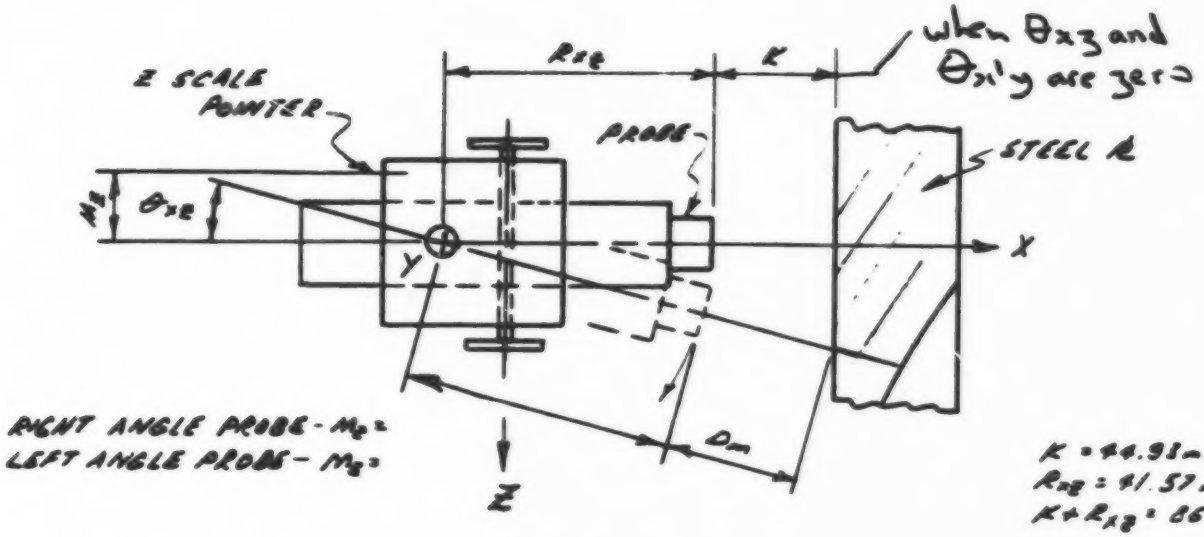

TOP VIEW

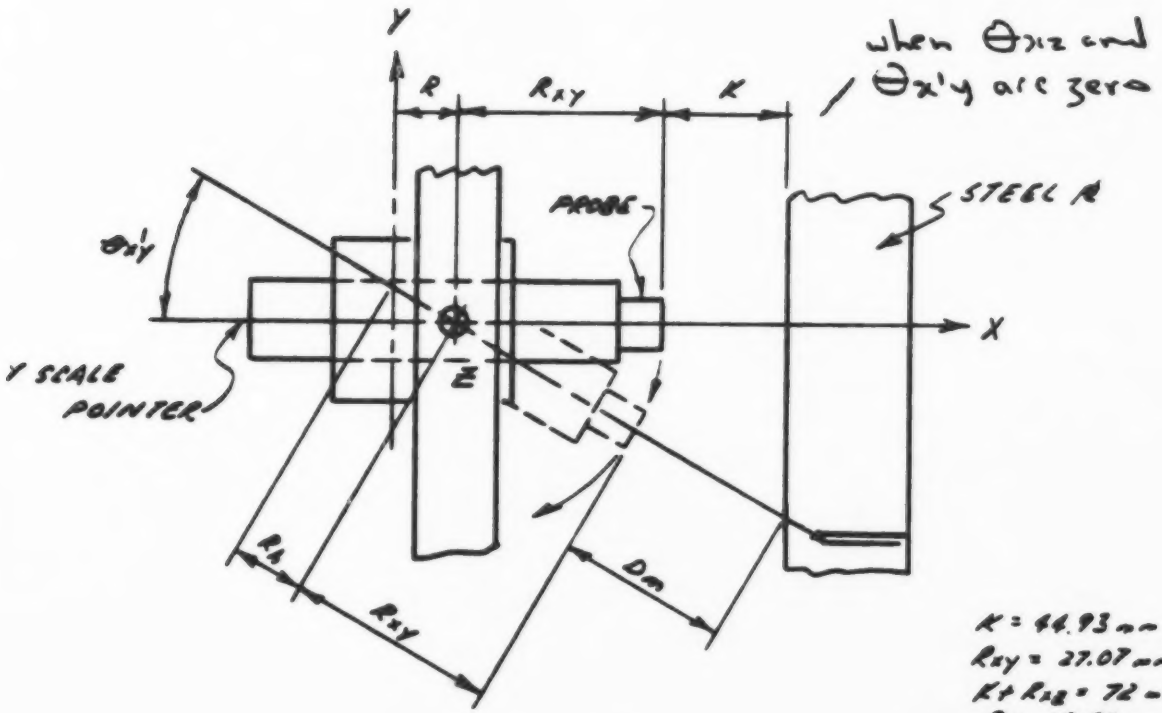

SIDE VIEW

FIG. NO. 16

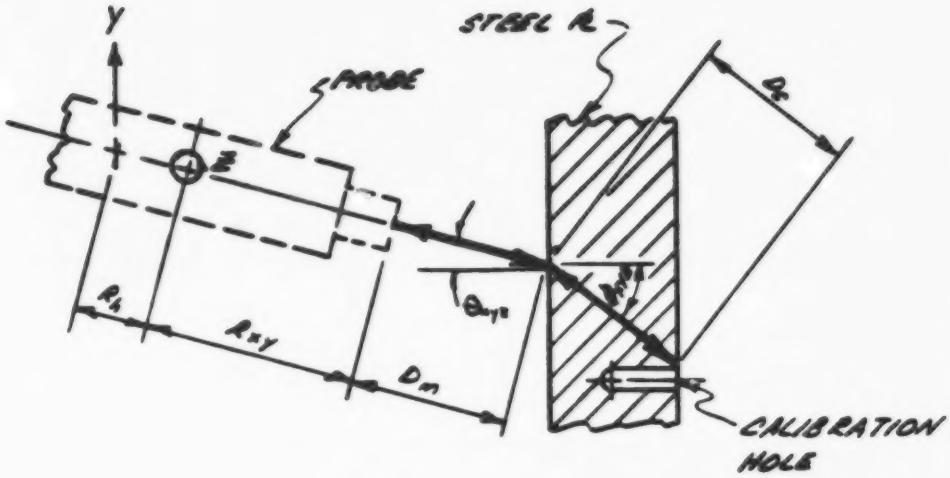

FIG NO-17a*

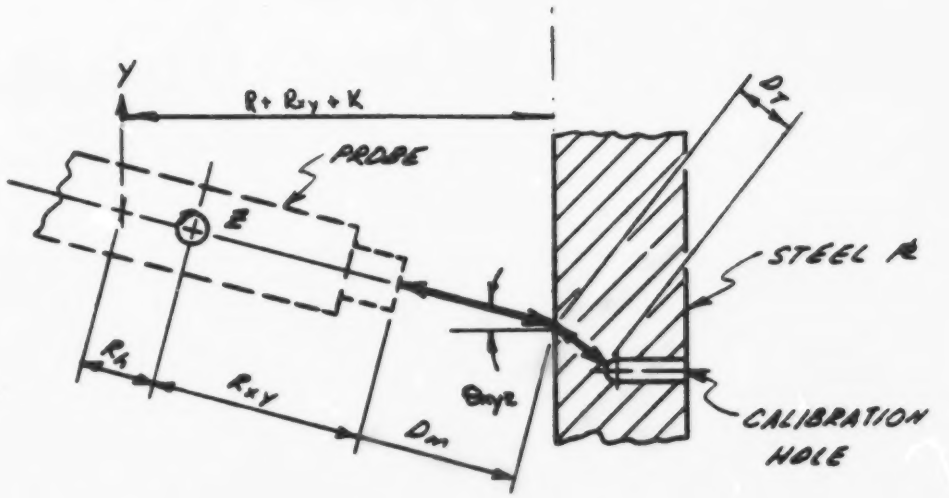

FIG NO-17b*

* Figs. and are views looking perpendicular to the plane that contains the surfaces DCA and CGE.

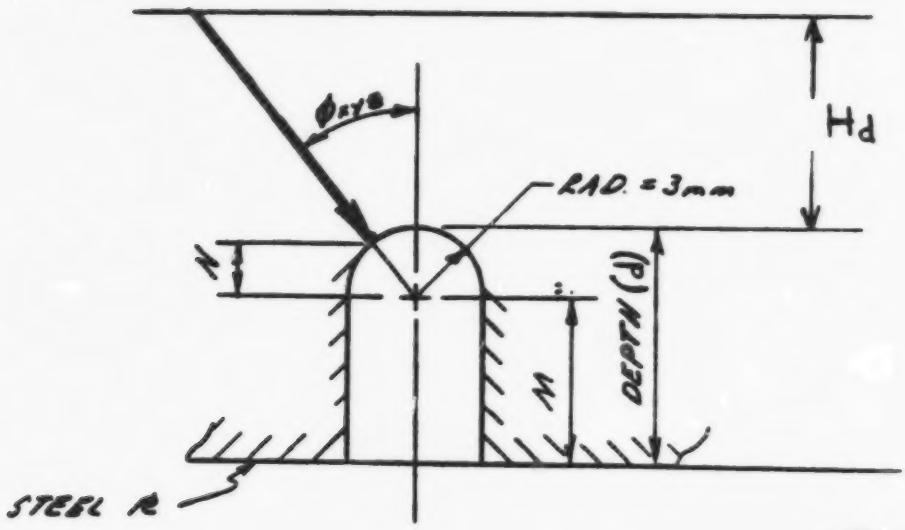

FIG 18

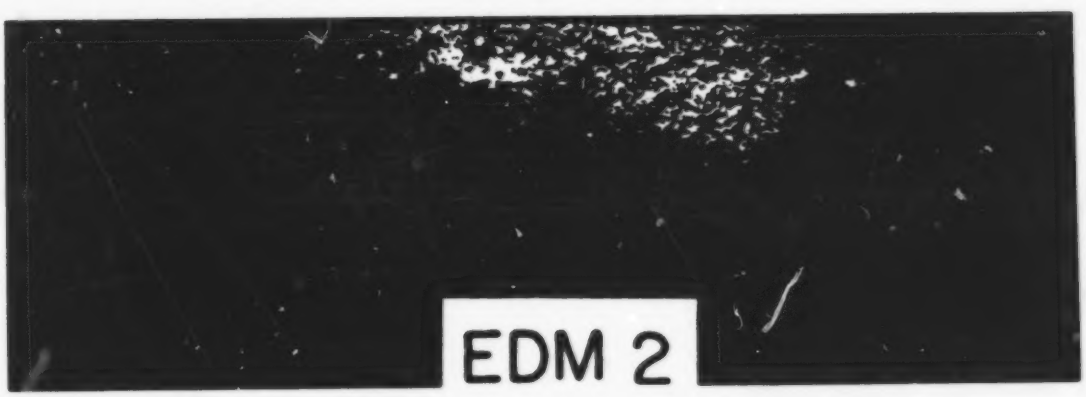

FIG. NO. 19

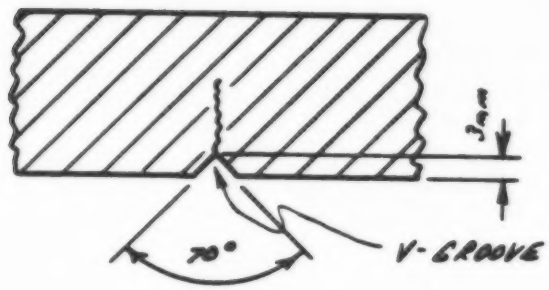

WELD PREPARATION (a)

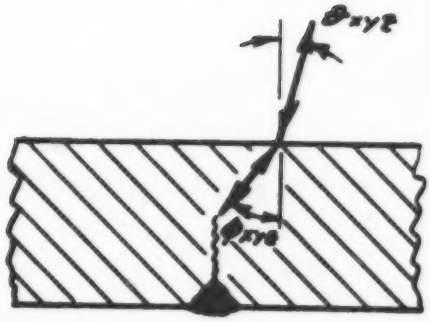

V-GROOVE WELD (b)

FIG 20

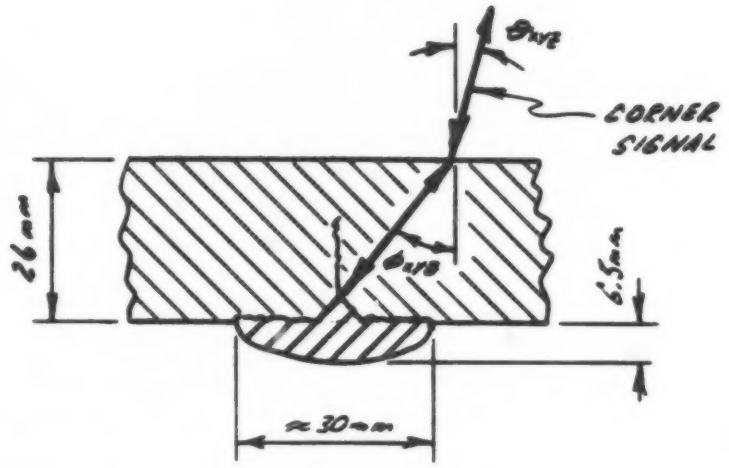

WELD CAP (a)

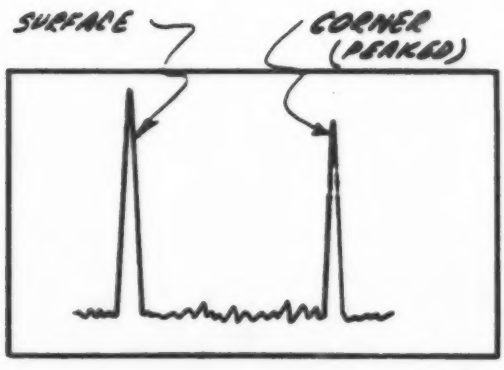

(b) CORNER SIGNAL

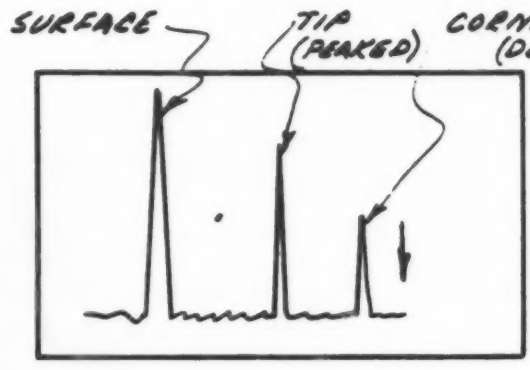

(c) TIP SIGNAL

FIG 21

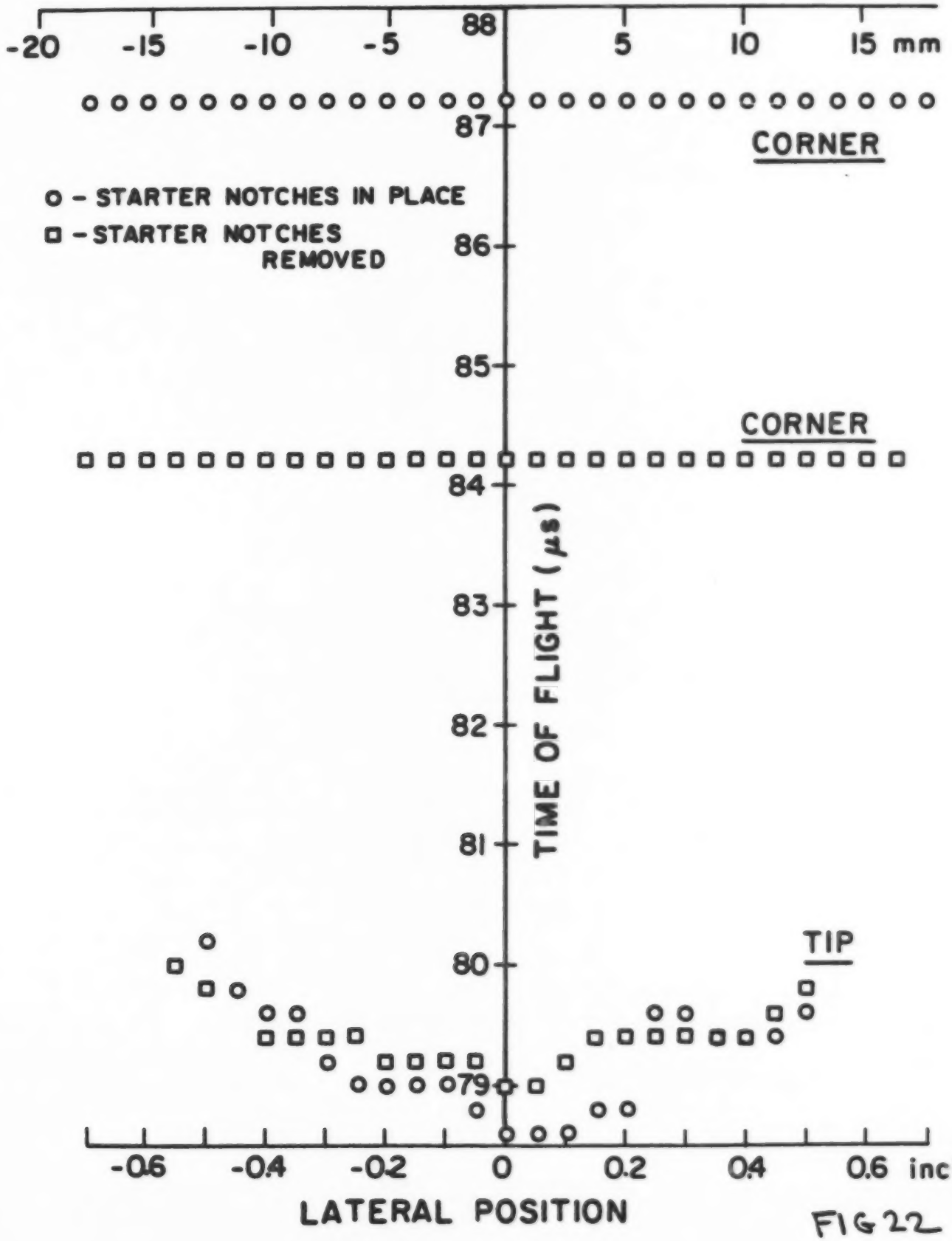
-20
-15
-10
-5
88
5
10
15 mm
87
CORNER
o - STARTER NOTCHES IN PLACE
□ - STARTER NOTCHES REMOVED
86
85
CORNER
84
83
82
81
TIME OF FLIGHT (μs)
TIP
80
79
-0.6
-0.4
-0.2
0
0.2
0.4
0.6 inch
LATERAL POSITION

FIG 22

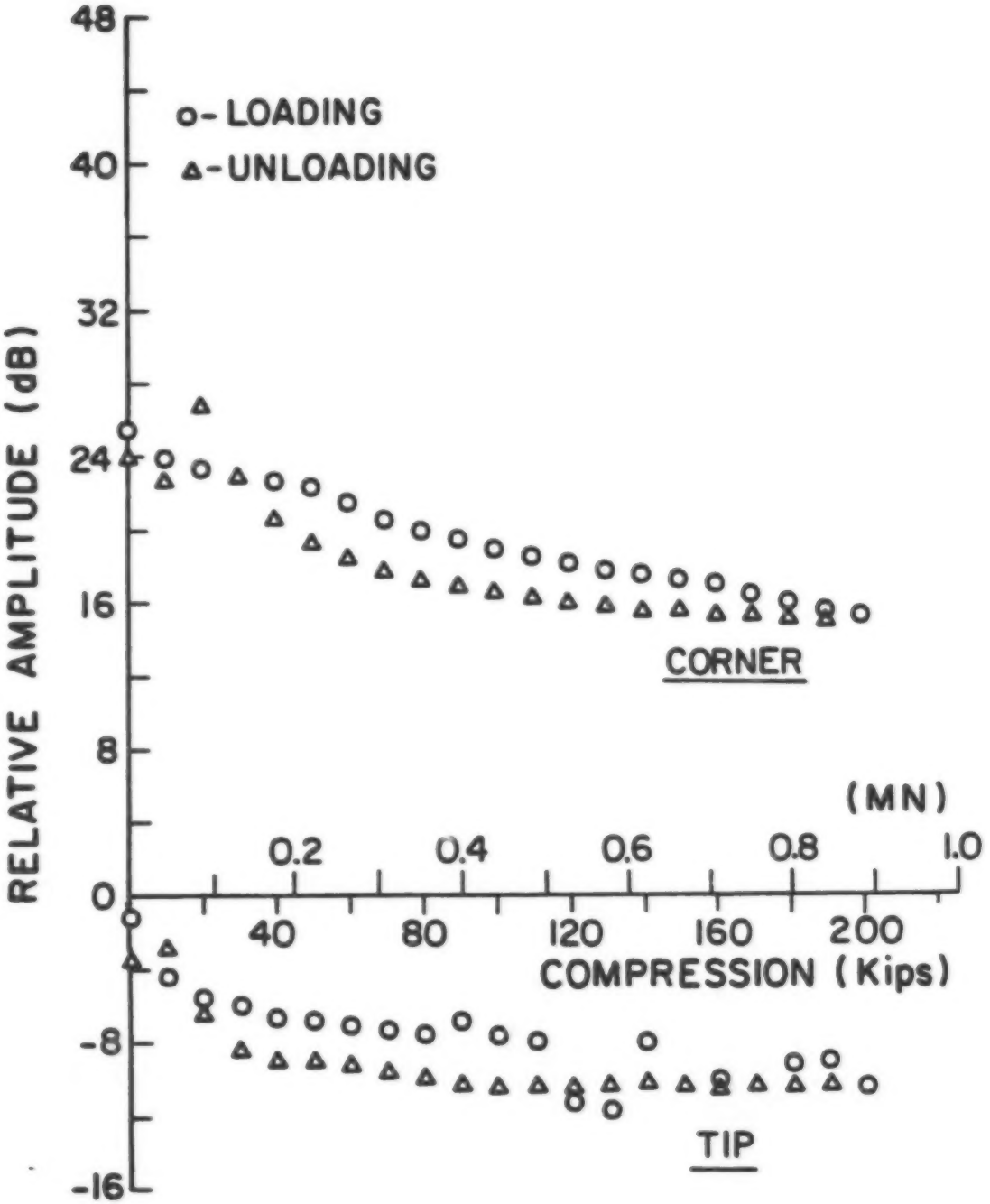
48
40
32
24
16
8
0
-8
-16
o- LOADING
Δ- UNLOADING
RELATIVE AMPLITUDE (dB)
CORNER
TIP
(MN)
0.2
0.4
0.6
0.8
1.0
40
80
120
160
200
COMPRESSION (Kips)

FIG 23

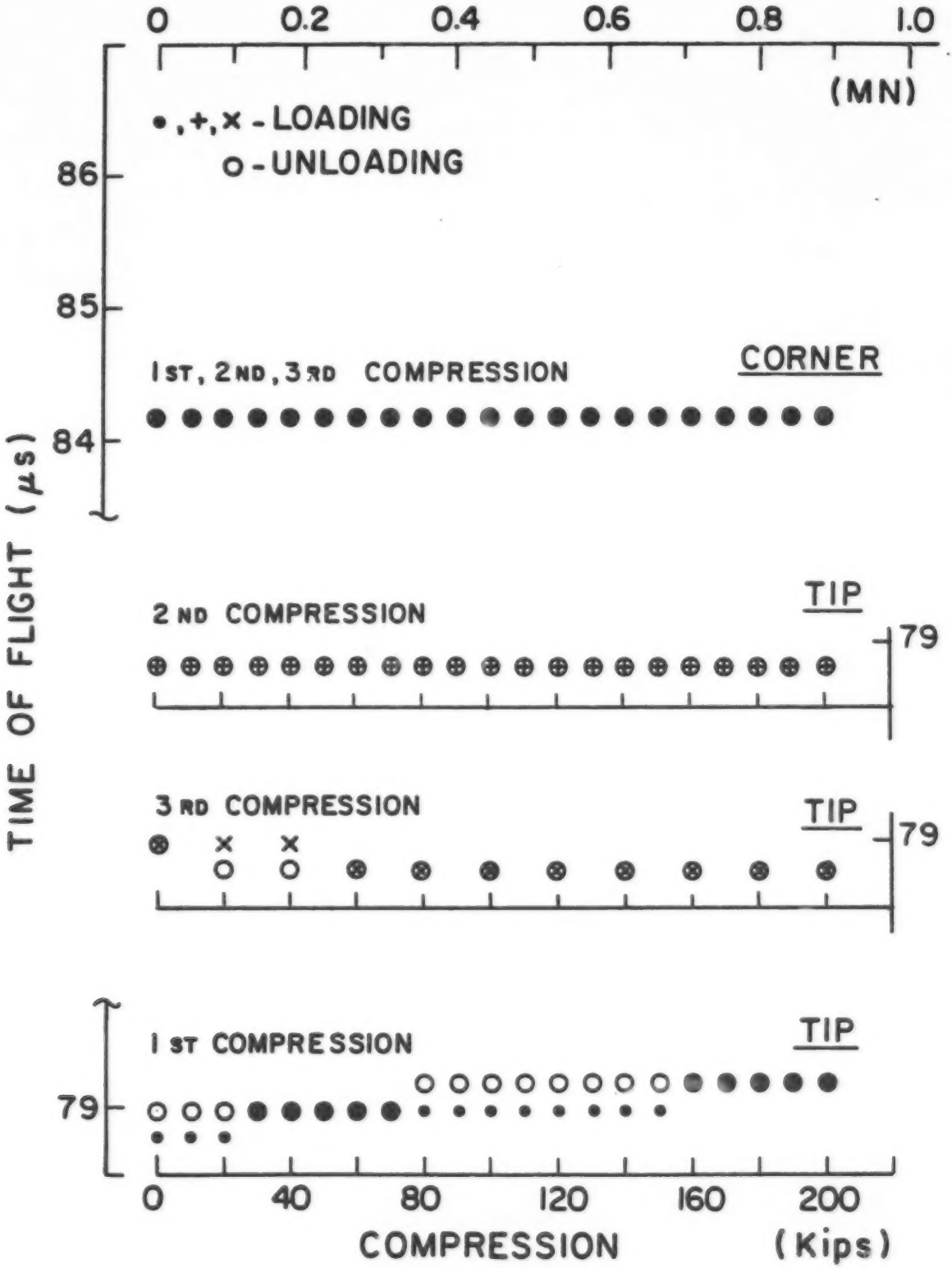
0
0.2
0.4
0.6
0.8
1.0
(MN)
•, +, × - LOADING
o - UNLOADING
86
85
84
1ST, 2ND, 3RD COMPRESSION
CORNER
2 ND COMPRESSION
TIP
79
3 RD COMPRESSION
TIP
79
1 ST COMPRESSION
TIP
79
TIME OF FLIGHT (μs)
0
40
80
120
160
200
COMPRESSION
(Kips)

FIG 24

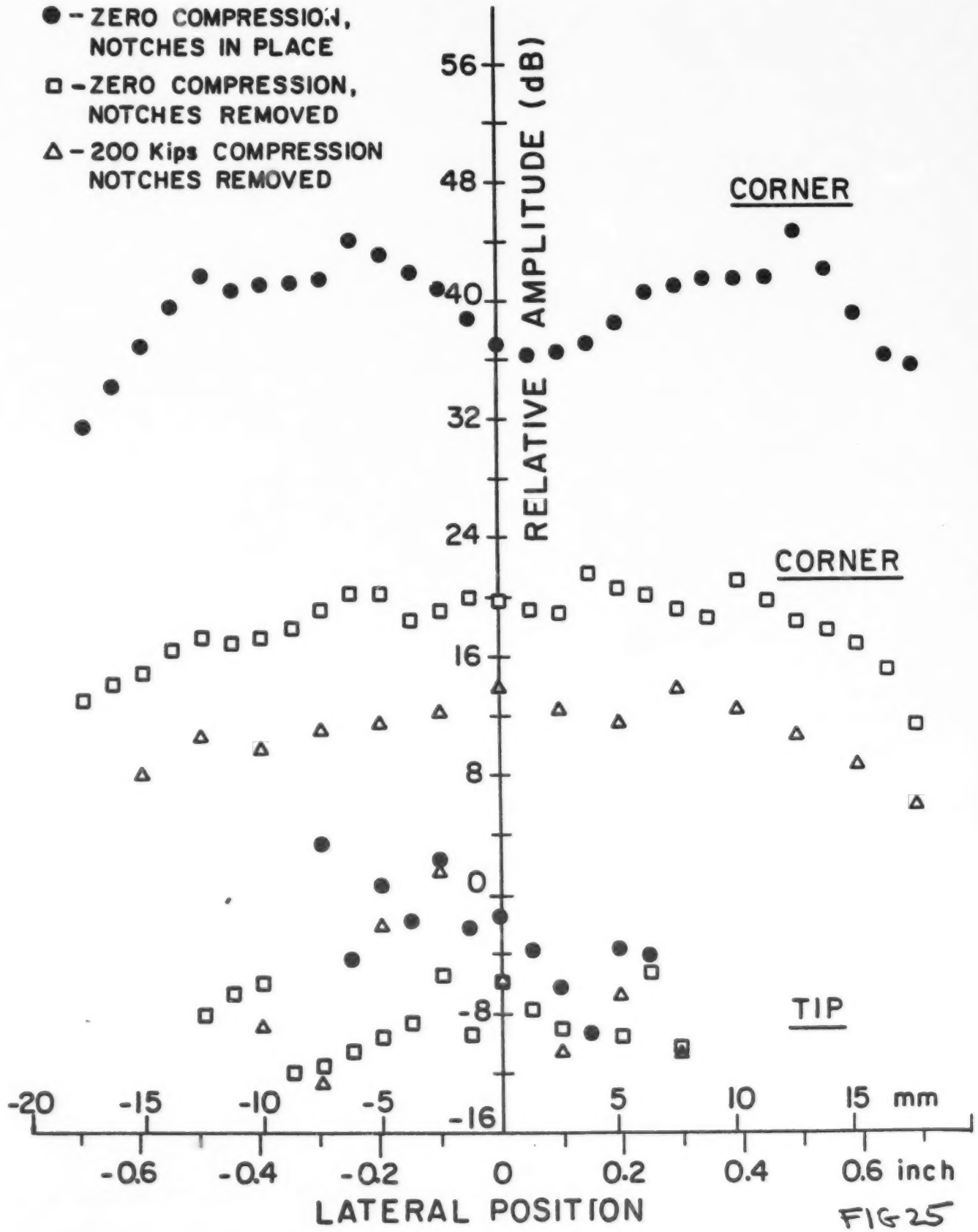
● - ZERO COMPRESSION, NOTCHES IN PLACE
□ - ZERO COMPRESSION, NOTCHES REMOVED
△ - 200 Kips COMPRESSION NOTCHES REMOVED
RELATIVE AMPLITUDE (dB)
56
48
40
32
24
16
8
0
-8
-16
CORNER
CORNER
TIP
-20
-15
-10
-5
5
10
15 mm
-0.6
-0.4
-0.2
0
0.2
0.4
0.6 inch
LATERAL POSITION

FIG 25

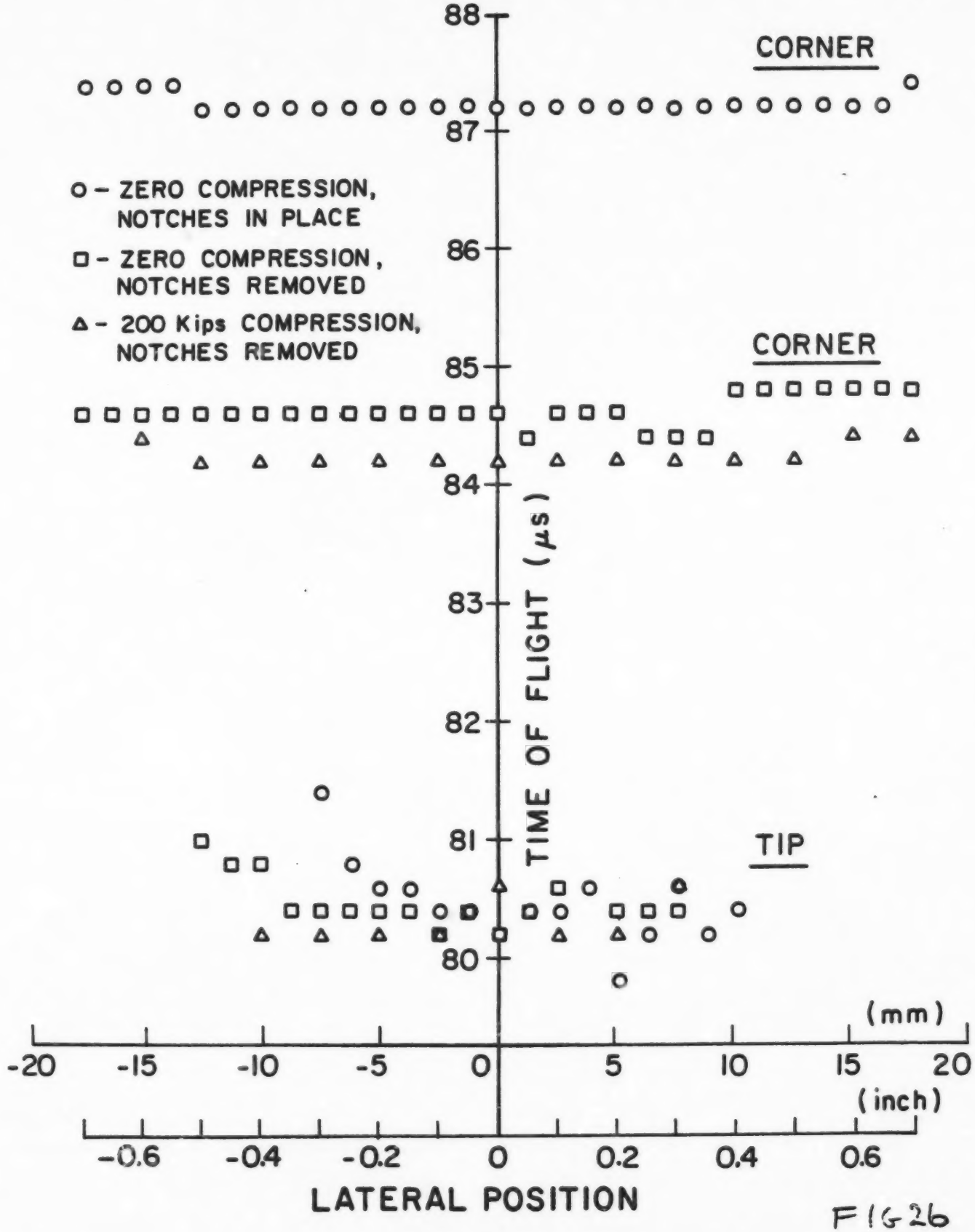
88
87
86
85
84
83
82
81
80
CORNER
CORNER
TIP
○ – ZERO COMPRESSION, NOTCHES IN PLACE
□ – ZERO COMPRESSION, NOTCHES REMOVED
△ – 200 Kips COMPRESSION, NOTCHES REMOVED
TIME OF FLIGHT (μs)
(mm)
-20 -15 -10 -5 0 5 10 15 20
(inch)
-0.6 -0.4 -0.2 0 0.2 0.4 0.6
LATERAL POSITION

FIG 26

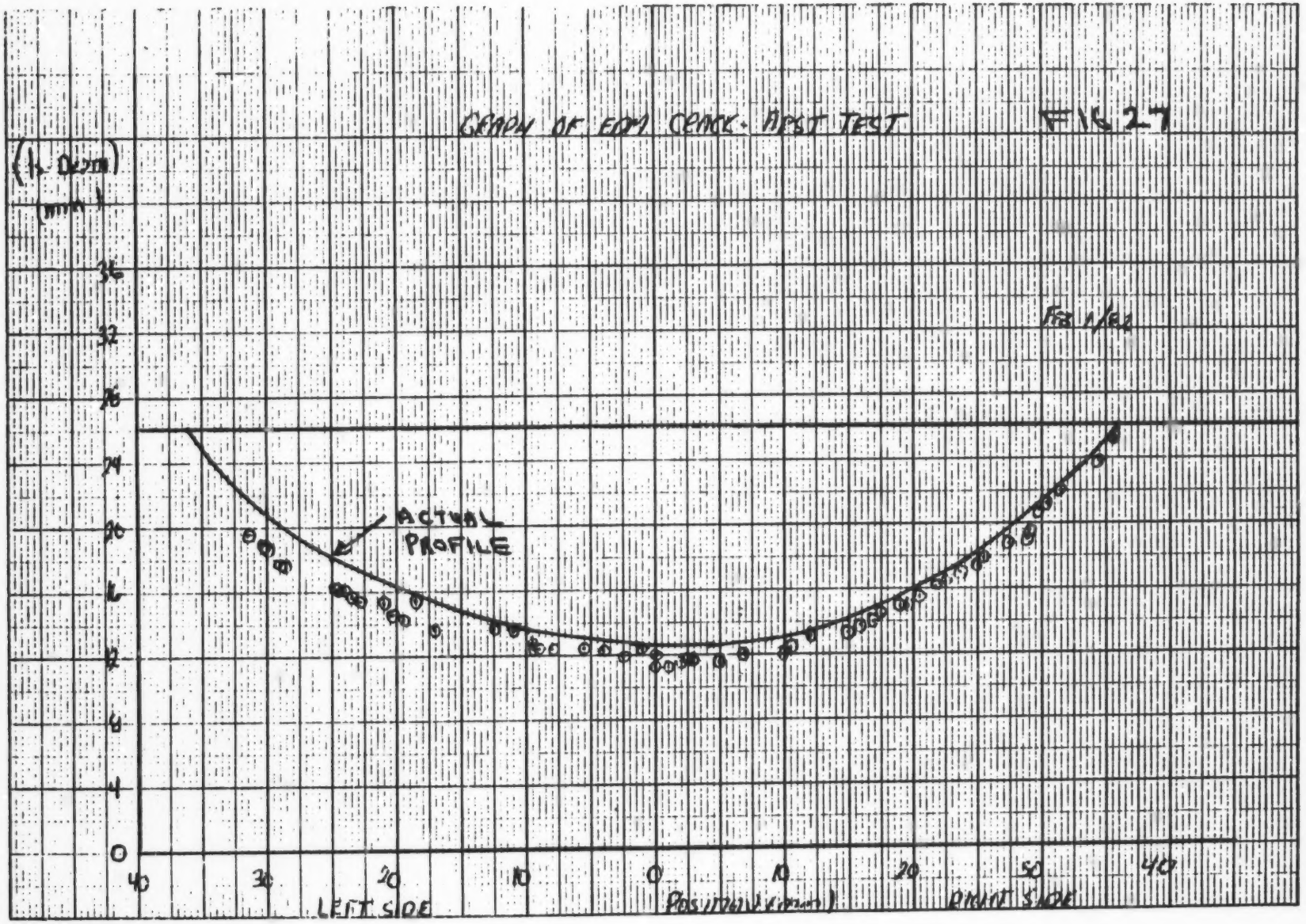
GRAPH OF FOR CENTR. REST TEST
FIG 2.7
(½ Dia in mm)
36
32
28
24
20
16
12
8
4
0
ACTUAL PROFILE
FOR ½ DIA
40
30
20
10
0
10
20
30
40
LEFT SIDE
(Positions in mm)
RIGHT SIDE

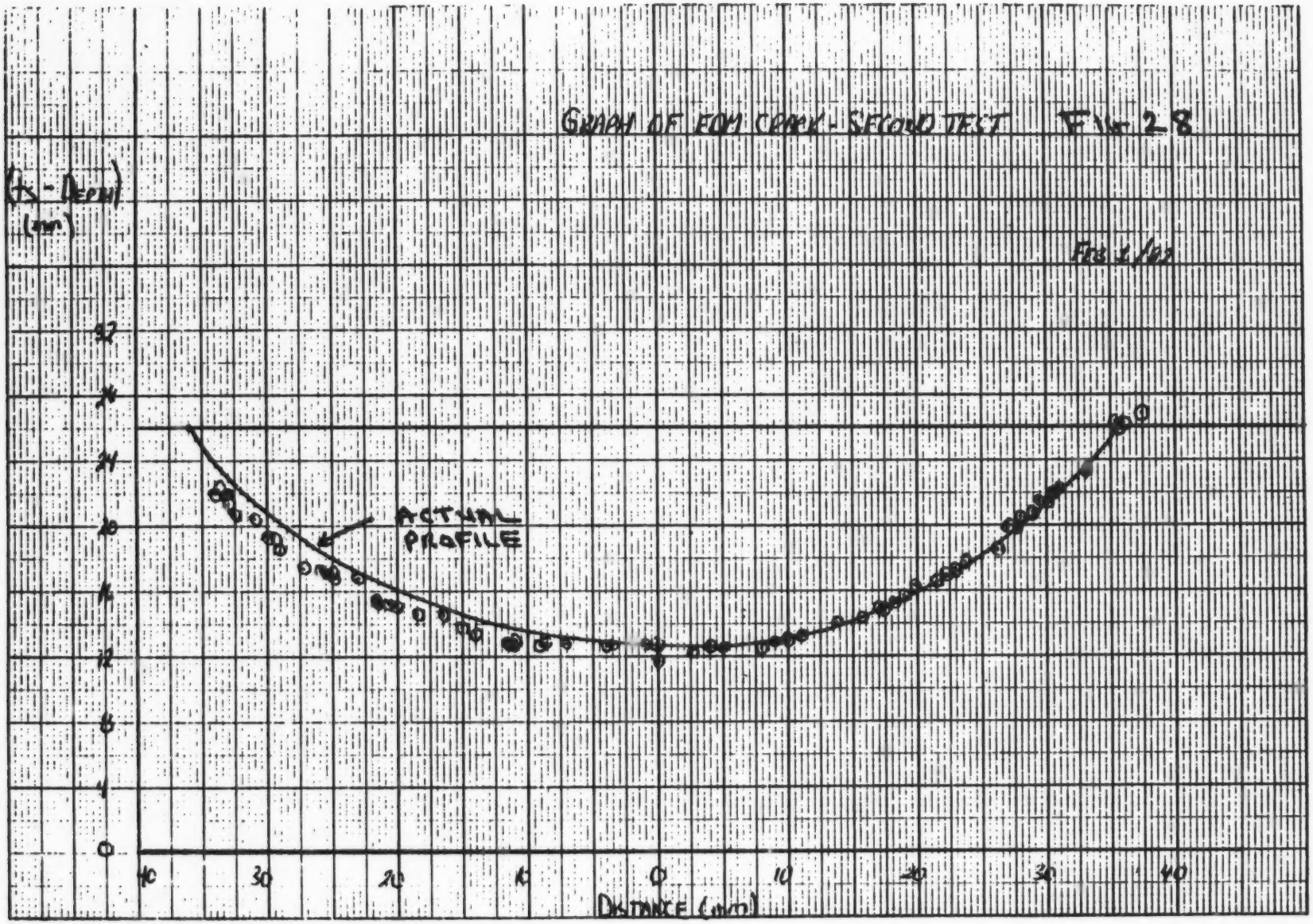
GRAPH OF EDM CRACK - SECOND TEST
Fig 2.8
(Y - DEPTH) (mm)
ACTUAL PROFILE
DISTANCE (mm)

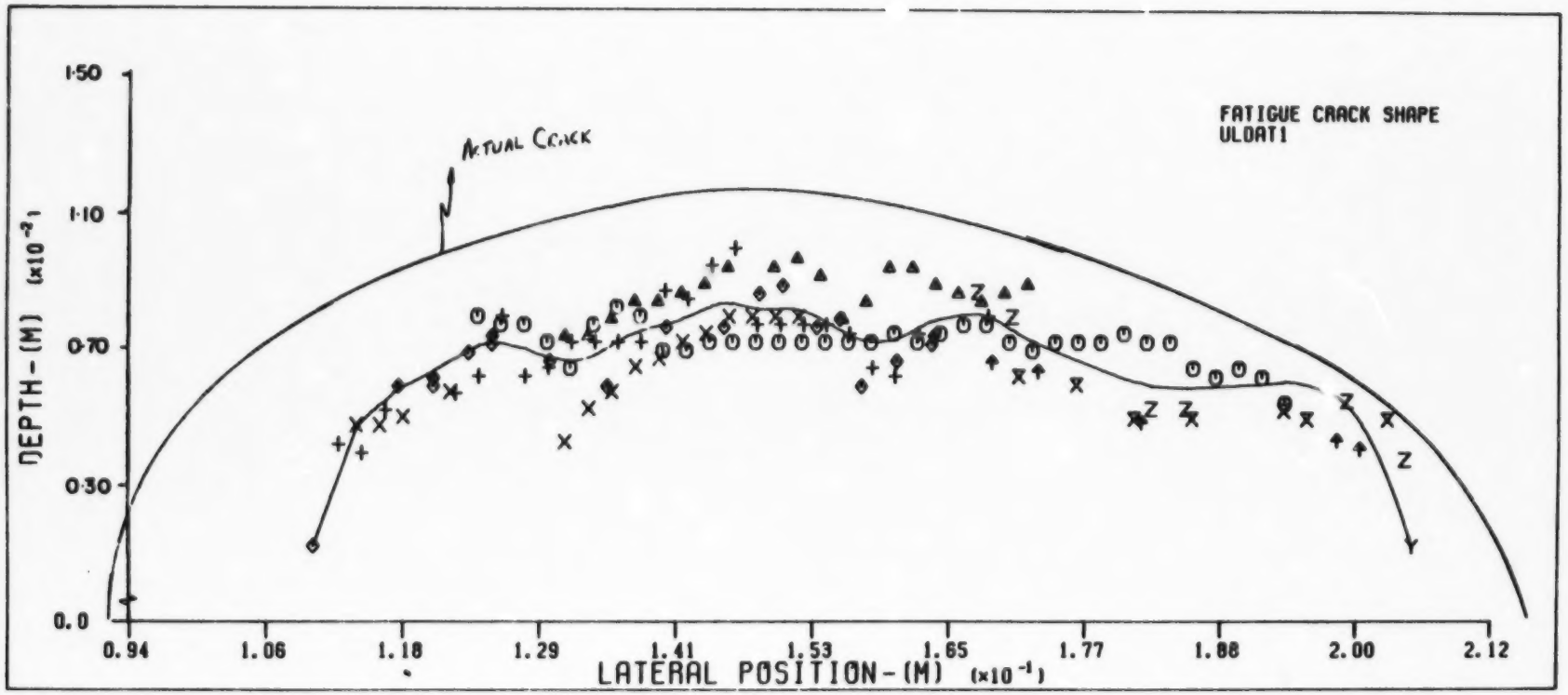
FATIGUE CRACK SHAPE
ULDATI
ACTUAL CRACK
DEPTH-(M) (x10⁻²)
1·50
1·10
0·70
0·30
0.0
0.94
1.06
1.18
1.29
1.41
1.53
1.65
1.77
1.88
2.00
2.12
LATERAL POSITION-(M) (x10⁻¹)

FIG 29

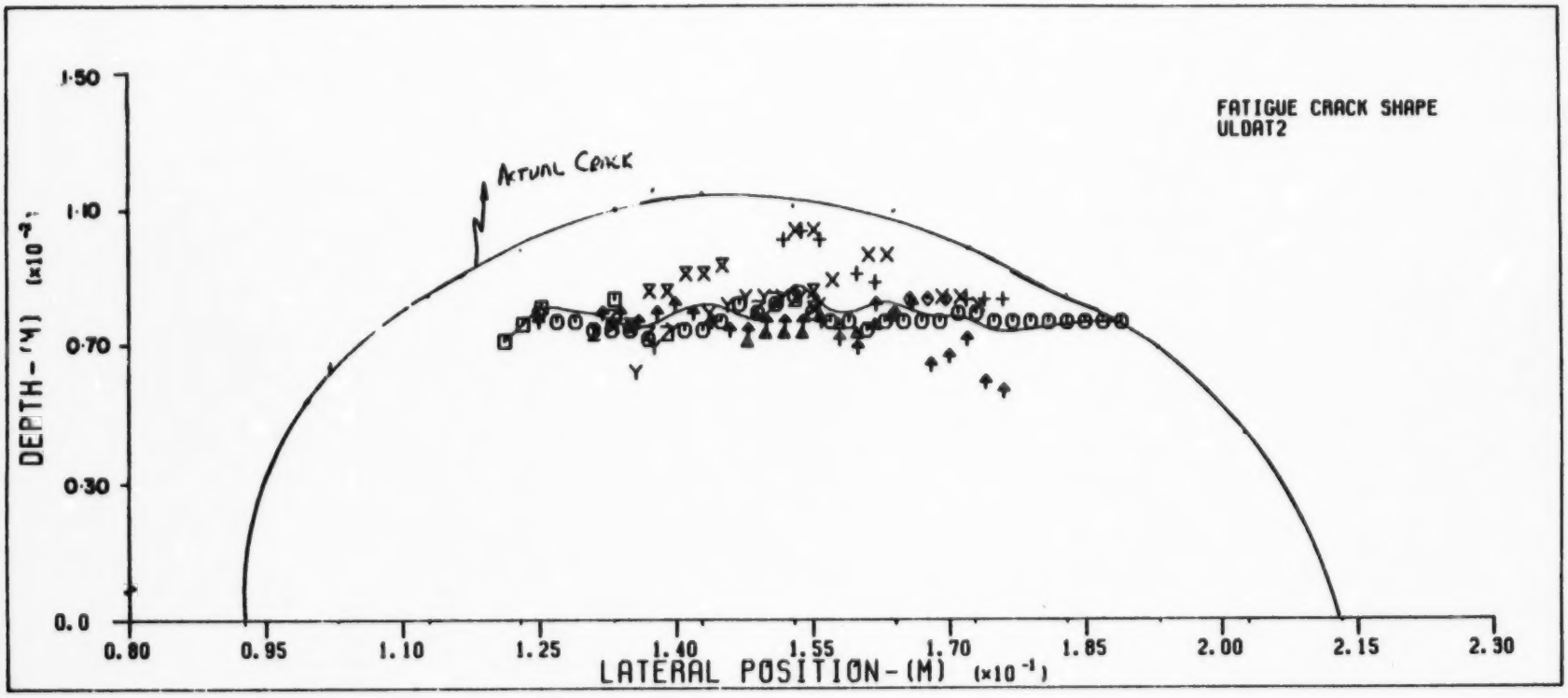
FATIGUE CRACK SHAPE
ULOAT2
ACTUAL CRACK
DEPTH-(M) (×10⁻²)
1.50
1.10
0.70
0.30
0.0
0.80
0.95
1.10
1.25
1.40
1.55
1.70
1.85
2.00
2.15
2.30
LATERAL POSITION-(M) (×10⁻¹)

FIG30

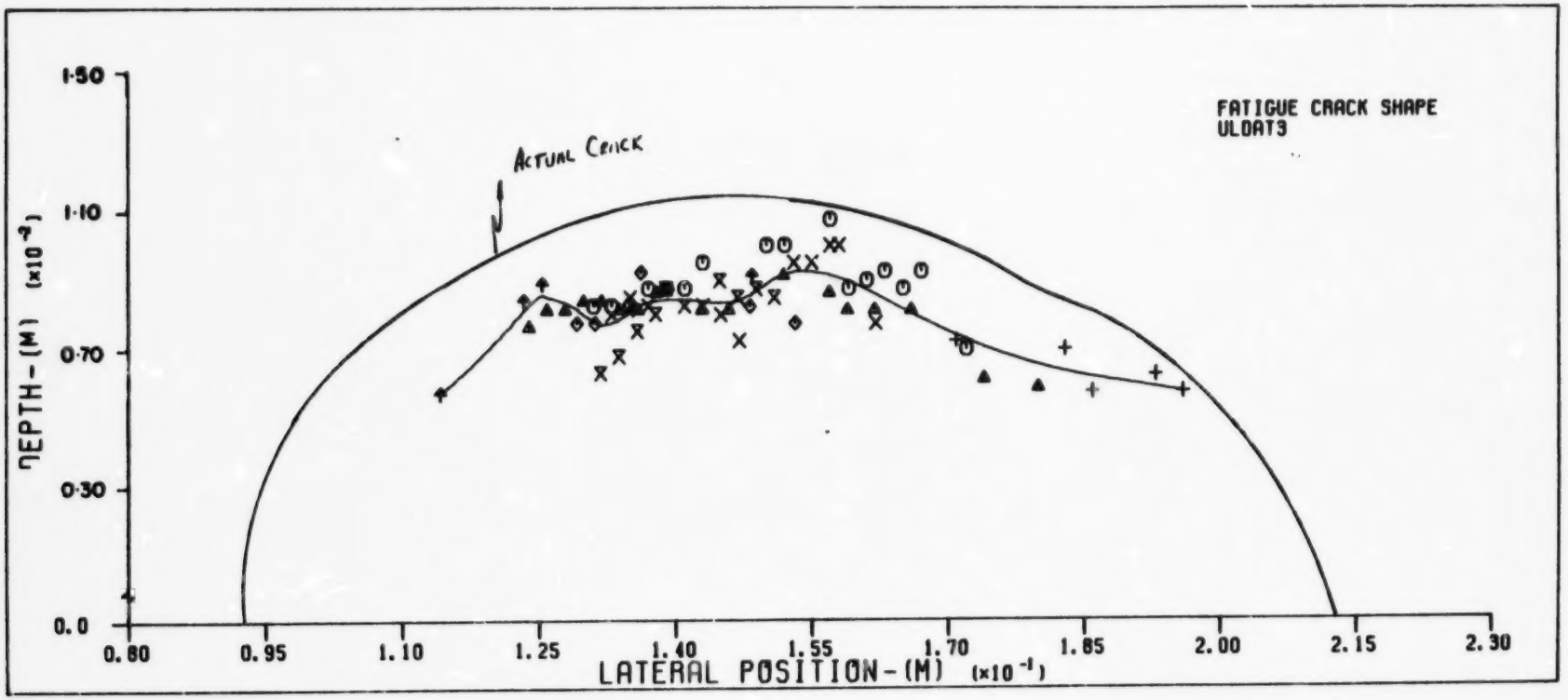
FATIGUE CRACK SHAPE
ULDAT3
ACTUAL CRACK
DEPTH-(M) (x10⁻³)
1.50
1.10
0.70
0.30
0.0
0.80
0.95
1.10
1.25
1.40
1.55
1.70
1.85
2.00
2.15
2.30
LATERAL POSITION-(M) (x10⁻¹)

FIG31

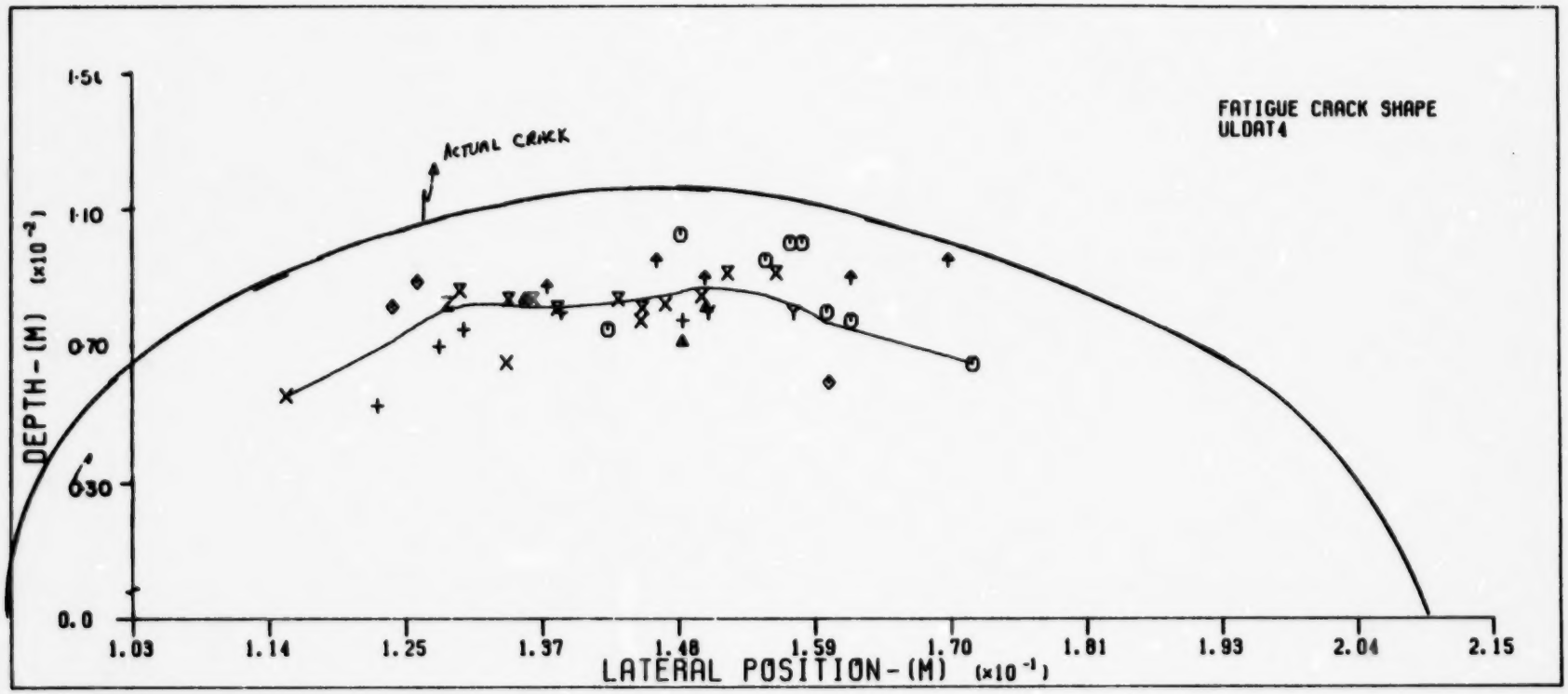
FATIGUE CRACK SHAPE
ULDAT4
ACTUAL CRACK
DEPTH-(M) (x10⁻²)
1.50
1.10
0.70
0.30
0.0
1.03
1.14
1.25
1.37
1.48
1.59
1.70
1.81
1.93
2.04
2.15
LATERAL POSITION-(M) (x10⁻¹)

FIG 32

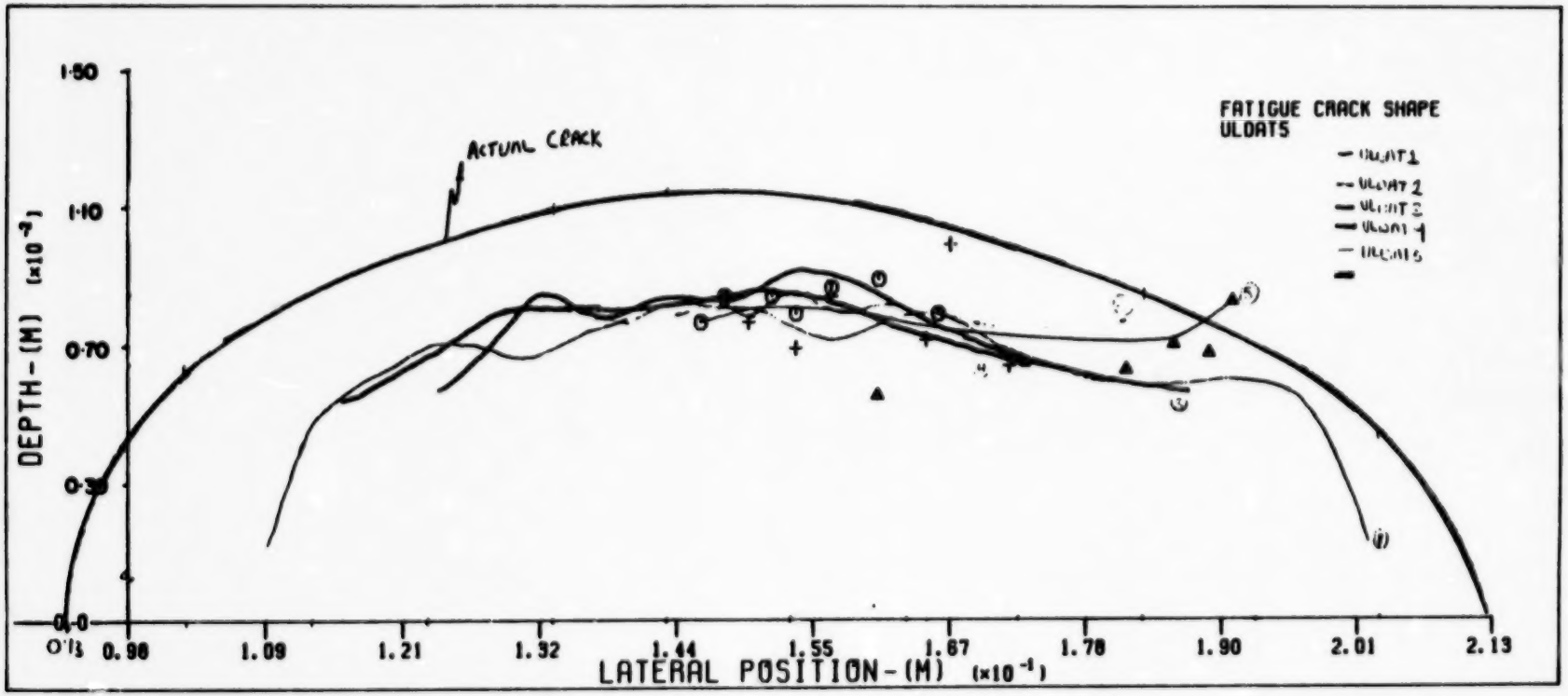
FATIGUE CRACK SHAPE
ULDAT5
ACTUAL CRACK
DEPTH-(M) (×10⁻²)
1·50
1·10
0·70
0·30
0·0
0·98
1.09
1.21
1.32
1.44
1.55
1.67
1.78
1.90
2.01
2.13
LATERAL POSITION-(M) (×10⁻¹)

FIG 33

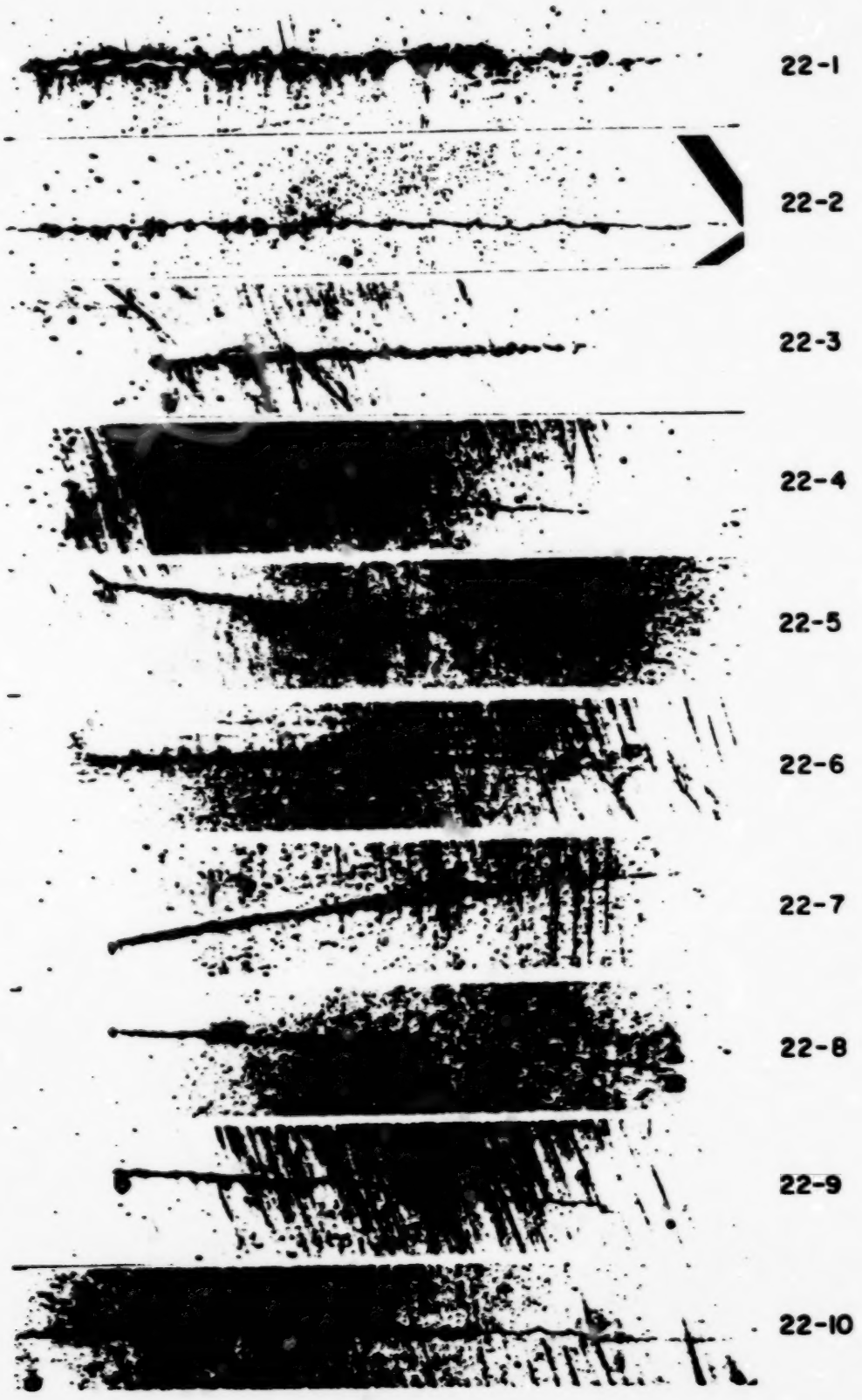

FIG. NO. 34

23-4 23-5 23-6 23-7 23-8

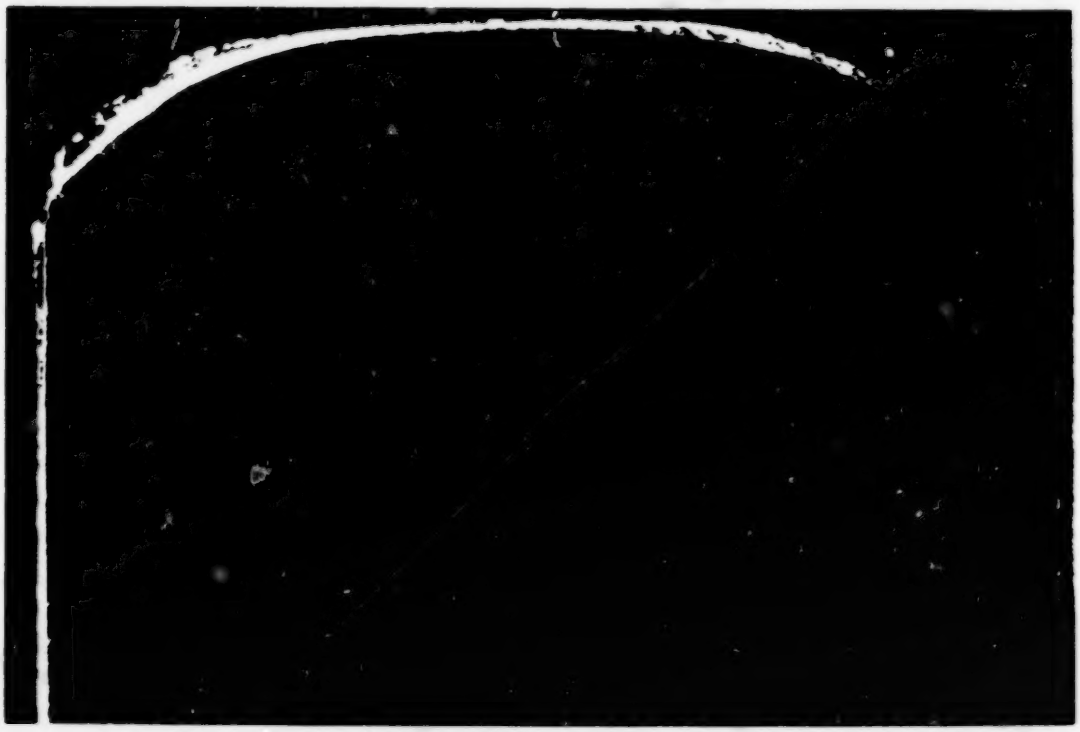

TYPICAL CRACK WITH WELD

FIG. NO. 35

PLATE 22

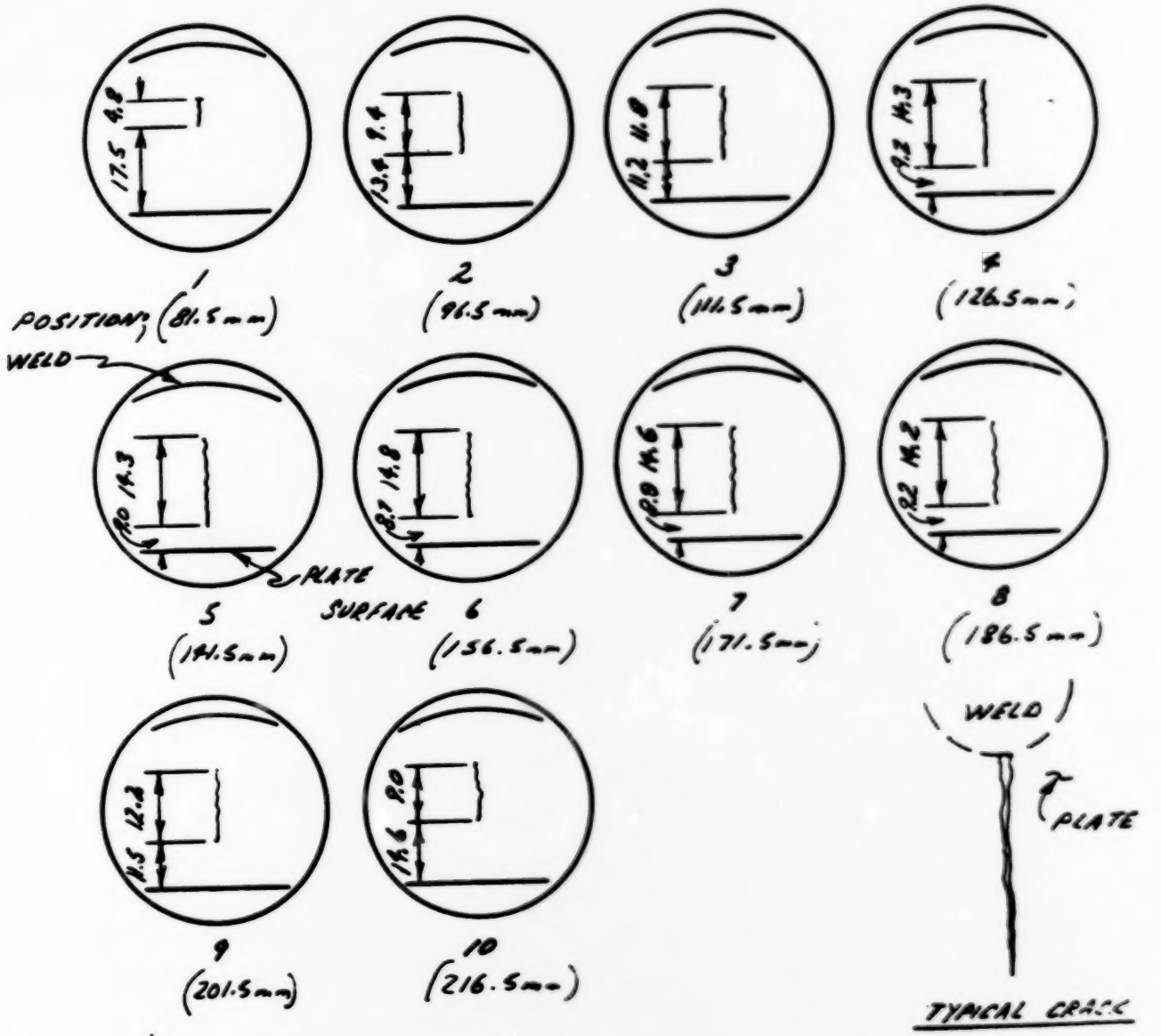

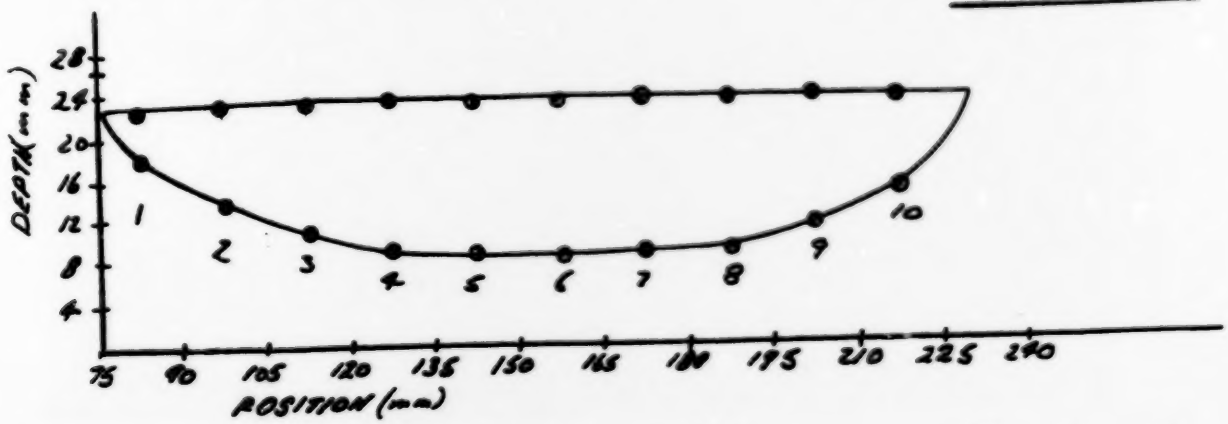

ACTUAL CRACK SHAPE

FIG. NO. 36

PLATE 23

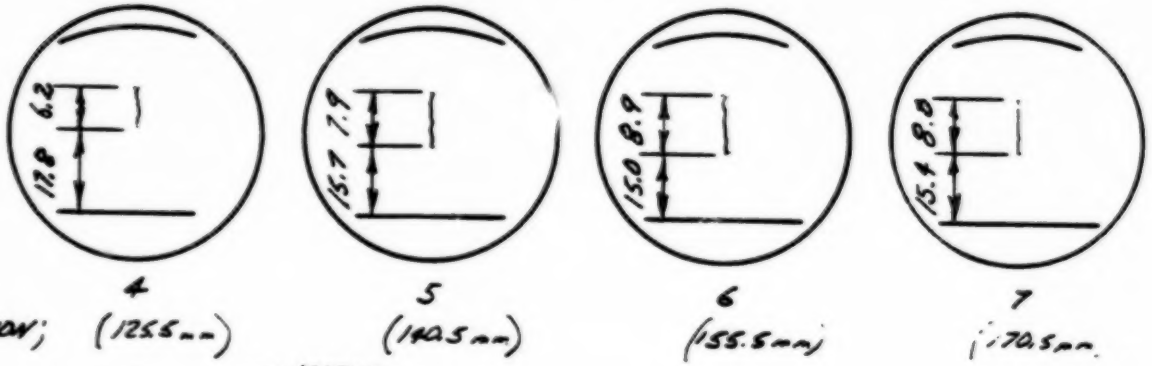

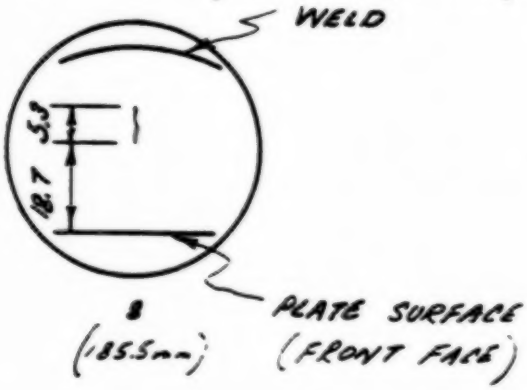

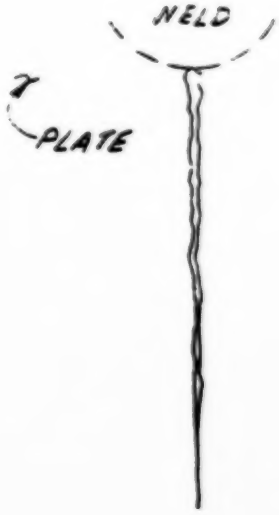

TYPICAL CRACK

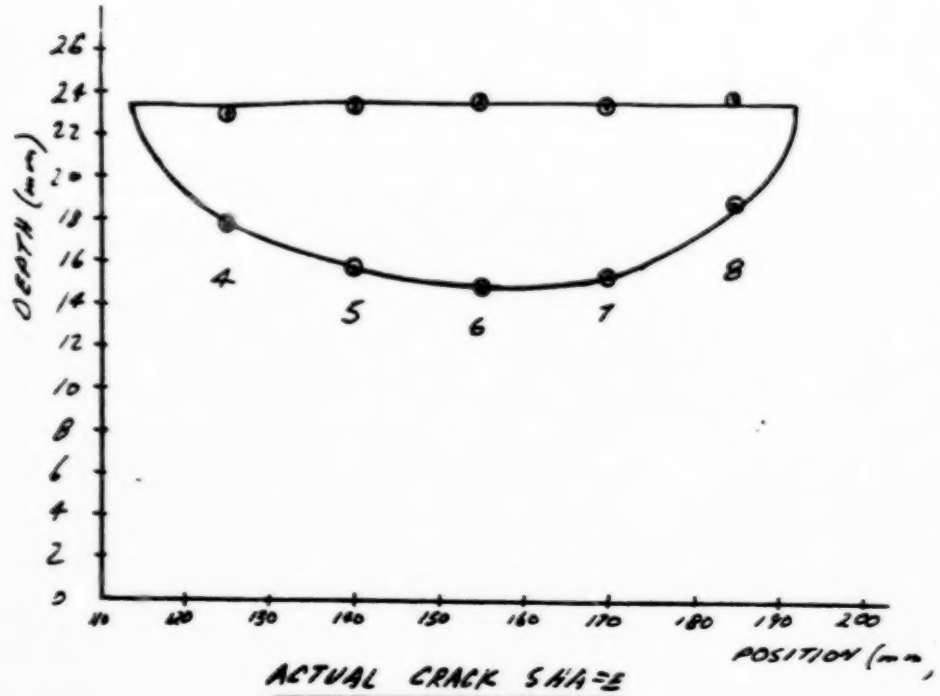

ACTUAL CRACK SHAPE

FIG. 110.37

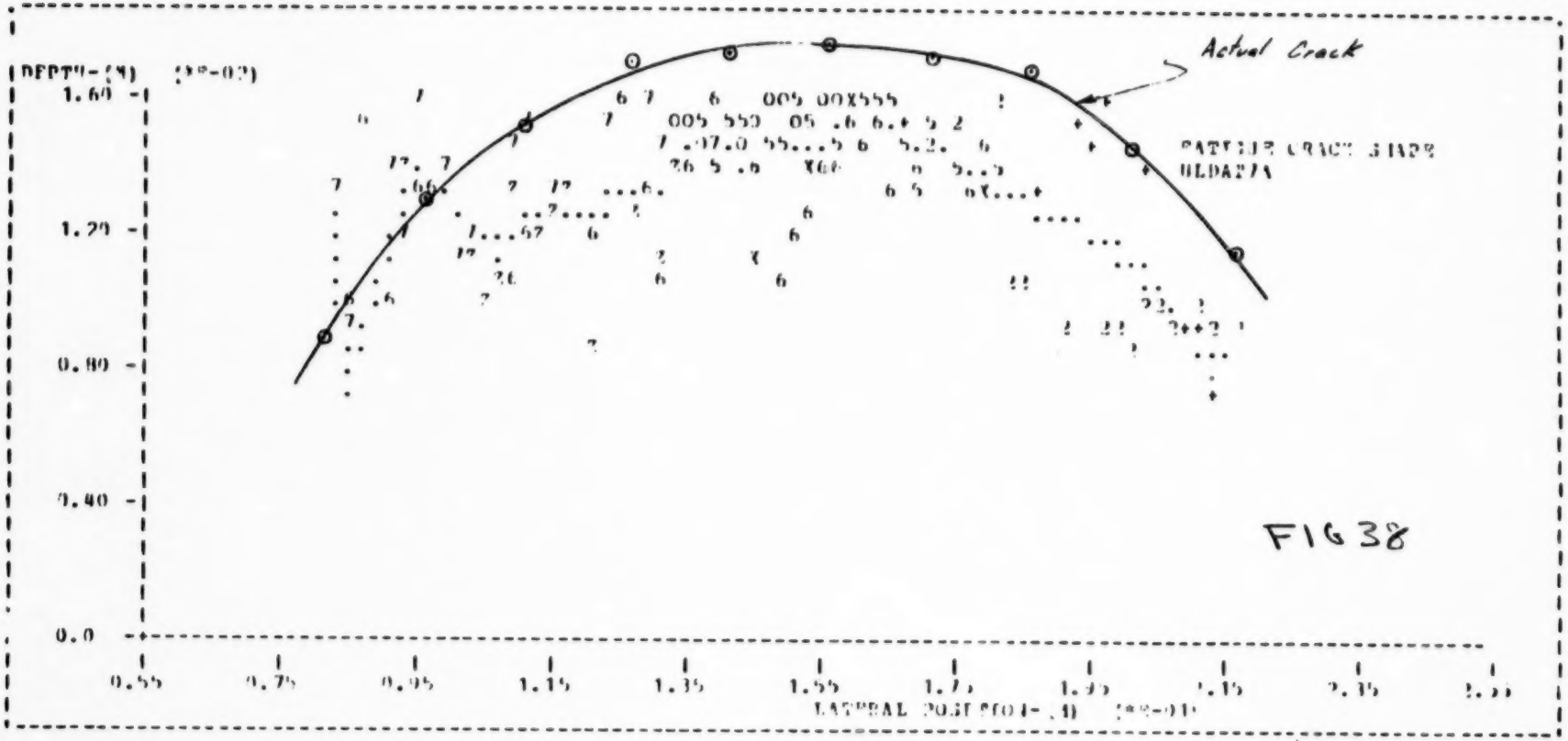

FIG 38

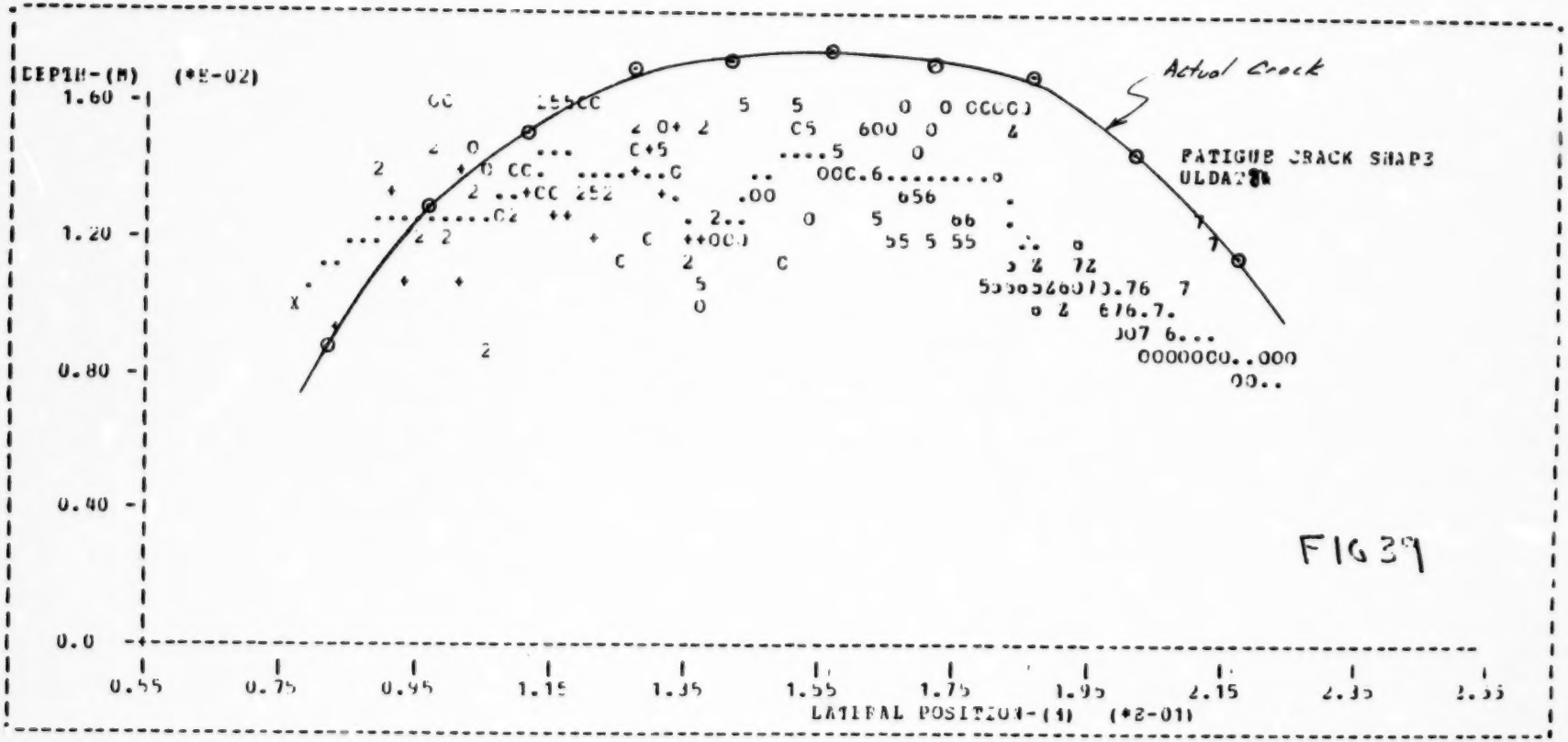
DEPTH-(M) (*E-02)
1.60
1.20
0.80
0.40
0.0
Actual Crack
FATIGUE CRACK SHAPE
0.55
0.75
0.95
1.15
1.35
1.55
1.75
1.95
2.15
2.35
2.55
LATERAL POSITION-(M) (*E-01)

FIG 39

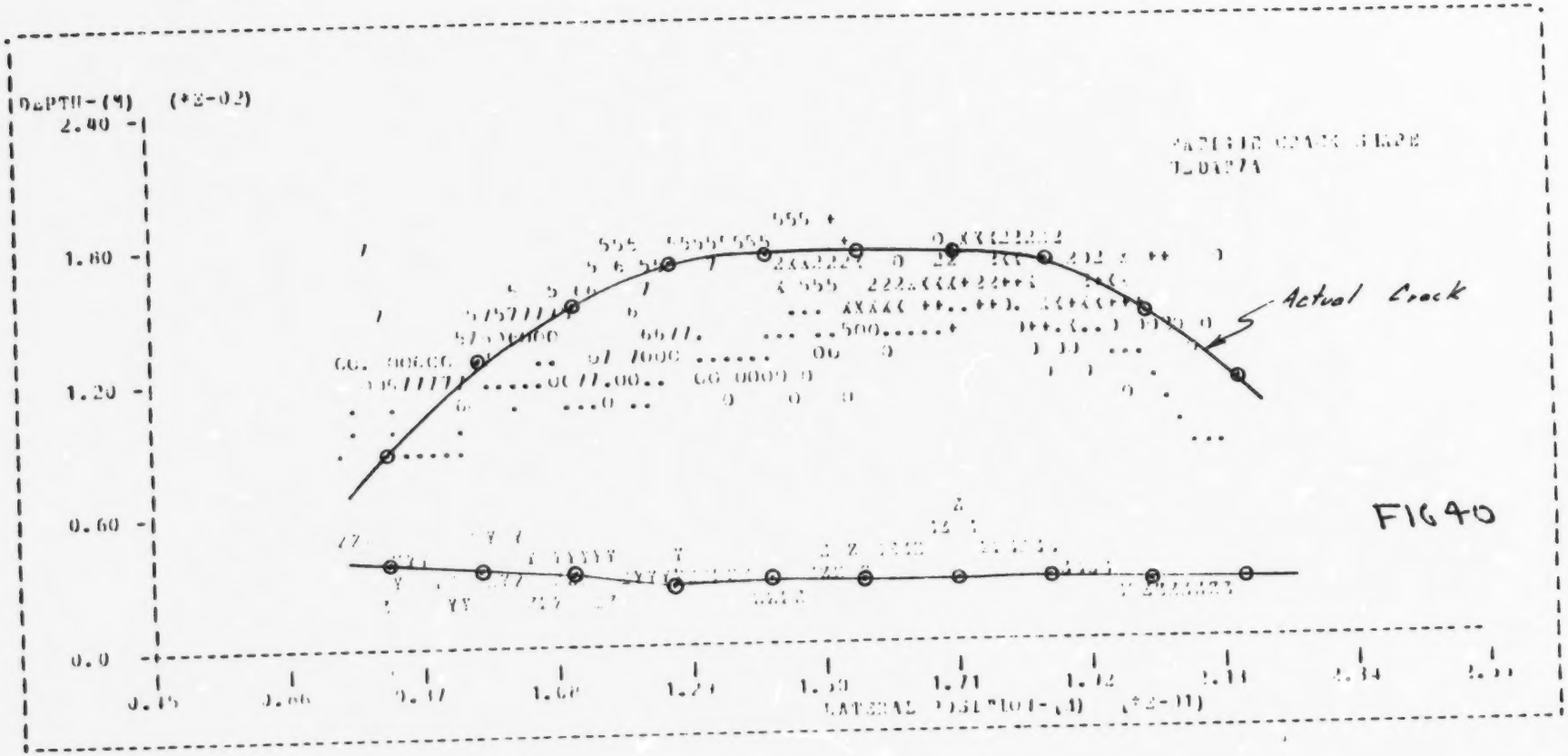

FIG40

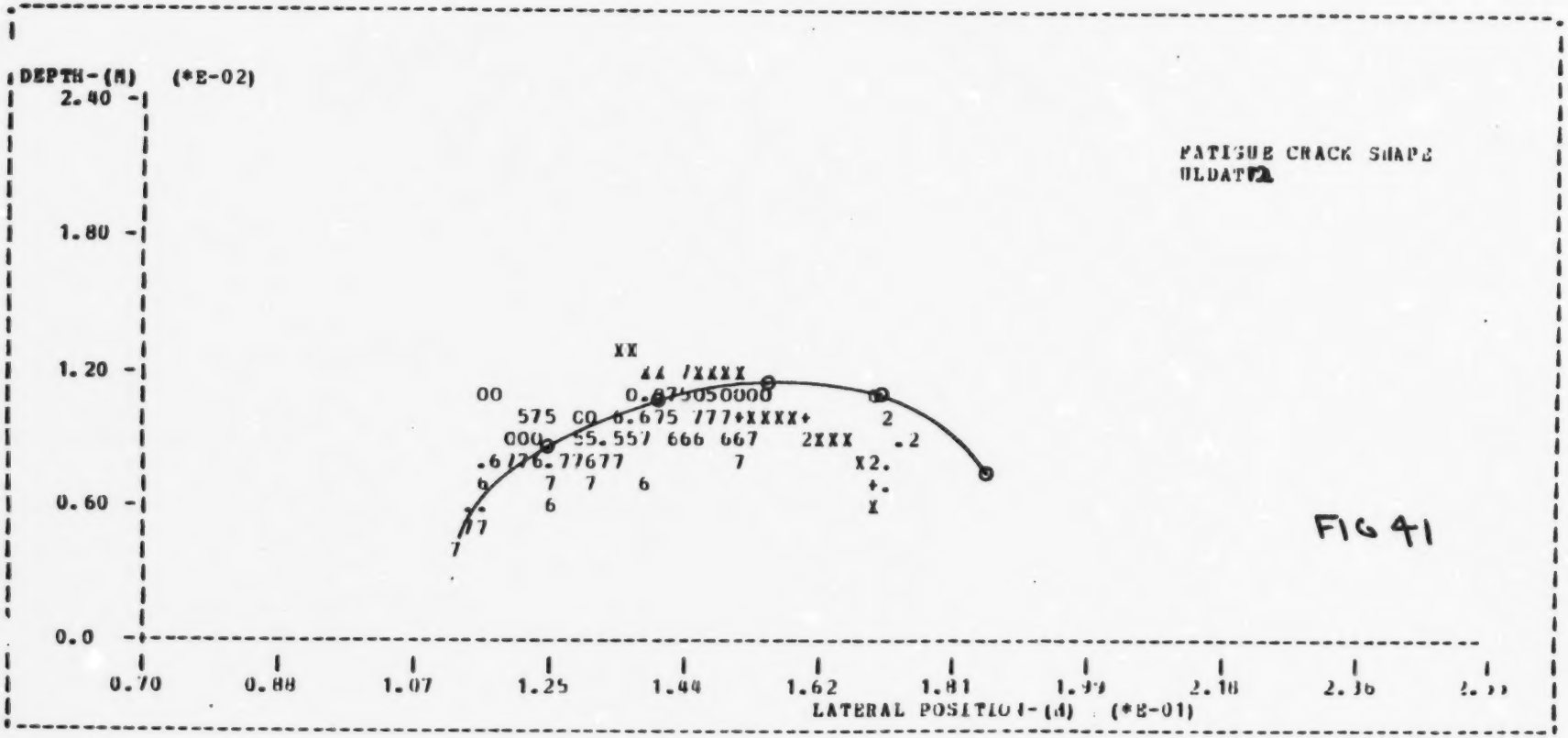
DEPTH-(M) (*E-02)
2.40
1.80
1.20
0.60
0.0
FATIGUE CRACK SHAPE
OLDAT2
0.70
0.88
1.07
1.25
1.44
1.62
1.81
1.99
2.18
2.36
LATERAL POSITION-(M) (*E-01)

FIG 41

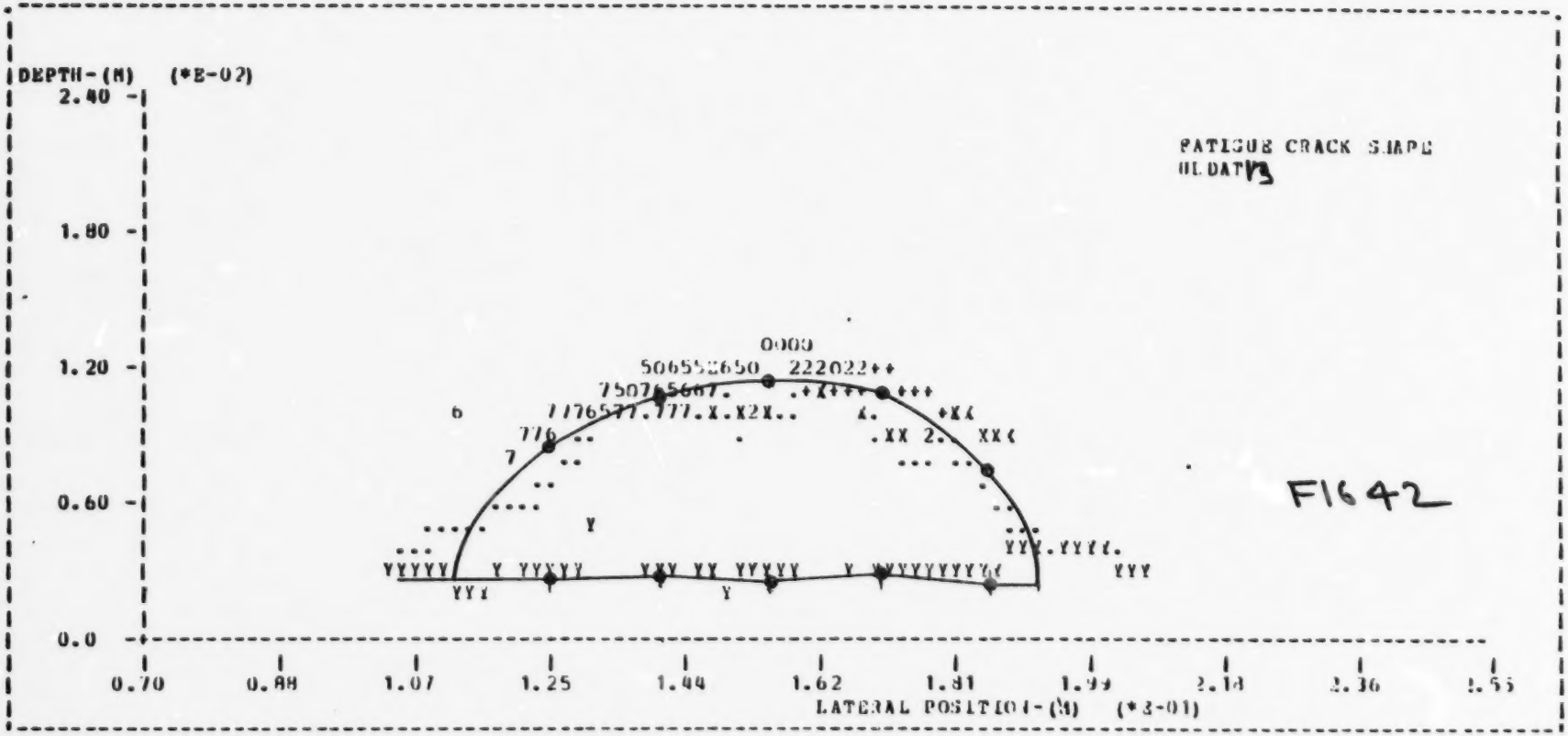
DEPTH-(M) (*E-02)
2.40
1.80
1.20
0.60
0.0
FATIGUE CRACK SHAPE
0.70
0.88
1.07
1.25
1.44
1.62
1.81
1.99
2.18
2.36
2.55
LATERAL POSITION-(M) (*E-01)
F1642

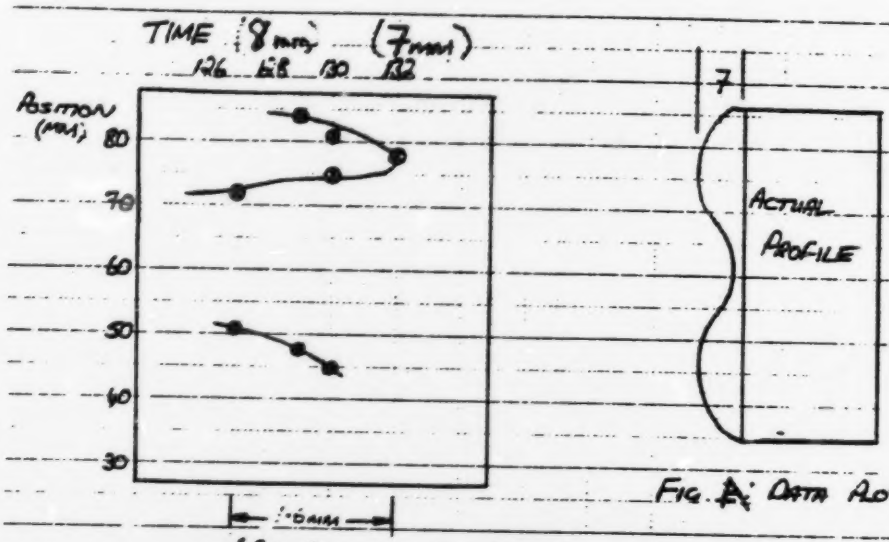

FIG. A: DATA PLOT FOR PART (A).

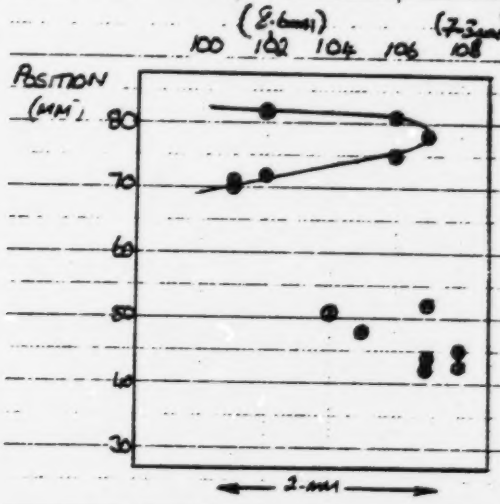

FIG. B: DATA PLOT FOR PART (B).

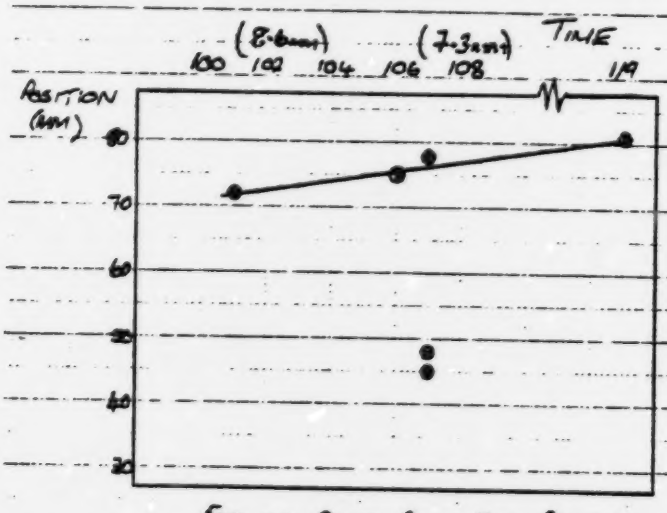

FIG. C: DATA PLOT FOR PART (C)

FIG 43

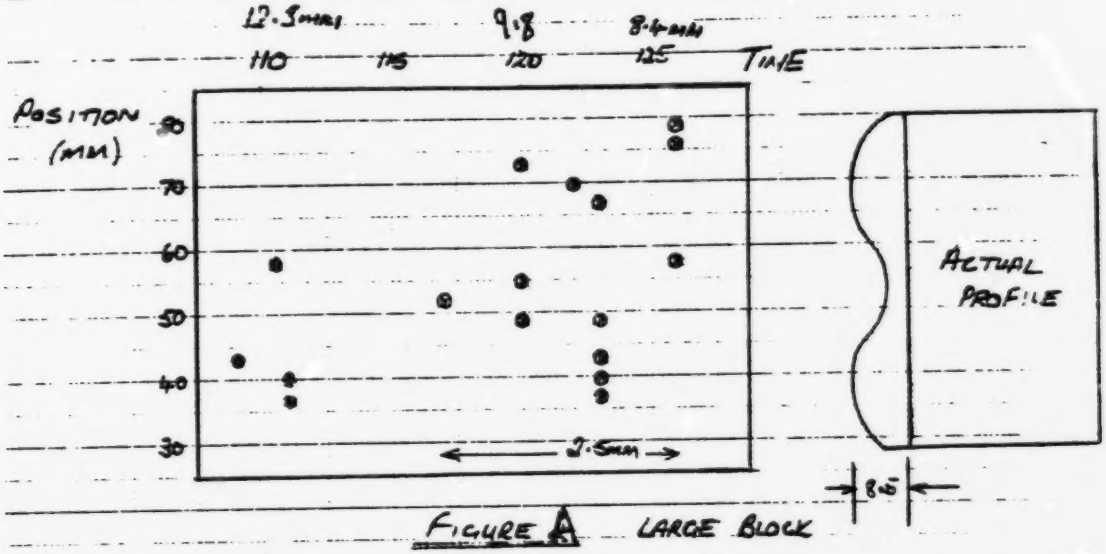

FIGURE A LARGE BLOCK

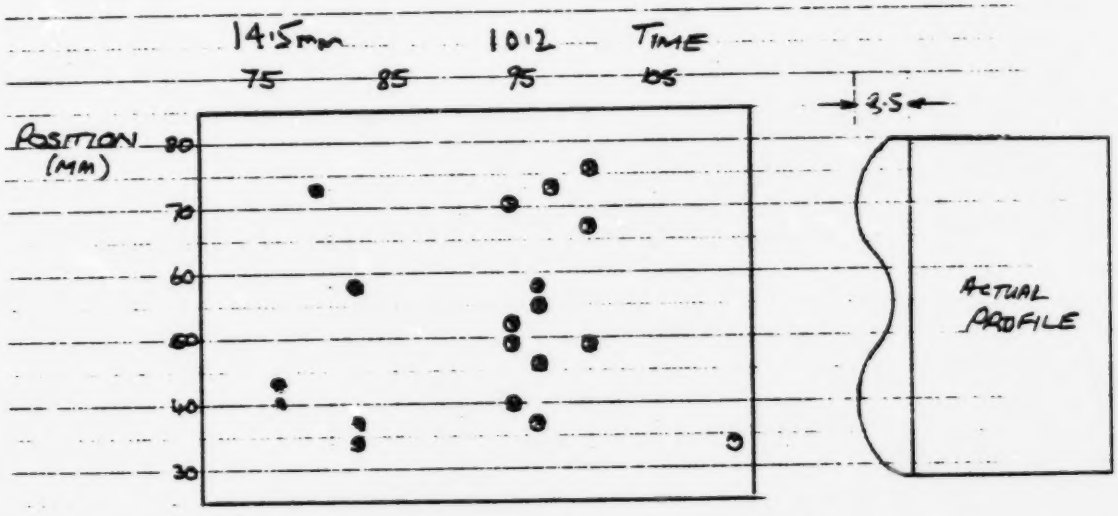

FIGURE B SMALL BLOCK

FIG 44

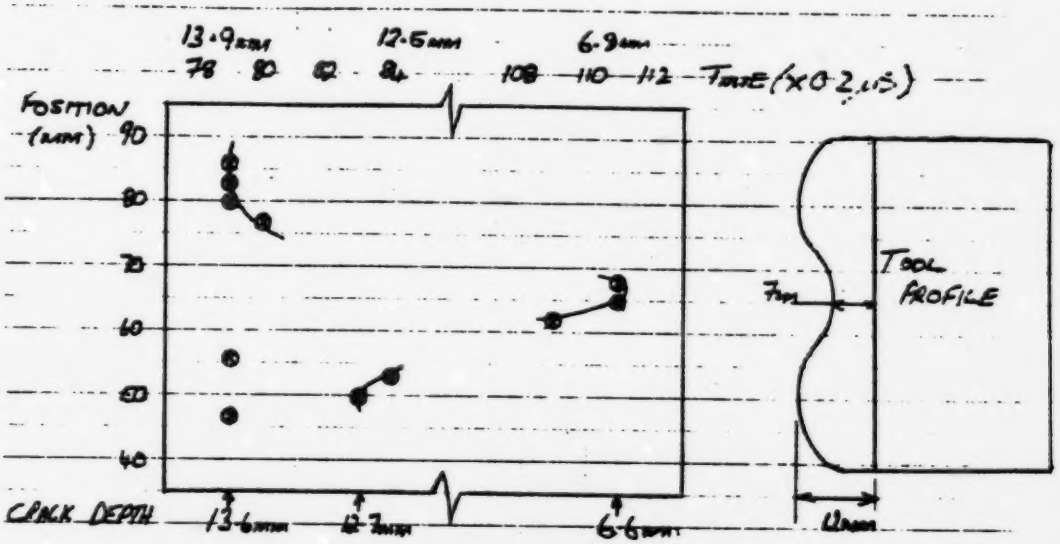

FIGURE 4: SMALL BLOCK SIDE (A)

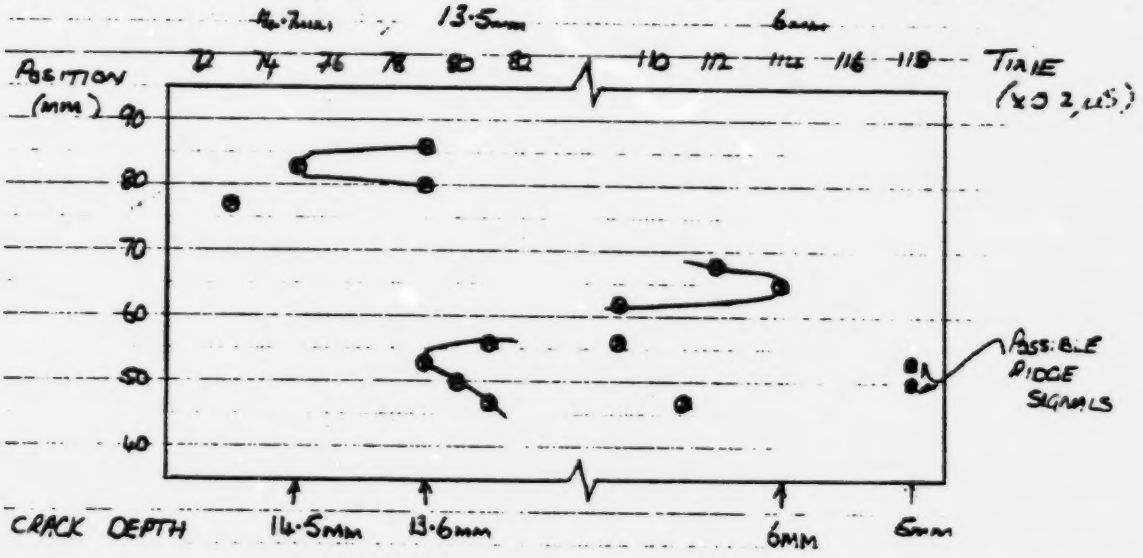
13·5mm
6mm
72 74 76 78 80 82 110 112 114 116 118 TIME (x0·2 μS)
POSITION (mm) 90 80 70 60 50 40
POSS. EDGE SIGNALS
CRACK DEPTH 14·5mm 13·6mm 6mm 5mm

FIGURE 5: SMALL BLOCK SIDE (B)

FIG 45

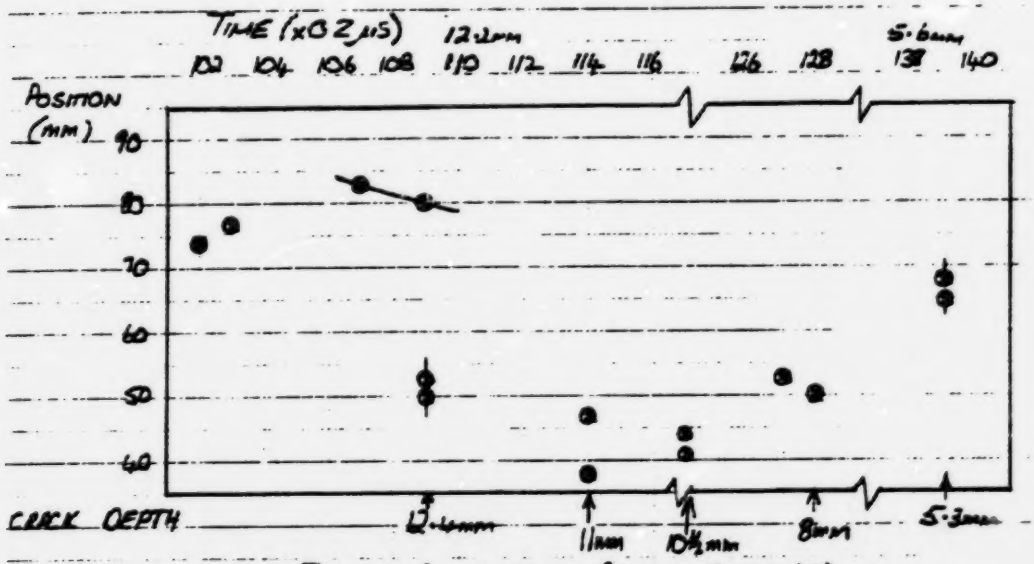

FIGURE C; LARGE BLOCK SIDE (A)

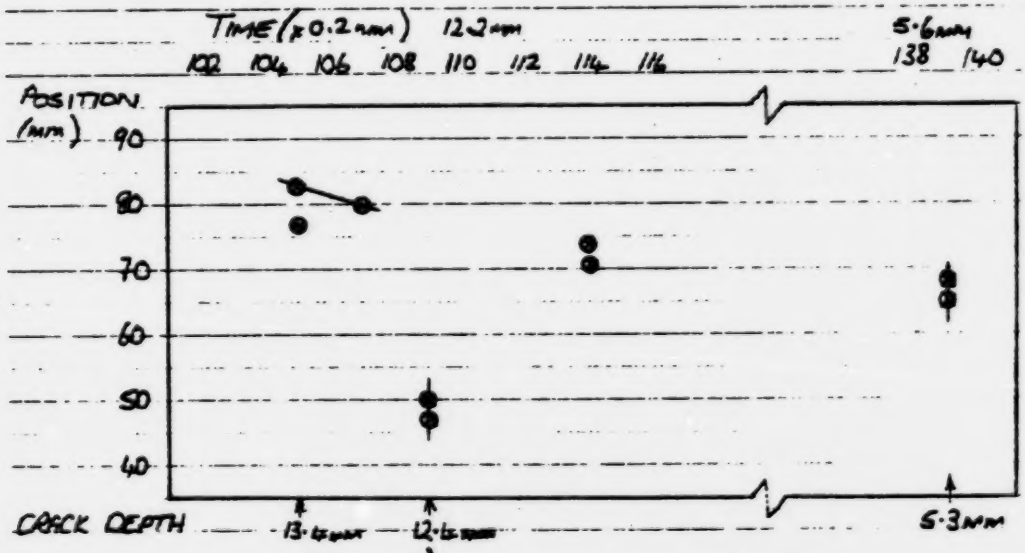

FIGURE D; LARGE BLOCK SIDE (B)

Fig 46

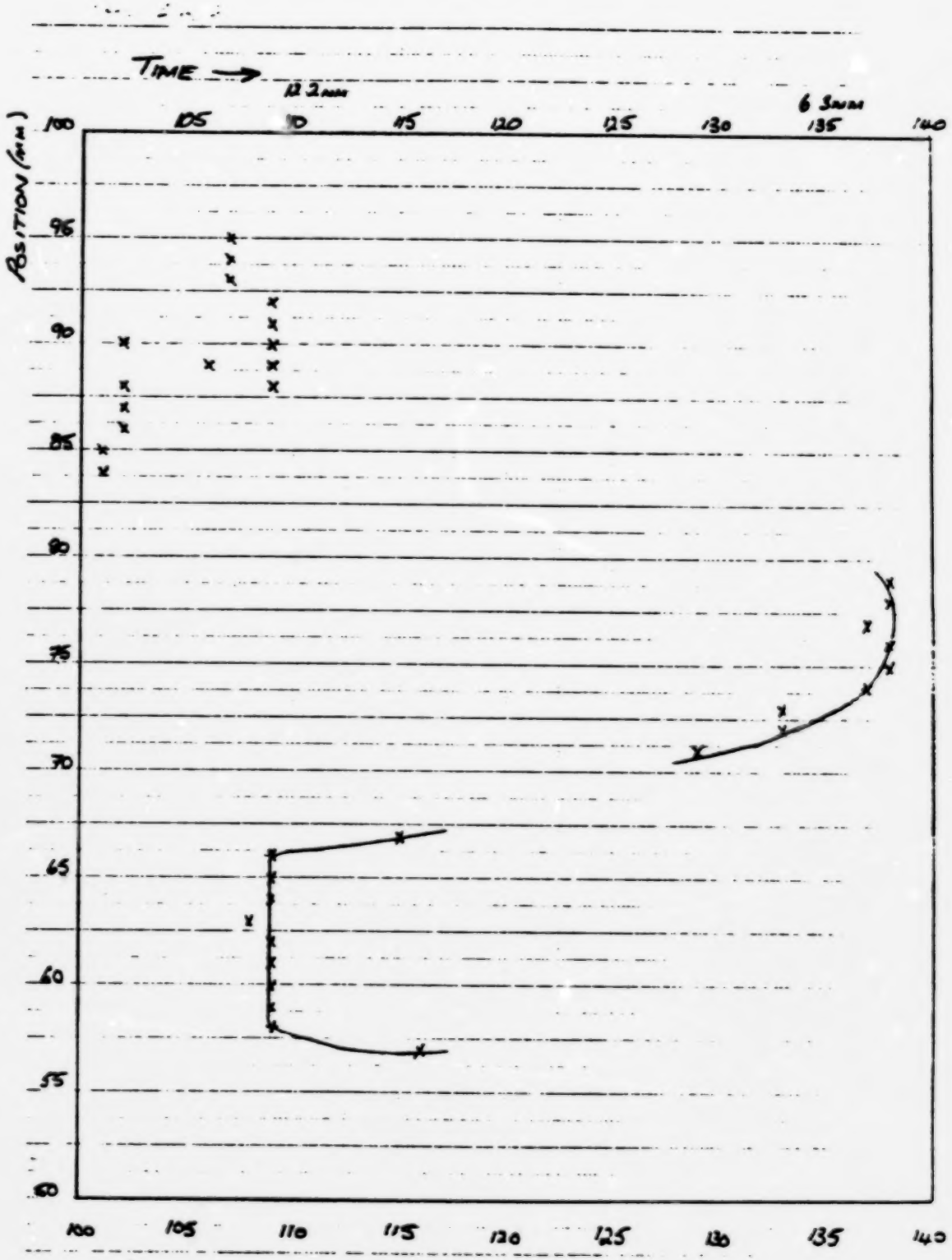

FIGURE 47: EDM CRACK No 3, LARGE BLOCK (45°)

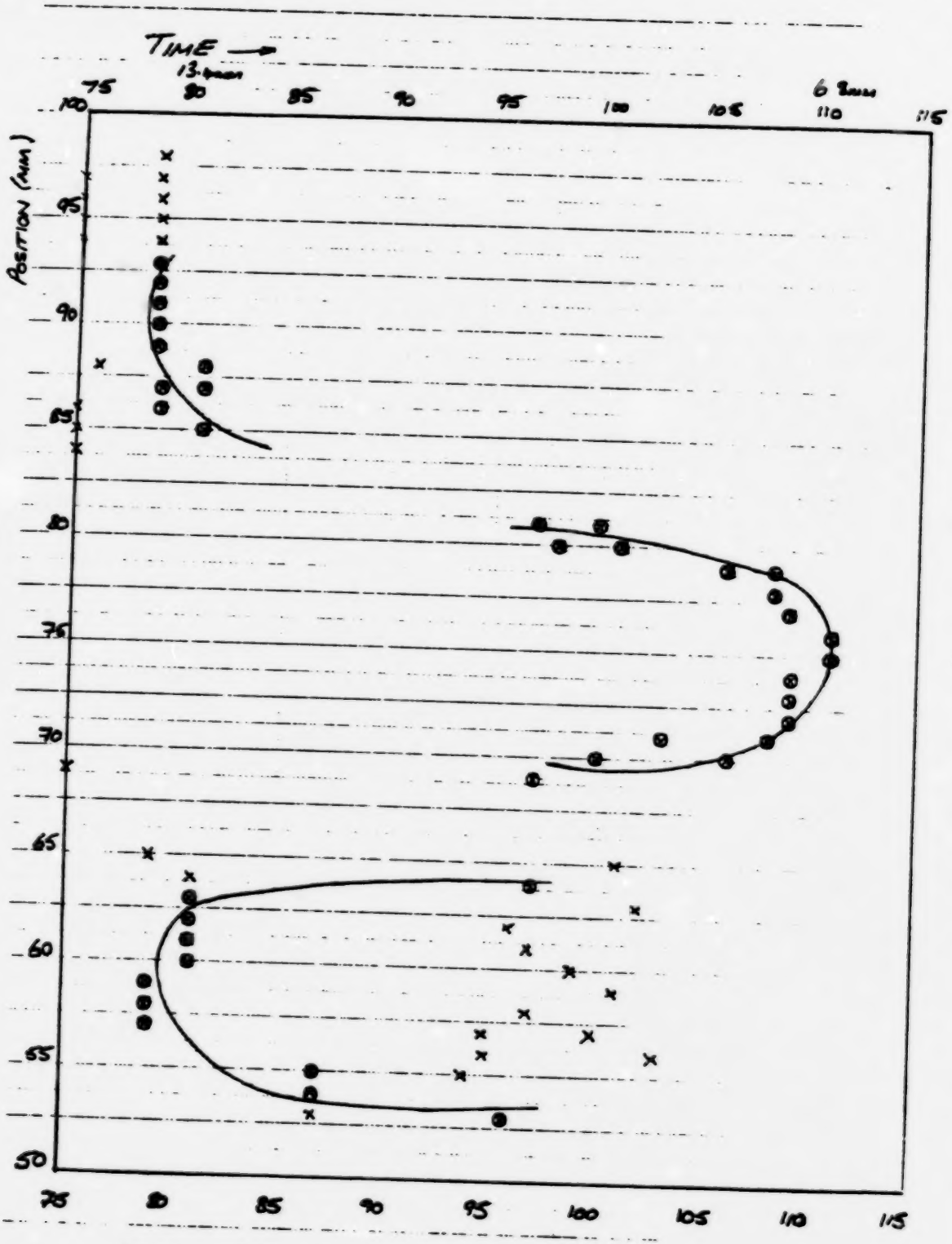

FIGURE 48 EDM CRACK No 3 SMALL BLOCK (45°)

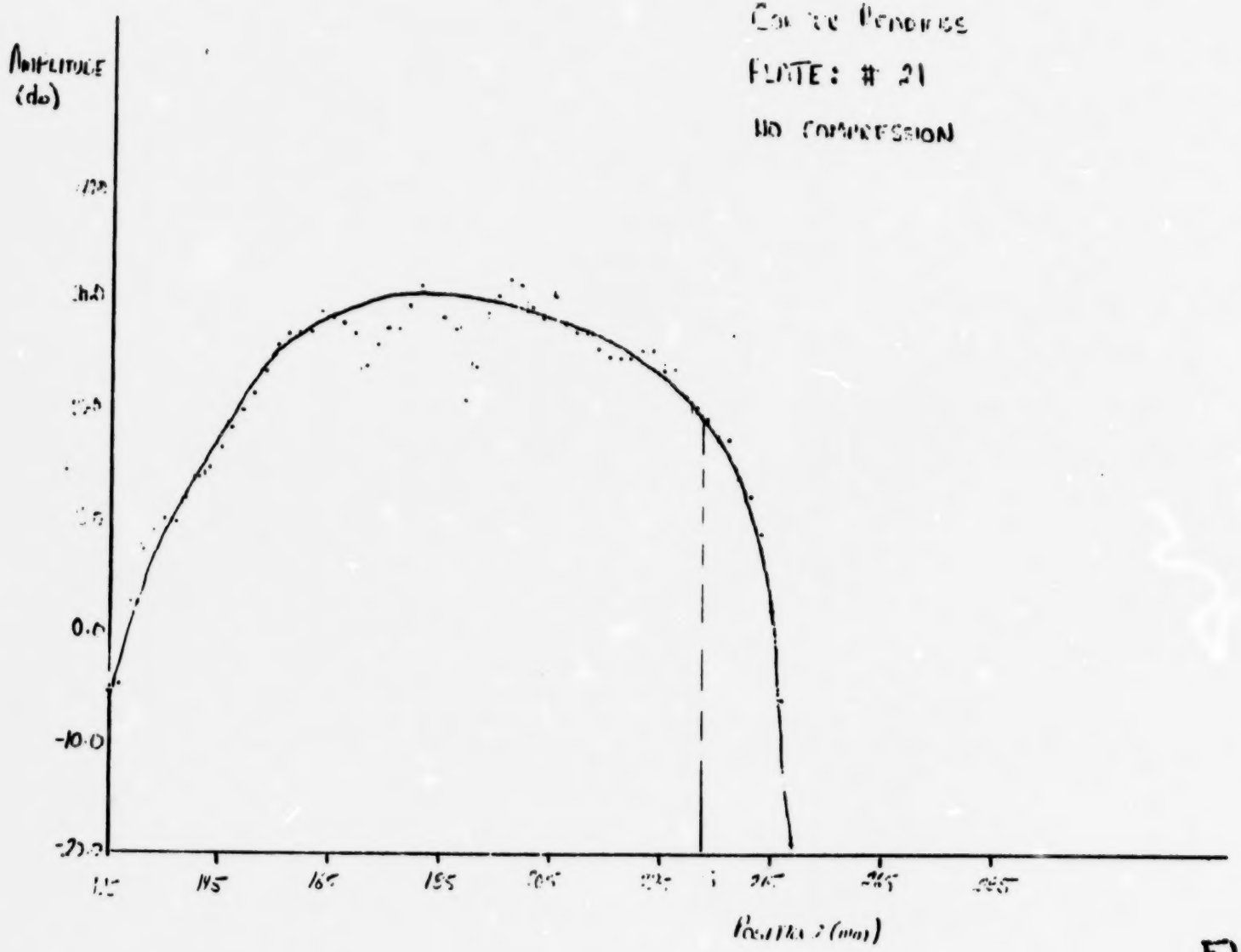

Cavity Pendulum

FLUTE: # 21

NO COMPRESSION

F1649

CORNER PROFILE
PLATE #21

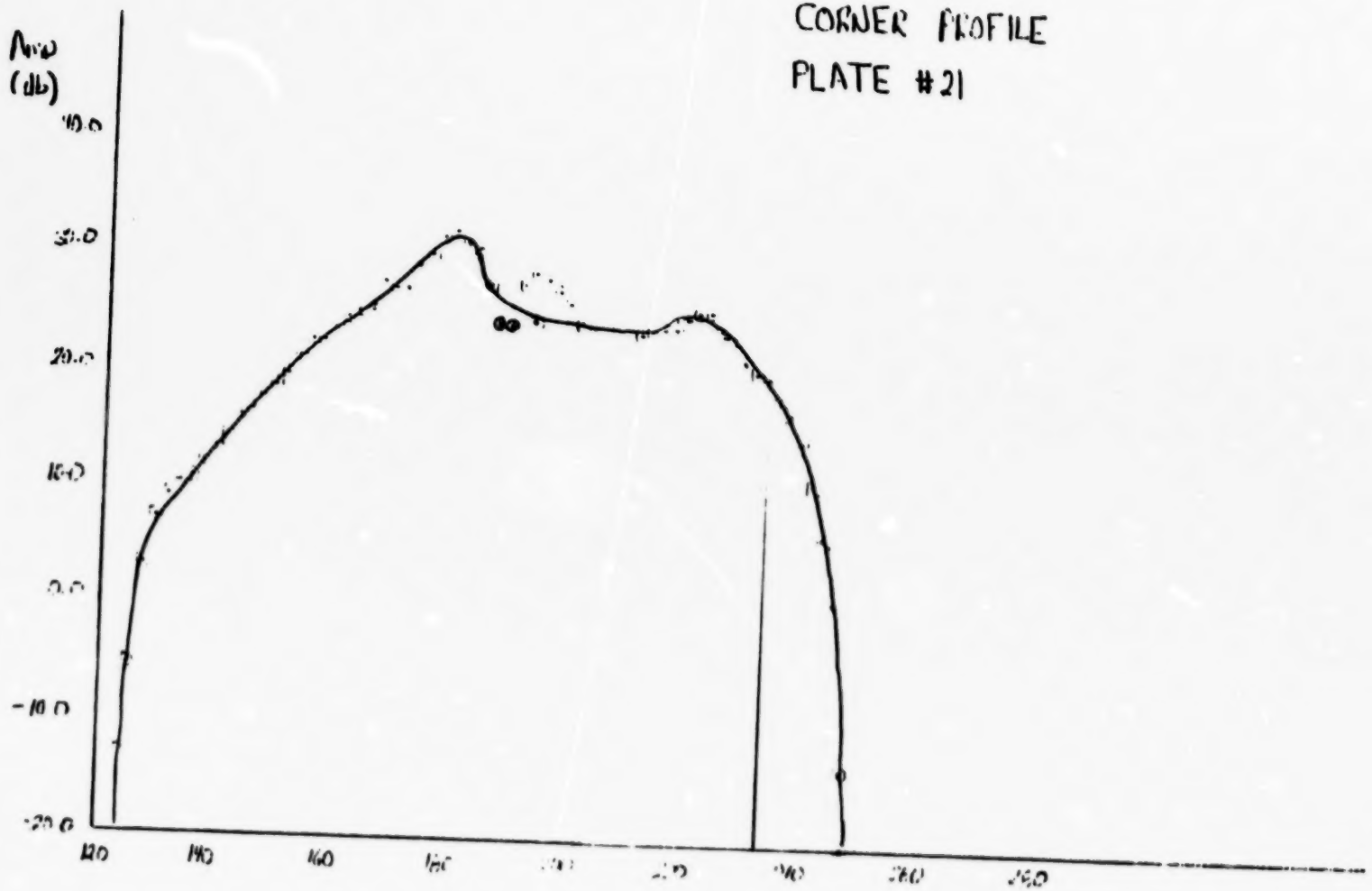

FIG 5

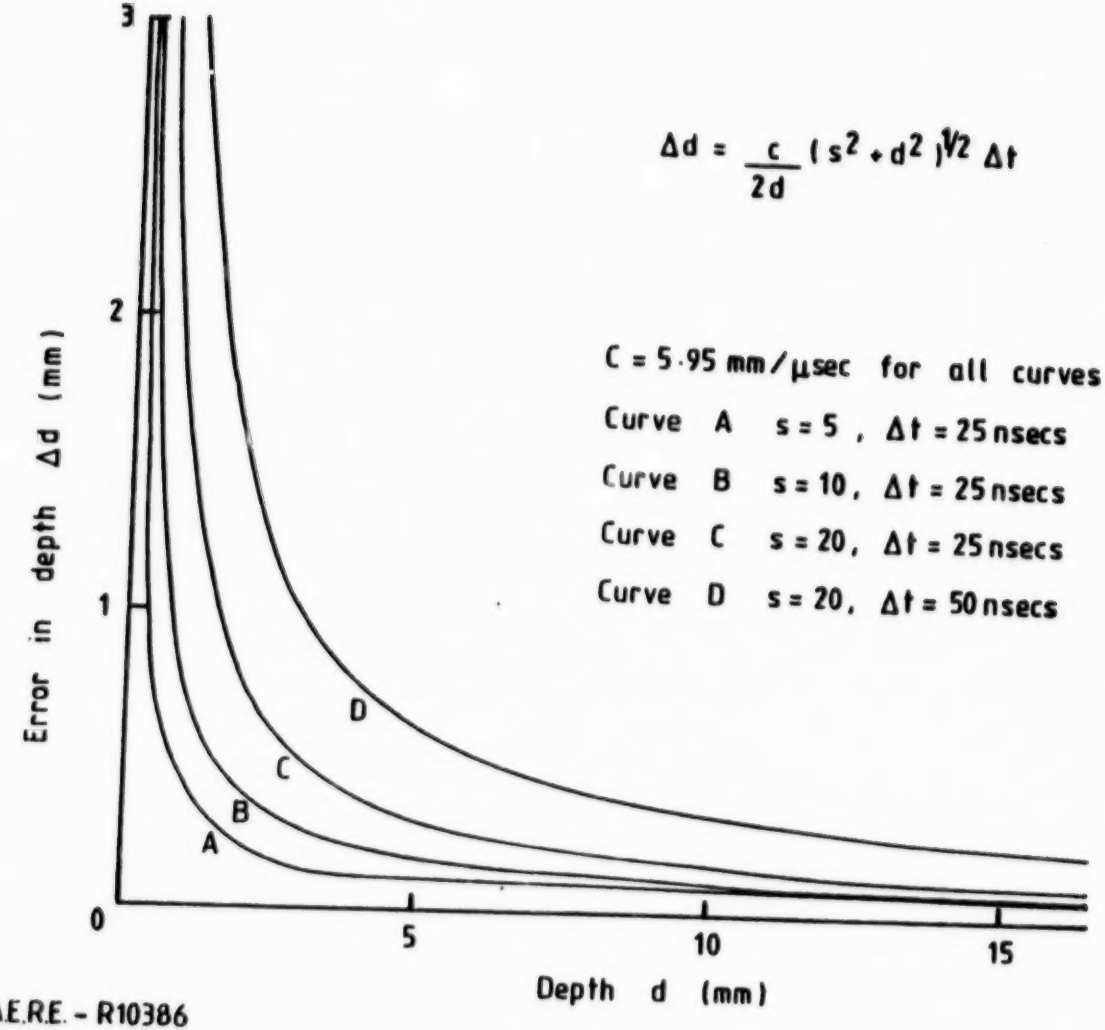

A.E.R.E. - R10386

FIG 51 ERROR IN DEPTH , Δd , AT DEPTH d FOR NEAR SURFACE CRACKS

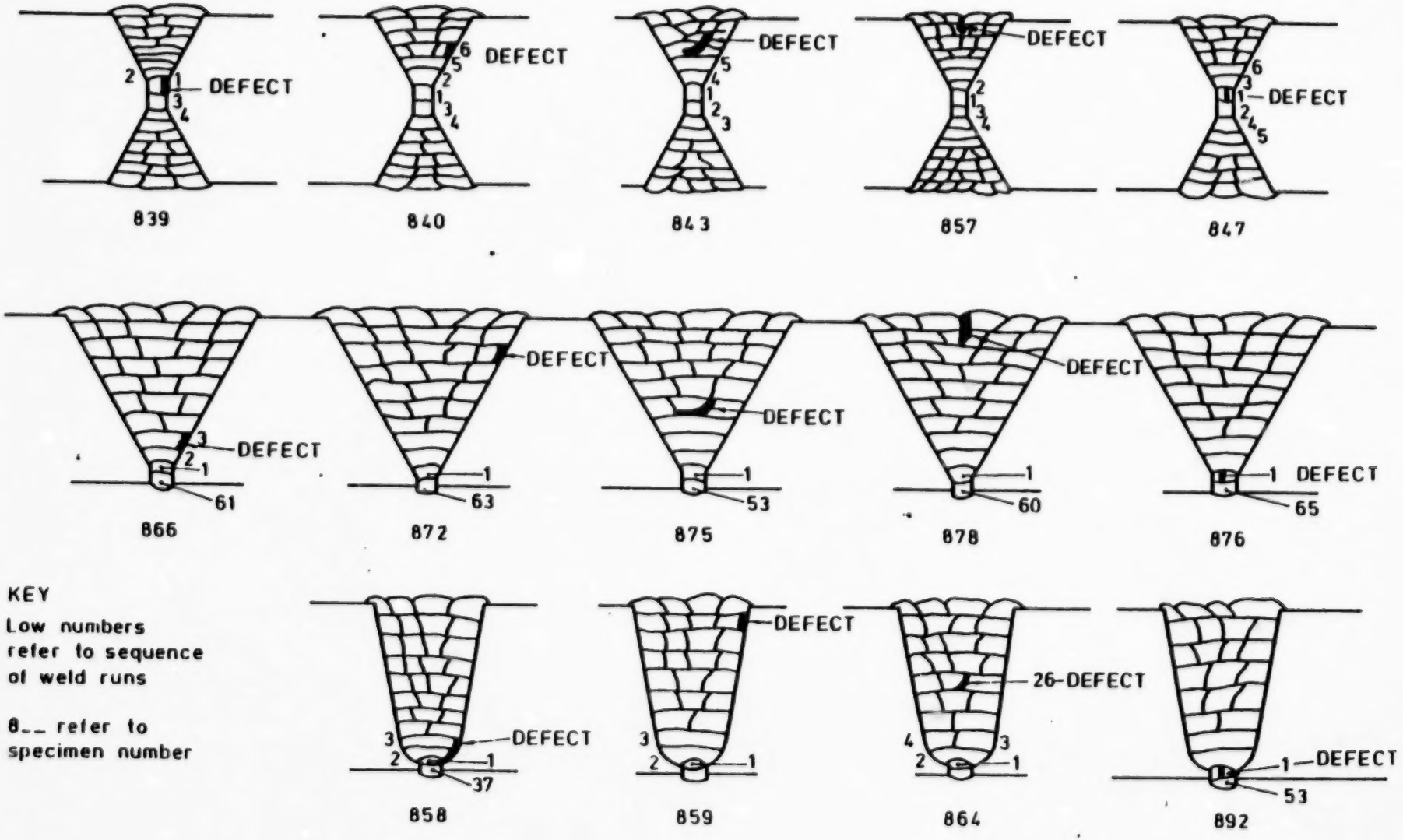

FIG.52 DIAGRAMMATIC REPRESENTATION OF SPECIMENS

POOR

QUALITY

ORIGINAL